Optimal Correction of The Slice Timing Problem and Subject Motion Artifacts in fMRI

David Parker

Submitted in partial fulfillment of the
requirements for the degree of
Doctor of Philosophy
in the Graduate School of Arts and Sciences

COLUMBIA UNIVERSITY

2019

ABSTRACT

Optimal Correction of The Slice Timing Problem and Subject Motion Artifacts in fMRI

David Parker

Functional magnetic resonance imaging (fMRI) is an extremely popular investigative and clinical imaging tool that allows safe and noninvasive study of the functional living brain. Fundamentally, fMRI measures a physiological signal as it changes over time. The manner in which this spatio-temporal signal is acquired can create technical challenges during image reconstruction that must be corrected for if any meaningful information is to be extracted from the data. Two particular challenges that are fundamentally intertwined with each other are temporal misalignment and spatial misalignment. Temporal misalignment is due to the nature of fMRI acquisition protocols themselves: a 3D volume is created by sampling and stacking multiple 2D slices. However, these slices are not acquired simultaneously or sequentially, and therefore will always be temporally misaligned with each other. Spatial misalignment arises when subject motion is present during the scan, resulting in individual volumes being spatially misaligned with each other. Spatial and temporal misalignment are not independent from each other, and their interaction can cause additional artifacts and reconstruction challenges if not addressed properly.

The purpose of this thesis is to critically examine the problem of both spatial and temporal misalignment from a signal processing perspective, while considering the physical nature and origin of the signal itself, and develop optimal correction routines for spatial and temporal misalignment and their associated artifacts.

One of the most immediate problems associated with temporal misalignment is that the order in which the slices are acquired must be known in order for correction to be possible. Surprisingly, this information is rarely provided with old or shared data, meaning that this critical preprocessing step must be skipped, significantly lowering the value of the data. We use the spatio-temporal properties of the fMRI signal to develop a robust and accurate algorithm to infer the slice acquisition order retrospectively from any fMRI scan. The ability to extract the interleave parameter from any data set allows us to perform slice timing correction even if this information had been lost, or was not provided with the scan.

In the next section of this work, we develop a new optimal method of slice timing correction (Filter-Shift) based on the fundamental properties of sampling theory in digital signal processing. By examining the properties of the signal of interest (The blood oxygen level depended signal: BOLD signal), we are able to design and implement an effective FIR filter to simultaneously remove noise and reconstruct the signal of interest at any shifted offset, without the need for sub-optimal interpolation.

In the final section, we investigate the effects of different motion types on the MR signal based on the Bloch equation, in order to develop a theoretical foundation from which we can create an optimal correction method. We devise a novel method to remove these artifacts: Discrete reconstruction of irregular fMRI trajectory (DRIFT). Our method calculates the exact displacement of the k-space samples due to motion at each dwell time and retrospectively corrects each slice of the fMRI volume using an inverse nonuniform Fourier transform. We conclude that a hybrid approach with both prospective and retrospective components are essentially required for optimal removal of motion artifacts from the fMRI data.

The combined work of this thesis provides two theoretically sound and extremely effective correction routines, that both remove artifacts and restore the underlying sampled signal. Motion correction and slice timing correction are typically the first two preprocessing steps to be applied to any fMRI data, and thus provide the foundation for any further analysis. While many other preprocessing steps can be omitted or included depending on the analysis, motion correction and slice timing correction are unequivocally beneficial and necessary for accurate and reliable results. This work provides a theoretical and quantitative framework that describes the optimal removal of artifacts associated with motion and slice timing.

Contents

List of Figures

List of Tables

Acknowledgments & Dedication

It's tempting to try to say something profound and dramatic about the journey I've been through for this thesis, but it's difficult to do so without being cliché. The truth is, *every* undertaking is a journey. You learn, you grow, you face the unexpected, you make mistakes, you keep going, and rarely do you end up where you thought you would be when the journey is over. At this point, all that's left to do is express my gratitude to those who have helped me along the way. I owe this entire thesis to my advisor Dr. Ray Razlighi, who gave me the opportunity to work with him in his lab, and mentored me in the ways of research, writing, and MRI. I'm grateful for the guidance Ray has given me, as well as the patience he's had with me over our years together. Ray has always held the lab to a high standard, and our work is better because of it. Ray has been both a friend and a teacher to me, and I'm only able to write this thesis today because of the opportunity he gave me. I also owe a great deal of gratitude to Dr. Yaakov Stern, who helped fund many years of my research. Without his generosity, I would not have been able to do this work. I also owe a great deal to Dr. Ray Lee who helped explain many technical workings of the Siemens scanners at MBBI, and who helped troubleshoot numerous challenges (often user-induced) that I encountered while collecting data.

For the final part of my thesis, I needed to navigate the maze that was raw fMRI data. Without the collaboration of Dr. Christoph Juchem and the help of his student Kelley Swanberg, I'm certain I would still be trying to decode that data to this day. They graciously provided me with their time, as well as documentation files that became my bible for a few months. Thanks to the scanning opportunities provided by MBBI at the Zuckerman Institute (particularly to Dr. J. Thomas Vaughan for implementing the seed grants, and Kathleen Durkin for answering what anyone else would consider an unreasonable amount of questions), I was able to quickly and easily acquire real fMRI data sets that serve as proof of concept for a large part of my work. I would also like to acknowledge Helen Cen, who also answered the many questions I asked, and helped me navigate the dissertation process. In general, the entire BME faculty and staff have been nothing but helpful and supportive, and they all genuinely want to see me succeed.

Aside from the academics, I of course have the usual cast of friends and family to thank. To all my friends who finished undergrad, got jobs, and made money, thank you for being patient with my student life.

I only hope that you were as jealous of how late I could sleep in as I was of your paychecks. Your friendship and visits helped make my time here special, and I loved hunting for all the coolest places in the city to take you to when you visited. And to the friends I made here, you've become an irreplaceable part of my life, and I wouldn't trade that for anything. Particularly Edgar, Mal, and Charishma, who helped me get out from under my grad student rock from time to time. Lastly but not leastly, I want to thank my parents, who were as patient and supportive as anyone could be. They offered me their help and support whenever and however they could. That may seem like a token symbolic thank you, but I wrote entire chapters of this thesis fueled by care packages sent from Mom. And of course, my Dad has always been interested, supportive, and eager to help if at all possible, and I've enjoyed working through an occasional problem with him.

In light of this, there's no single dedication to make for this thesis. To me it feels like it was written by a cast of thousands, as they say. However, there are four people who have had the largest impact on me and my work over the years, and so this thesis is dedicated to my advisor Ray, to my parents, Jean and Kevin, and to Katherine, who would be proud.

I should also note that earlier, when I said "At this point, all that's left to do is express my gratitude", that was a complete lie. There's so much to do. I should be proof reading. Oh no.

1 Introduction & Thesis Overview

1.1 Background

1.1.1 Nuclear Magnetic Resonance

Nuclear magnetic resonance (NMR) describes the phenomena that occurs when charged nuclei are placed in a strong magnetic field. The most common example of this, and indeed the principle behind medical MRI, is the hydrogen proton. When placed in a strong magnetic field, protons will 1) align themselves with the main magnetic field, and 2) undergo precession at a resonance frequency which is determined by physical factors such as the mass and electrical properties of the proton, as well as the strength of the magnetic field. This is illustrated in Figure 1.1, where the proton is represented as its magnetic moment vector **μ**.

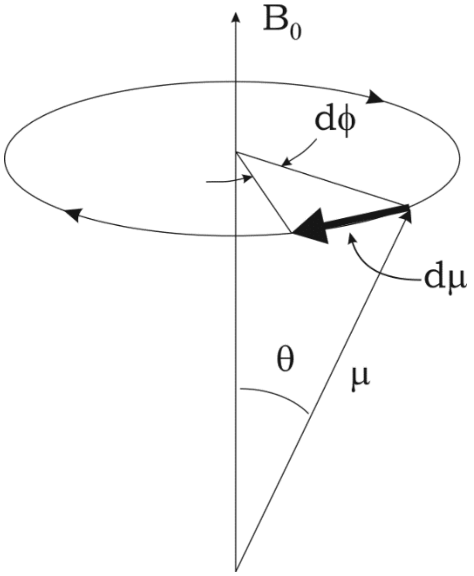

Figure 1.1 The fundamental behavior of a charged particle in an external magnetics field.
The charged nuclei (Most commonly a hydrogen proton) has a magnetic moment vector **μ**. When placed in a strong external magnetic field B_0, the proton begins to precess around the main magnetic field with differential motion d**μ** at an angle θ. The differential angle determines the precession frequency, defined as |dϕ/dt|. Reproduced from Magnetic Resonance Imaging.

The proton precesses around the main magnetic field **B** with angular velocity described by d**μ**. The angle covered by this precession over a period of time is given by dϕ. The exact frequency at which a given proton will precess is determined by:

$$\omega_0 = \frac{d\phi}{\mathrm{dt}} = \gamma B_0 \tag{1.1}$$

Where ω_0 is the angular frequency (known as the Larmor frequency), B_0 is the strength of the external magnetic field, and γ is the gyromagnetic ratio of the proton. Any volume of tissue will have an enormous amount of protons, all of which have their own magnetization vector precessing around the magnetic field. Despite the large number of protons, these spins are undetectable due to the unsynchronized phase of their precession. Using a radio frequency (RF) pulse tuned to the larmor frequency, these protons can be "excited", which synchronizes all the spins and generates a measureable signal. This is the basis of all MR imaging.

1.1.2 The fMRI Signal

fMRI uses a fast pulse sequence known as Echo planar imaging (EPI) to acquire the MR signal. EPI, and indeed all MRI modalities, acquire a signal created by the synchronization of protons spinning in a large magnetic field. The magnitude of this signal will fundamentally depend on the density of excitable protons in any given unit volume. The primary frequency of these spins, ω_0, can be demodulated, meaning we only detect any deviations from this frequency. These spins are picked up by receiver coils and digitally sampled. The detection and sampling of the signal all contribute to the resulting signal equation. This equation is usually simplified to include the effects from all these processes in an "effective spin density" term, $\rho(\boldsymbol{r})$, which describes the magnitude of a signal generated at spatial location ***r*** given the proton density of the tissue and detection properties of the MRI machine. With a few assumptions that neglect signal decay over time, a simplified signal equation can be expressed as:

$$s(t) = \iiint \rho(\boldsymbol{r})\, e^{i(\phi(r,t))} d\boldsymbol{r} \tag{1.2}$$

where $\phi(\boldsymbol{r}, t)$ is the phase offset accumulated at point ***r*** and time t. This represents any additional phase the spins gained (or lost), beyond what would be accumulated from spinning at its Larmor frequency ω_0 alone. Occurring naturally, these phase offsets are not useful. However they can be artificially manipulated by applying magnetic gradients to the volume. When a gradient is applied along an axis, the resonance frequency will deviate from the Larmor frequency. For example, a gradient along the z axis will result in the following deviation:

$$\omega_G(z,t) = \gamma z G_z(t) \tag{1.3}$$

where G is the gradient strength in Tesla/meter, and z is the position on the z axis. The amount of phase accumulated from this offset depends on the duration that the gradient was applied:

$$\phi_G(z,t) = -\int_0^t \omega_G(z,t')dt' = \gamma z \int_0^t G_z(t')dt' \tag{1.4}$$

It is convenient to move the integration of the gradient into a time dependent variable *k*:

$$k_z(t) = \frac{\gamma}{2\pi}\int_0^t G_z(t')dt' \tag{1.5}$$

This can be generalized to all axis as the dot product of the spatial location vector ***r*** with the 3D gradient vector ***G*****,** which results in a 3D k-space vector, $\boldsymbol{k}$**.** Putting the signal equation in terms of $\boldsymbol{k}$ reveals that the signal equation s($\boldsymbol{k}$) is the Fourier transform of the object's proton density:

$$s(\boldsymbol{k}) = \iiint \rho(r)\, e^{-i2\pi \boldsymbol{kr}} d\boldsymbol{r} \tag{1.6}$$

By manipulating the gradients in a precise manner, a 1, 2, or even 3 dimensional k-space can be sampled, and the image can be reconstructed with a simple inverse Fourier transform (IFT).

1.1.3 Origins of The BOLD Signal

fMRI is a fast imaging technique sensitive to changes in blood oxygenation levels. Changes in signal intensity due to blood oxygenation is called the blood oxygenation level dependent signal (BOLD signal). The discovery of the phenomena on which the BOLD signal is based was first noticed as a curiosity

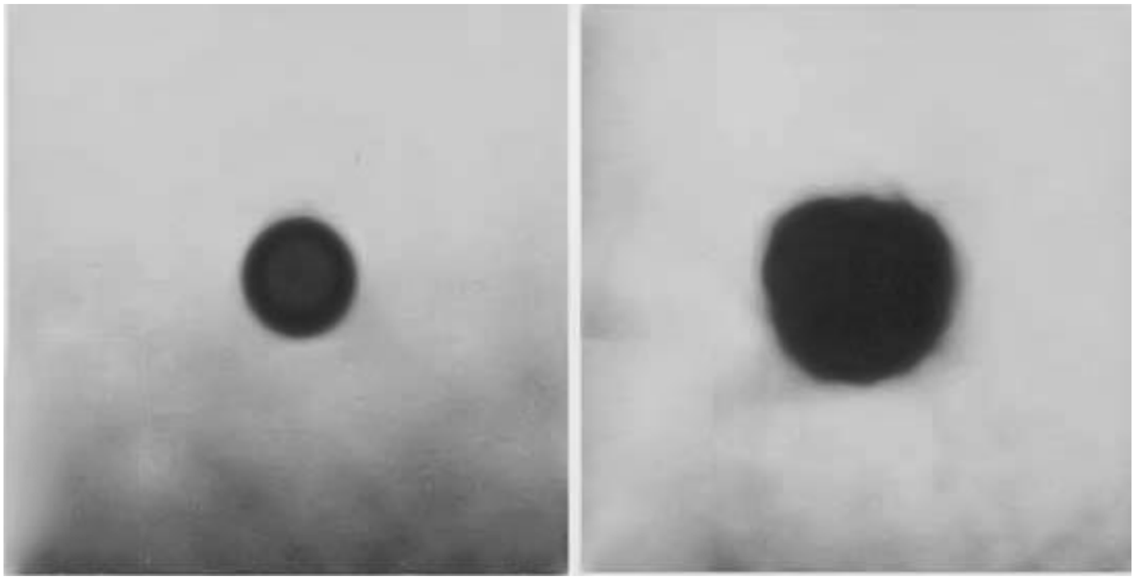

Figure 1.2 The effect of deoxygenated hemoglobin on a T2* image.

In this figure, two identical tubes are imaged, one filled with oxygenated hemoglobin (left), and the other with deoxygenated hemoglobin (Right). The deoxygenated hemoglobin causes small distortions in the surrounding magnetic field, causing the spins in these regions to dephase and cancel each other out, resulting in the larger dark shape. [2]

by Linus Pauling when he found that deoxygenated hemoglobin (dHb) has different magnetic properties than oxygenated hemoglobin [1]. Oxygenated hemoglobin is diamagnetic, and largely unaffected by the magnetic fields of an MRI scanner. dHb, on the other hand, is paramagnetic. Because of this, it distorts the surrounding magnetic field. It was first shown definitively that oxygenated vs dHb gave different MRI signals by Ogowa et. al. [2] by imaging two identical tubes; one filled with oxygenated blood, and the other deoxygenated blood. This demonstration is shown in Figure 1.2. The distortions in the magnetic field caused by the dHb cause protons in the tissue to precess at slightly different frequencies. After excitation, this will result in the protons de-phasing faster, making the tissue appear darker. However, when a brain region becomes active, the signal recorded by fMRI shows a measureable *increase* in signal intensity when there is activation. This is due to a phenomenon known as neurovascular coupling.

When a network or region is actively working, it sees a substantial increase in activity in the form of action potentials. Neurons have no way of storing metabolites for consumption, and so they rely on arterial blood to provide a continuous supply of metabolic materials [3], implying that the consumption of metabolites from the blood is directly proportional to the demand [4]. In order to meet these demands, the brain has an intricate and sensitive blood-delivery compensation mechanism called neurovascular coupling [5]. Neurovascular coupling works by increasing the amount of blood flowing through an activated region. An example of this process is illustrated in Figure 1.3. At rest, a steady amount of oxygen is extracted from oxygenated hemoglobin in the blood. Neuronal firing increases the demand for oxygen, causing more to be extracted. The mechanisms of neurovascular coupling detects this activity, and respond with a large increase in blood flow and blood volume to the area, providing more metabolites to the region. The amount of blood sent to the region vastly overcompensates for the increase in activity [6]–[10],[3]. This essentially "washes out" the deoxygenated hemoglobin in the area, leading to smaller magnetic field distortions. In BOLD fMRI this will result in higher signal intensity in that region. This principle is the foundation of the BOLD signal in fMRI. Although blood flow is an indirect, and therefor imperfect measure of neural activity, studies have shown good correspondence between the BOLD signal, multi-unit activity, and local field

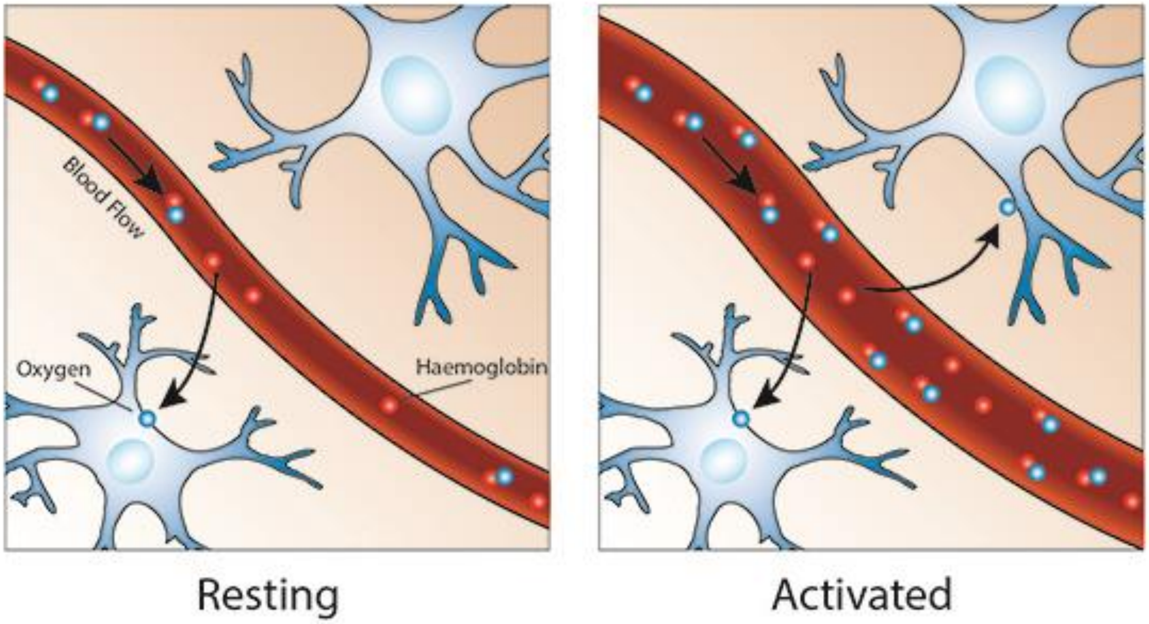

Figure 1.3: Changes in blood volume and flow due to neurovascular coupling.

At rest, neurons consume a "baseline" level of oxygen (Left). When neurons are activated, their oxygen consumption increases (Right). The body compensates for this by greatly increasing the flow and volume of blood present, increasing the number of available oxygenated hemoglobin. This is done through the mechanism of neurovascular coupling. Reproduced from Clare, 1997 [93].

potential recordings [11]–[13]. In fMRI , the BOLD signal is realtively small compared to the average voxel intensity in the brain, about 2% of the mean.

1.1.4 fMRI Image Acquisition

Because changes in blood oxygenation happen relatively quickly, there is a need to acquire multiple images in a short period of time in order to track the temporal transients in the brain. In order to achieve this, fMRI does not image at the high-resolution capabilities of a structural MRI scan. Further, it employs EPI to rapidly sample 2D slices with a single RF pulse. Each 2D slice is made up of a grid of "Voxels". A voxel is a sample of the average fMRI signal in a given volume of tissue (usually on the order of 2x2x2mm). The physical size and location of these voxels is determined by the scan parameters. Once these parameters are set, each voxel is spatially fixed for the duration of the scan. To form a full brain image, multiple 2D slices are acquired and stacked to form a single volume, which can typically be acquired between 1-3s, depending on the resolution and the number of slices being acquired. The time it takes to acquire one volume is known as the repetition time (or TR). In a typical fMRI scan, multiple volumes are acquired during a task or at rest to investigate activation. Changes in blood flow (and therefor neural activity) are tracked over time as a brightening or darkening of the voxel intensity. Visually, it is not possible to see which areas are being activated without the aid of a statistical analysis. Typically the general linear model (GLM) is used to match voxel time-series with an expected activation time-series. Another common analysis in the field is functional connectivity, which essentially compares the time-series' of all voxels in the brain to each other, and identifies which voxels temporally fluctuate in a similar fashion. These statistical analysis are very sensitive to anything that may corrupt the bold signal, such as temporal offsets between voxels, or any number of possible acquisition artifacts, such as motion, physiological noise, or magnetic field inhomogeneities.

1.1.5 K-space in fMRI

As explained in section 1.1.2, fMRI images are acquired in the frequency domain, referred to as k-space. The k-space of an image describes the image in terms of a set of planar waves oscillating at different frequencies. When these planar waves are summed together using an inverse Fast Fourier Transform

(IFFT) (which is a fast and computationally efficient algorithm to perform the otherwise slow inverse Fourier transform), they form an exact replication of the image. A single point in k-space describes the magnitude of a plane wave at a specific frequency and phase, encoded by the location of that point. Therefore, altering a single point in k-space will have an effect that is broadcast to the entire image.

The pattern in which consecutive points of k-space are sampled during fMRI is called the k-space "trajectory". The k-space trajectory traces a path along k-space by applying specific gradients in a specific order, and sampling the fMRI signal at designated points until a complete image can be reconstructed. This happens over a very short period of time, typically 60ms, which is twice the TE of the pulse sequence (The TE is half the time it takes to acquire a full slice of k-space). As the trajectory is traced, the signal from the receiver coils is sampled at a uniform rate, which collects evenly distributed k-space values. The time between two consecutive sampled k-space points is called the dwell time, typically around $5\mu s$. Some typical MRI trajectories are shown in Figure 1.4.

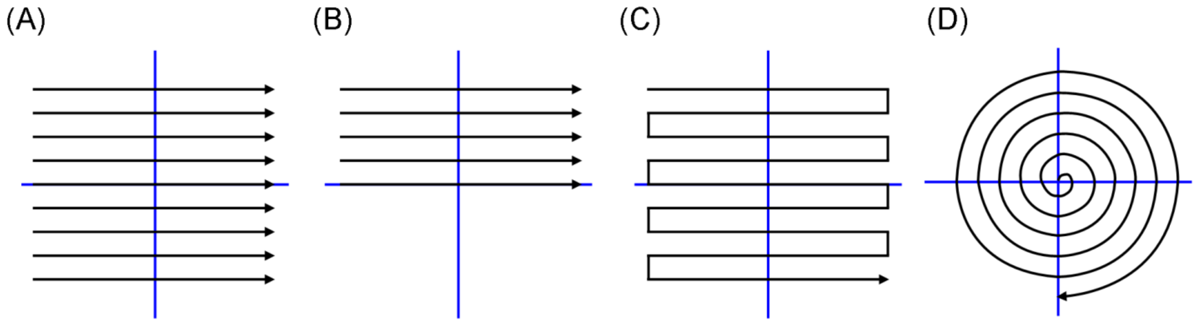

Figure 1.4: Common K-space sampling trajectories.

Four examples of k-space sampling trajectories. A) Line-By-Line, where each line is acquired in the same direction, one at a time. B) Partial acquisition. By taking advantage of symmetry properties in fMRI, partial acquisitions can be used to minimize acquisition time. C) The most common fMRI trajectory, in which the entire k-space is sampled by rapidly tracing a single zig-zag path. D) Spiral imaging, which can also be used for fMRI, where a spiral trajectory is traced out from the center of k-space in a single acquisition. Reproduced from Chase, 2019. [94]

The most common way to sample k-space in fMRI is by tracing a Cartesian grid as in Figure 1.4(C). This grid has uniformly spaced samples, which is a necessary condition in order to perform an IFFT. However, other non-Cartesian sampling strategies do exist, such as radial EPI, shown in Figure 1.4(D) [14].

These other methods require some form of regridding to perform image reconstruction using an IFFT. Regridding is the process of using the sampled points of k-space to estimate the values at gridded Cartesian coordinates using interpolation or some similar method. This is a fairly well understood problem in the field, and there are many available regridding algorithms [15], [16].

An illustration of a full EPI pulse sequence is shown in Figure 1.5. The RF pulse is applied at the beginning of the sequence. The G_{slice} gradient is applied at the same time as the RF pulse to determine which slice will be excited. In a typical EPI pulse sequence, slice selection is done along the z axis. G_{phase} and G_{read} are used to "trace" the k-space trajectory. This particular pulse sequence would trace a zig-zag trajectory as shown in Figure 1.4(C). The TE and TR are illustrated in this figure, however the dwell time cannot be shown on this scale in any meaningful way, as there are typically around 100 samples taken along each positive and negative segment of the G_{read} gradient.

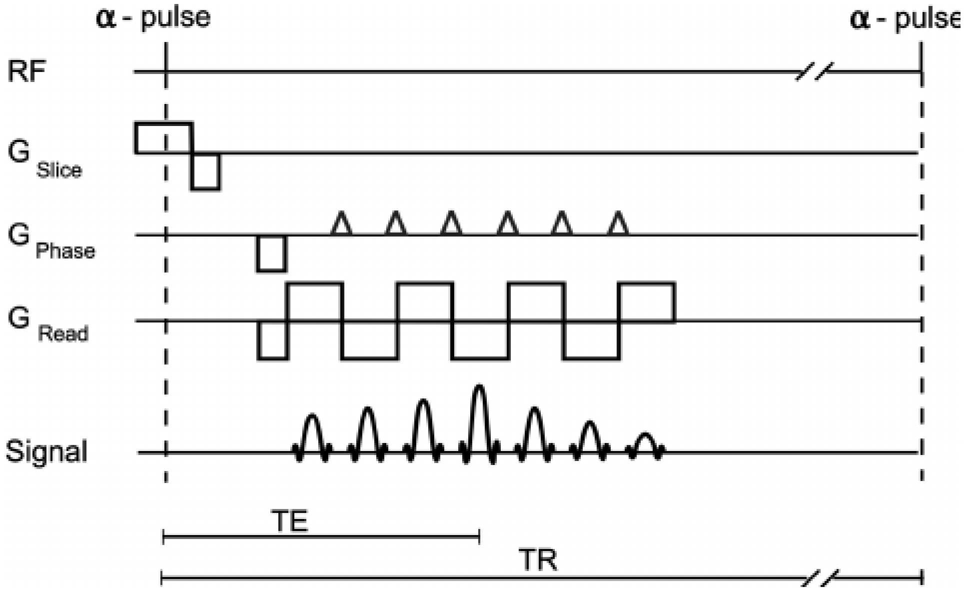

Figure 1.5: A typical EPI pulse sequence.

A typical EPI pulse sequence tracing a zig-zag k-space trajectory. Slice selection is done by applying a G_{slice} gradient at the time of RF excitation. K-space readout is achieved by applying precise G_{phase} and G_{read} gradients. This pulse sequence creates a k-space trajectory similar to the one shown in Figure 1.4 C. Reproduced from Gebker, 2007 [95].

1.1.6 fMRI Preprocessing

Because of the small size of the BOLD signal, the sensitivity of the statistical analysis, and the presence of artifacts and noise, fMRI data must undergo extensive preprocessing to remove noise and prepare the data for any meaningful analysis. Typical preprocessing steps can include slice timing correction, motion correction, spatial smoothing, prewhitening, spatial normalization, confound regression, and physiological noise correction. The order in which these steps are applied, and whether a step is even applied at all, varies from study to study with little investigation into their interaction with each other. Two specific processes that are inexorably intertwined with each other are slice timing correction and motion correction. The focus of this thesis is on these two preprocessing methods, both on how they interact, as well as how to correct for them in the optimal manner.

1.2 Slice Timing, Motion, and their interaction

1.2.1 The Slice Timing Problem

Because an fMRI volume is made of multiple 2D slices, such sequential acquisition results in an accumulating offset delay between the first slice and all following slices. Furthermore, to eliminate or attenuate leakages of a RF pulse excitation to adjacent slices, interleaved slice acquisition techniques are performed regularly in fMRI scanners. In interleaved slice acquisition, slices are not acquired sequentially, which imposes non-monotonic acquisition delay to the adjacent slices. Even-odd interleave is the most common interleaved slice acquisition in fMRI scanning although other kinds of interleaved sequences are also used, with different numbers of slices being skipped between two consecutive slice acquisitions [17]. No matter what kind of interleave is being used, they all give rise to the same issue, which is the non-monotonic offset delay in their acquisition timing. This processes can be described by a sampling function with a temporal offset that is dependent on the slice (or, spatial location z). If $f(\boldsymbol{r}, t)$ is the underlying true fMRI signal at location $\boldsymbol{r}$ ($\boldsymbol{r}= (x, y, z)$ in Cartesian coordinate system) and time instant t, then the sampled version of the true signal will be

$$F[\boldsymbol{r}, n] = f(\boldsymbol{r}, nTR + \varphi(z)) \tag{1.7}$$

where z is the slice number, and $\varphi(z)$ is the offset delay imposed for each slice by interleaved acquisition. The effect of this is illustrated in Figure 1.6. The same underlying signal is sampled at 4 different offsets (Figure 1.6 (A)). If these sampled values are plotted atop each other, they create 4 signals that appear completely different (Figure 1.6 (B)). The preprocessing step that corrects for these temporal offsets is referred to as Slice Timing Correction (STC).

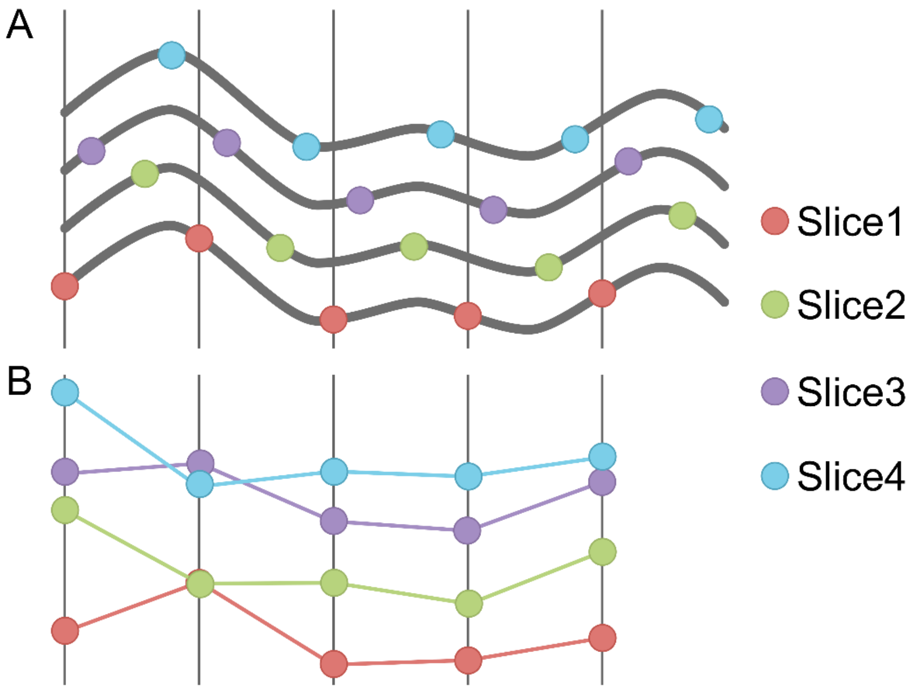

Figure 1.6: The slice-timing problem.

the same signal sampled at different offsets yields signals that do not look the same (A) four adjacent slices acquired with interleaved acquisition all sample the same underlying bold signal. (B) Without correction, reconstruction yields four different signals despite having the same underlying shape.

1.2.2 Interleave Parameters

While almost all studies use interleaved slice acquisition, the order in which interleaved slices are acquired might be different across manufacturers and pulse sequences. In other words, the interleave parameter may vary from image to image even when acquired with the same scanner. To correct for interleaved slice acquisition, It's necessary to know the order in which the slices were acquired (Called the "interleave parameter”). Without this parameter, it is impossible to perform STC. This parameter should be stored in the fMRI file’s header during data acquisition, however, it is surprising how often such an important parameter is missing. Currently, no methods exist to retrospectively detect the interleave parameter from the fMRI data itself. This issue has become more pressing with the recent demands for sharing fMRI data collected with NIH/NSF funds. Sharing data without this parameter, as it is done in one of the largest online resting-state fMRI datasets (fcon_1000 [18]), reduces the validity of the results obtained with this data.

1.2.3 The Motion Problem

Numerous studies reported motion as the most detrimental source of noise and artifacts in functional magnetic resonance imaging (fMRI). Three major kinds of motion-induced artifacts are: 1) Misalignment, 2) Spin-history artifacts, and 3) k-space sampling artifacts. Different approaches have been proposed and used to attenuate the effect of motion on fMRI data, including both prospective and retrospective (post-processing) techniques. However, each type of motion (i.e. translation versus rotation or in-plane versus out-of-plane) has a distinct effect on the MR signal, which is not fully understood nor appropriately modeled in the field. In addition, effects of the same motion can be substantially different depending on when it occurs during the pulse sequence (e.g. RF excitation, gradient encoding, or k-space read-out). Thus, each distinct kind of motion and the time of its occurrence may require a unique approach to be optimally corrected. For example, retrospective techniques such as spatial realignment can correct for between-volume misalignment, but fails to address within volume contamination and spin-history artifacts. Because of the steady-state nature of the fMRI acquisition, spin-history artifacts rising from over/under excitation during slice-selection contaminate the MR signal even after cessation of motion, which makes it challenging to be corrected retrospectively. Prospective motion correction has been proposed to prevent these artifacts, but fails to address motion artifacts during k-space filling.

In an fMRI scan with a stationary subject, a given voxel samples the signal from one location in the brain throughout the entire scan. This is an important requirement in all fMRI statistical analysis. In general, any analysis will attempt to compare the time-series of each voxel to a reference time-series, under the assumption that the voxel is sampling the same location in the brain for the entire duration of the scan. However, if the subject moves part-way through the scan, a continuous signal from a single brain region can be sampled by different voxels over time. In order to view the BOLD signal from a single region, you must reposition the brain so that the same region falls on the same voxel for all volumes . This is typically done with a common motion correction routine known as "realignment". Realignment applies rigid body registration of each volume to a refrence, to make sure all acquired volumes spatially align with each other. If done properly, this will effectively realign each brain region with the same voxels over the entire scan.

Unfortunately, this does not completely solve the problem of motion. While it's possible to correct for misalignment between volumes, it's also possible for motion to cause misalignment *within* a single volume. Due to the slice-by-slice acquisition of fMRI, scanners acquire individual slices that remain fixed in space, even if the object is moving. If the object moves during the acquisition of a volume, stacking the slices for reconstruction results in a distorted brain volume, which creates a serious problem for most motion correction techniques today. This problem is demonstrated in Figure 1.7. When a stationary volume is acquired, parallel slices of the volume are sequentially excited and can be reconstructed accurately, as

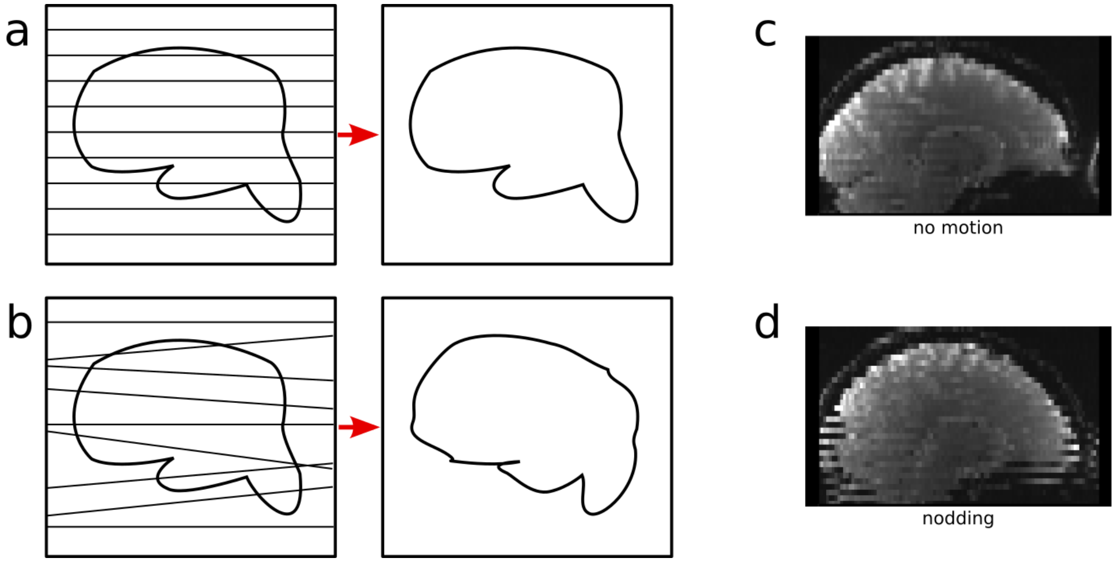

Figure 1.7: Motion-induced slice-misalignment artifacts in a single volume.

Motion that occurs during the acquisition of a volume will cause slice misalignment. a) A stationary object has parallel slices excited and acquired, which can be stacked into an accurate representation of the object. b) If the object moves during acquisition of the slices, the acquisition will no longer be parallel slices. When stacked for reconstruction, these slices will yield a distorted image. This is shown in real data in c and d, where c shows a stationary volume, and d shows a volume acquired when the subject underwent a nodding motion.

shown in Figure 1.7(a). However, if motion occurs during acquisition, the slices excited in the volume are no longer parallel to each other, and the reconstructed image is a distorted version of the true volume. The two volumes can no longer be registered using rigid body registration. Additionally, certain regions of the brain will have been over-acquired (Where slice lines intersect in Figure 1.7(b)), while other regions will have been completely skipped (Gaps between diverging slice lines in Figure 1.7(b)). This leaves a permanent, uncorrectable artifact in the fMRI image. This is shown with real data as well: In Figure 1.7(c), the subject is stationary for the acquisition of a volume. For Figure 1.7(d), the subject undergoes a nodding motion, and a banding pattern appears.

Currently, the recommended way to handle high-motion volumes is to simply remove, or “scrub” all motion contaminated volumes from a study. For studies in high motion subjects, such as children, this technique on average removes 25% of the data per scan, with some subjects having as much as 39% of their data scrubbed [19]. While this is bad for both resting state and task related fMRI, task based fMRI has yet another concern. Motion that’s even slightly correlated with the task can cause a statistical analysis to erroneously identify motion-contaminated regions as being neurologically active during the task[20], [21]. It’s evident that the effect of motion on fMRI, both task and resting, is extremely harmful, and the artifacts must be accounted for and removed. However, even under ideal conditions, if realignment is able to perfectly remove all motion from the scan, there is still a temporal misalignment that will cause problems for STC.

1.2.4 Interaction of STC and MC.

STC and MC are heavily intertwined processes. Surprisingly, there exists no consensus on the order in which these preprocessing steps should occur [22], [23]. In some ways, this is understandable, as STC and MC interact negatively regardless of the order they’re applied in. If motion correction is applied before slice timing correction, each volume will be rotated and translated into a reference position. Depending on the motion present, a single slice after realignment may have values interpolated from adjacent slices as a consequence of motion correction. Since each slice is sampled at a slightly different offset during the TR, the sampling rate of a voxel’s time-series after MC is not guaranteed to be uniform. STC applies a single timeshift to every voxel’s time-series in a given slice. Intuitively, this will be unable to address the slice timing problem on a non-uniformly sampled signal. Furthermore, even if the nonuniform sampling of these time-series could be accounted for, there would still be motion related artifacts in the image due to disrupted k-space sampling and spin-history artifacts. An illustration of this process is shown in Figure 1.8.

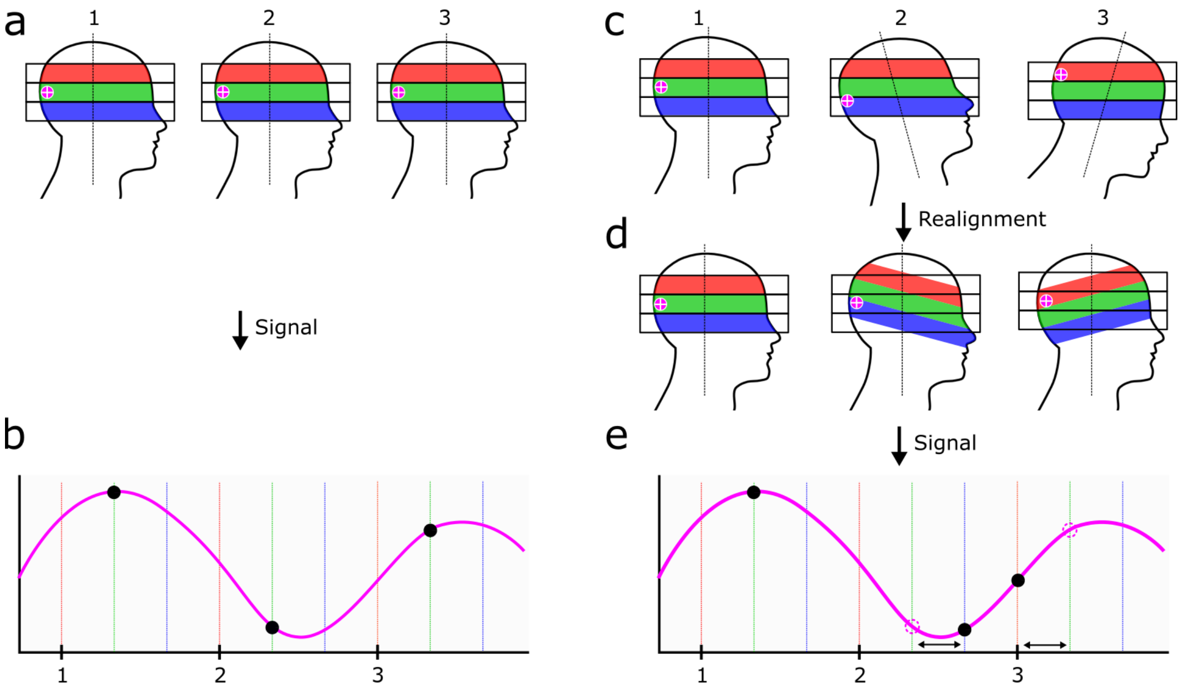

Figure 1.8: The Interaction of slice timing and motion.

Three slices are acquired sequentially, where the color indicates the temporal delay of the sample (First red, then green, then blue). (a) A stationary subject is scanned. A region of interest (ROI) in the brain, marked with a crosshair, has an underlying BOLD signal (The magenta line shown in (b)). Three volumes are acquired, and the signal sampled at the crosshair is plotted with black circles. These samples are uniformly spaced with a period of 1 TR. (c) A subject moves during scanning. In volume 1, the subject is in the same orientation as the subject in (a). In volume 2, the subject tilts their head back, causing the region of interest to move down into the blue slice. In volume 3, the subject tilts their head forward, causing the region of interest to move up into the red slice. (d) Realignment is then performed using rigid body registration, so that the subject appears stationary from volume to volume. However this does not fix the temporal delay of each sampled region, as indicated by the colored bars. Now, each slice has brain regions that were sampled at different temporal offsets. By examining the ROI, it can be seen that the same brain region has three different temporal delays over the course of three volumes (indicated by the changing color from volume 1 to 3). (e) The true sample times of this signal are plotted, and it can be seen that samples 2 and 3 are shifted from their intended sample times (which are indicated by the dashed circles), and do not follow a regular sampling interval, which is necessary for STC, or any signal processing step to be performed.

Conversely, applying STC before MC avoids the problem described above, but it introduces an entirely new kind of challenge. STC before MC shifts the time-series of each voxel with interpolation. However, if there's motion present, then different samples in the time-series may be from different brain regions, essentially concatenated together. Temporally interpolating potentially unrelated signals together is intuitively flawed. Essentially, STC and MC address two separate problems that arise in completely different domains. STC operates temporally and requires a full fMRI time-series which spans across multiple acquisitions, each of which will have unique motion profiles/artifacts, while MC operates spatially and can be applied to slices/volumes individually. This clearly demonstrates three important points: 1) There is no optimal order in which all artifacts caused by the interaction of motion and slice-based acquisition can be removed with current STC and MC routines. 2) The distinct nature of STC and MC require that each problem be addressed separately. 3) For optimal removal of STC and MC artifacts, a new MC routine must be developed that corrects for artifacts due to spin-history and disrupted k-space sampling in order to be effective.

1.3 Specific Aims

MRI samples a relatively weak signal that is easily overpowered by sources of noise. On top of this, fMRI measures extremely small fluctuations in voxel intensity. This means that the ability to remove artifacts from the signal is critically important to maximize the validity and power of any statistical findings. To this end, a vast array of preprocessing tools have been developed in the field that attempt to remove as many confounds as possible. However, many of the algorithms used in these steps, particularly in STC and MC, are not derived from the principles of signal processing and sampling theory.

The purpose of this thesis is to enhance our understanding of the fMRI signal, STC, MC, and their interaction with each other. Using these observations, novel processing algorithms are developed to correct for slice timing and motion, based in a foundation of signal sampling theory. These novel STC and MC routines are developed in context of a full preprocessing pipeline, and so their order of application can no longer be arbitrary. The development and testing of these algorithms was carried out on both real and simulated data. To this end, the work was divided into three specific aims:

1) To maximize the utility of a novel STC routine, the interleave parameter must be known for any fMRI data set. A method to detect the interleave parameter from the unprocessed fMRI time-series is developed and evaluated across multiple data sets from numerous study sites.
2) To optimize the STC preprocessing step, the BOLD signal and fMRI time-series is examined from a physiological and signal processing standpoint. From this, we develop a STC routine that will optimally reconstruct the BOLD signal at any offset using signal sampling theory. Our routine is validated using real and simulated fMRI data.
3) To create an optimal motion correction routine, the physical origin of the fMRI signal, and the effect motion has on it, is examined using the Bloch equations. The conclusions reached from this analysis are used to develop a novel motion correction algorithm which operates directly on the raw data and effectively removes all motion artifacts from the reconstructed signal. This method is tested in physics-based fMRI simulations, as well as real data.

1.4 Significance

Magnetic resonance imaging is an extremely powerful diagnostic and investigative tool to both the medical and research fields alike. Before the commercial availability of the modern MRI machine, internal anatomy could be viewed with comparable resolution using a CT scanner, but with the absence of any functional information. On the other hand, PET scanners allowed scientists to take functional images of the body, in the absence of any structural information, and at relatively low resolution. MRI allows us to image both structure and function from the same machine, without the need for exogenous contrast.

An important fundamental difference between MRI and CT or PET is that MRI uses no ionizing radiation for imaging. CT uses multiple X-rays to construct an image, and so the amount of radiation absorbed during a typical chest CT scan is equivalent to what you would absorb naturally over 2 years from background radiation. PET scans also require some form of radioactive tracer to be injected into the body, and the radiation in a typical FDG PET scan is of a similar level to that of a chest CT [24]. On the other hand, MRI uses only magnetic fields and RF excitation pulses. Aside from the presence of metallic or conductive objects, the primary safety concern of MRI is tissue heating due to repeated exposure to high energy RF pulses [25]. As field strength on MRI machines increase, this concern becomes larger, as the pulse sequences require more and more power to achieve the same images [26]. Injuries due to RF heating do still occur, and are typically related to some kind of device, implant, or lead on the patient. Of the millions of MRI scans performed in the US each year, the FDA receives only around 300 adverse event reports, the majority of which are heating or burns, making it an extremely safe imaging modality [27].

fMRI is not just a tool used to study human cognition. In fact, fMRI (and MRI in general) is extremely versatile in its application. fMRI can be used in drug therapy, to examine how different substances alter the response in the brain [28]. fMRI can be used to study functional changes in the brain when effected by neurological diseases such as parkinsons, depression, type 2 diabetes, insomnia, alzheimers, autism, and more [29]–[35]. By studying these changes, scientists can develop a greater understanding of the disease, which can lead to more effective treatments, and can help direct future research in a more focused direction.

Because MRI has the unique ability to see both structure and function, it is an extremely attractive tool for researchers studying the human brain. A high resolution structural image can be acquired immediately before a functional scan, providing an accurate template to align the functional image to. Because of the safety of fMRI and no requirement for external contrast, brain function can be scanned for any length of time, limited only by the subject's comfort in the scanner. This means that more functional scans can be taken without risk of harming the subject. This has allowed an explosion in large-cohort brain studies of both healthy and diseased populations. These large cohorts allow researchers to examine numerous aspects of the human brain in exquisite detail, such as network connectivity and precursors of disease onset. This allows researchers to better identify subjects with a larger risk for diseases before clinical onset. Such analysis would be difficult to do with smaller numbers of subjects, and the results would not be nearly as robust. Massive scanning projects such as the Human Connectome Project [36] have helped push forward in these areas, leading to a better general understanding of cognition and development [37].

However, the relative safety of MRI does not mean that an arbitrary number of scans can be given to collect large amounts of data. Given the cost of scan time, and the comfort of the subject, it's important to be as efficient as possible during scanning. Most task based scans are usually between 100 to 300 volumes, and resting state scans are rarely more than 15 min long, giving them potentially up to 900 volumes for a typical scan. However, the analysis done on resting state scans requires these additional volume for better accuracy [38]. In a clinical population, an average of 25% of these scan volumes will have sufficient motion contamination to be rendered useless, and are discarded. This significantly reduces the statistical and diagnostic power of these scans, resulting in longer scans or inconclusive analysis.

For clinical studies where thousands of subjects need to be scanned, potentially multiple times, losing 25% of all fMRI scans is an enormous scientific and financial loss. Even if these volumes are recovered, improper preprocessing can hurt the resulting analysis. By developing preprocessing tools that eliminate artifacts as completely as possible, and adhere to sound signal processing theory, many of these losses can be eliminated, and the overall strength of the study can be enhanced. The methods developed in this dissertation are directly applicable to any fMRI scan acquisition, and indeed for any MRI imaging modality that is sensitive to motion.

2 Recovery of Interleave Parameter From fMRI Data

2.1 Introduction

Without knowledge of the slice acquisition order, the critical preprocessing step of STC cannot be applied. Developing an optimal STC method is useless in practice if a data set is missing information on its slice acquisition. As fMRI data are typically acquired with interleave acquisition, it's common to summarize the acquisition order with a single "interleave parameter", which describes how many slices are skipped between acquisitions. For example, an interleave parameter of "2" means that every 2nd slice is acquired. Most interleave routines are standardized in a way that an entire acquisition order can be reconstructed from this single parameter. This chapter focuses on the development of a method to retrospectively extract the interleave parameter using only the 4D fMRI time-series.

2.1.1 Temporal Correlations in fMRI

The spatiotemporal fMRI signal, $f(\boldsymbol{r},t)$, is an inherently smooth but noisy signal (A smooth hemodynamic response with noise) which is sampled at a rate of 1/TR Hz. A conventional fMRI signal consists of four dimensions, three spatial Cartesian directions, $\boldsymbol{r}=(x,y,z)$, and one time component t. One important measure used in many fMRI studies is the *temporal* correlation of the fMRI signal between different voxels. The temporal correlation function between two points, **r** and **r**′, is given by the following equation:

$$\rho(\boldsymbol{r},\boldsymbol{r}')=\frac{1}{N}\sum_{t}^{N}\frac{\left(f(\boldsymbol{r},t)-\overline{f(\boldsymbol{r},t)}\right)\left(f(\boldsymbol{r}',t)-\overline{f(\boldsymbol{r}',t)}\right)}{\sigma_{f(\boldsymbol{r},t)}\sigma_{f(\boldsymbol{r}',t)}} \qquad (2.1)$$

where N is the number of samples in temporal domain, and $\overline{f(\boldsymbol{r},t)}$, and $\sigma_{f(\boldsymbol{r},t)}$ are the temporal mean and standard deviations of signal $f(\boldsymbol{r},t)$, respectively. Note that $\rho(\boldsymbol{r},\boldsymbol{r}')$ is a six dimensional correlation function, giving a distinct 3 dimensional correlation map for each voxel. These correlation maps are the basis for many resting-state and functional connectivity fMRI data analyses.

2.1.2 Temporal Autocorrelation Function

Using the equation above, a voxel's correlation with itself (where $\boldsymbol{r}=\boldsymbol{r}'$) is 1. This is also the highest correlation a given voxel will have with any other voxel. The correlation of a signal to itself is referred to as the temporal autocorrelation. However, as a signal's correlation with itself is always 1, this measure is rather uninteresting until temporal shifts are considered. To calculate the autocorrelation of a signal with a shifted version of itself, we rewrite equation (2.1) as a cross correlation:

$$\rho_{\boldsymbol{r}}(t,t') = \frac{1}{N}\sum_{t}^{N}\frac{\left(f(\boldsymbol{r},t) - \overline{f(\boldsymbol{r},t)}\right)\left(f(\boldsymbol{r},t') - \overline{f(\boldsymbol{r},t')}\right)}{\sigma_{f(\boldsymbol{r},t)}\sigma_{f(\boldsymbol{r},t')}} \qquad (\ 2.2\ )$$

Now the correlation between a single voxel at point $\boldsymbol{r}$ is being calculated for itself and a time-shifted version of itself, where $t' = t - \tau$. One important observation about the temporal autocorrelation is that its maximum is when there is no offset, and $t' = t$. Typically, the larger the offset τ becomes, the lower the autocorrelation value is. There may be local minima and maxima as τ increases, but a typical autocorrelation function for a BOLD fMRI signal is largely monotonically decreasing, as shown in Figure 2.1. A fundamental but important observation can be made from this: given a continuous signal, two samples taken close together in time are

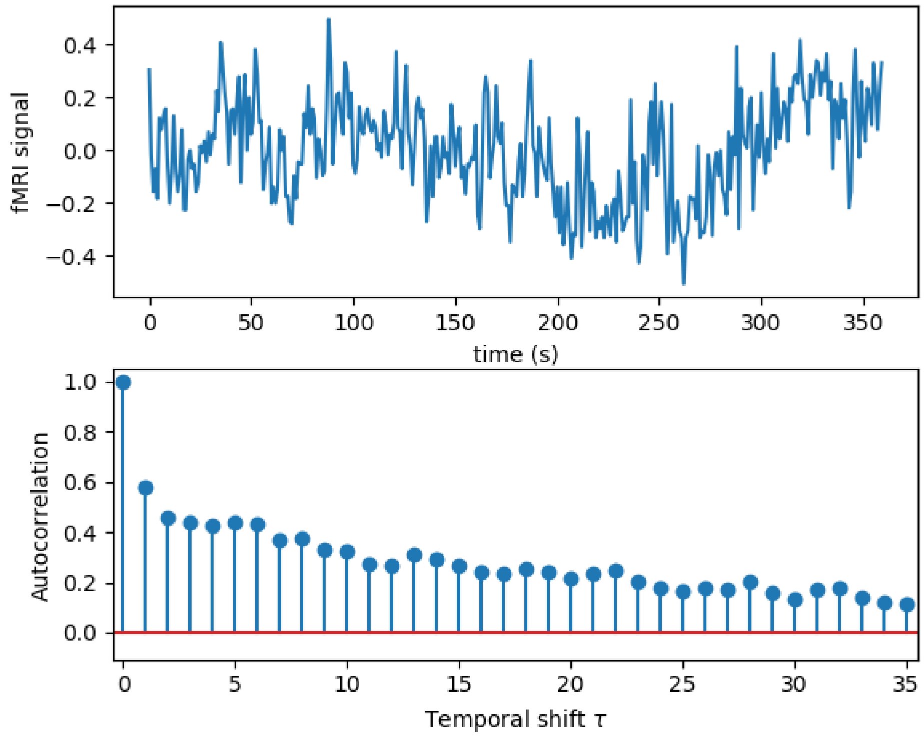

Figure 2.1: Typical fMRI autocorrelation.

(Top) A typical fMRI time-series from a gray matter voxel, normalized. (Bottom) The autocorrelation of this signal given a temporal shift τ, described by equation (2.2).

likely going to be more similar than two samples taken further apart. Another way of saying this is that as temporal delay τ increases, the correlation decreases.

2.1.3 Spatial Correlation Functions

Much like a temporal correlation, a spatial correlation can also be calculated. A spatial correlation compares the similarity of two regions in space. In fMRI, this can be the correlation of one slice to another within a given volume. Much like a temporal correlation, a given slice will have a maximum correlation with itself, and will have lower correlations with other slices. Given the spatially varying anatomy of the head, the further away two slices are, the lower their spatial correlation will be. Much like the temporal autocorrelation, this is a monotonically decreasing function. An example of a typical fMRI spatial correlation across slices is shown in Figure 2.2.

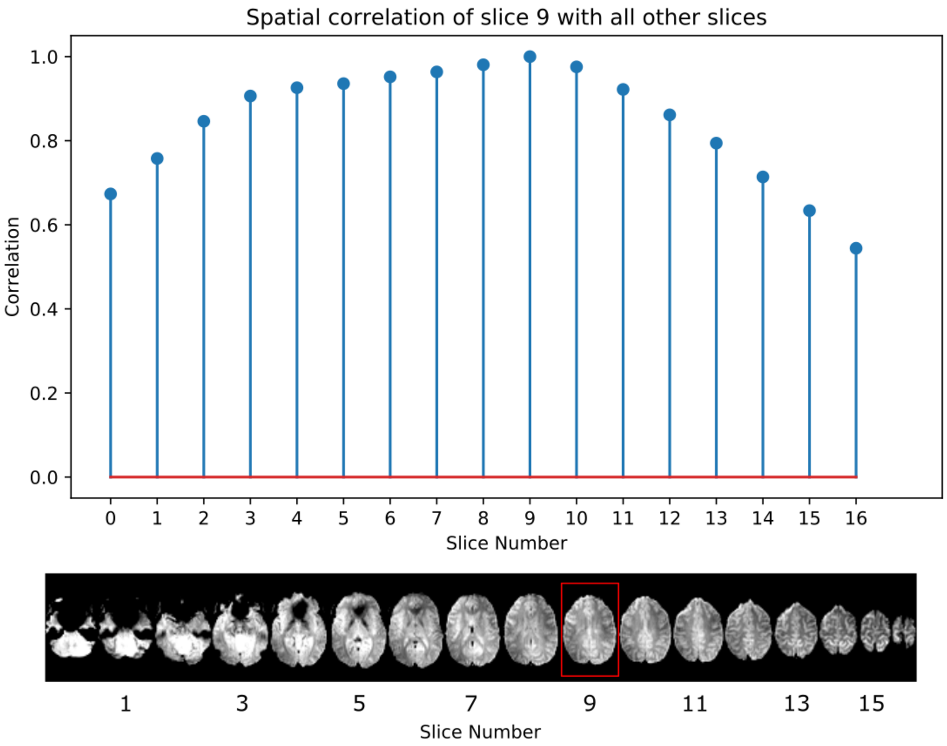

Figure 2.2: Spatial correlation of a typical fMRI volume.

(Top) The spatial correlation of a reference slice (slice 9) to all other slices in a typical fMRI volume. (Bottom) The corresponding slices used for the correlation calculations.

2.2 Methods

2.2.1 Temporal Distance Correlation Function

Given the properties of the temporal and spatial autocorrelations, we can expect that the overall correlation between two voxels will depend on their distance, both spatially and temporally. The spatial distance refers to the Euclidean distance between two voxels. The temporal distance refers to the offset at which the time-series' were sampled due to slice-sampling. We define a function to describe this called the "temporal-distance correlation function" of the fMRI signal. The temporal distance correlation function is the average of all temporal correlations of voxel pairs that are spatially located specific distances and directions from each other. In general, a temporal-distance correlation function is a two dimensional function, with one axis indicating the absolute Euclidean distance, and another giving the direction in which the voxel pairs are located. In its most general formulation, it is given by following equation,

$$\xi(\eta, d) = \frac{1}{m} \sum_{\forall\, r,r\prime,\ \ |r-r'|=\eta\ \&\ \measuredangle(r-r')=d} \rho(\boldsymbol{r}, \boldsymbol{r}') \tag{2.3}$$

where m is the total number of voxel pairs found in the fMRI data that are located within a distance of η and direction of d. In addition, $|\boldsymbol{r} - \boldsymbol{r}'|$ is the length, and $\measuredangle(\boldsymbol{r} - \boldsymbol{r}')$ is the angle of the vector connecting $\boldsymbol{r}$ to $\boldsymbol{r}\,'$. In general, d needs to have more than one dimension to cover the entire 3D space of the fMRI volume. However, for the purpose of STC, we are only interested in the evolution of this function along the axes that the data are acquired in, being the Cartesian axes (x, y, z). For instance, $\xi(2, z)$ is the temporal-distance function for all the voxel pairs that are located exactly 2mm from each other along the z axis.

Due to the properties of spatial correlations, as the spatial distance between two points $(\boldsymbol{r}, \boldsymbol{r}')$ increases, the temporal-distance correlation function monotonically decreases. This simple characteristic of the temporal-distance correlation function should be observed across all three axes, as seen in Figure 2.3a. In this figure, the temporal distance correlation function decrease slowly and in a nearly identical manner along the x and y axis (Blue and green lines). This is because voxels along the x and y axis are sampled at the same instant in time, and so they only suffer from spatial decorrelation as their Euclidean distance increases. The temporal distance correlation function along the z axis decreases much faster than along the x and y. This is because the z axis experiences both spatial and temporal decorrelation, due to the slice-based acquisition of fMRI.

In Figure 2.3a, the correlation along the z axis has a monotonically decreasing value because the slices are acquired sequentially. However, with interleaved slice acquisition, this decreasing monotonic trend will be disrupted along the slice selection axis, as seen in Figure 2.3b. This disruption is due to the fact that neighboring voxels along the z axis are not sampled immediately after each other in the interleaved slice acquisition protocols. It is clear from this that the temporal decorrelation is more detrimental than the spatial decorrelation. Based on this simple property of the temporal-distance correlation function, the interleave parameter can be recovered from the raw, unprocessed fMRI data.

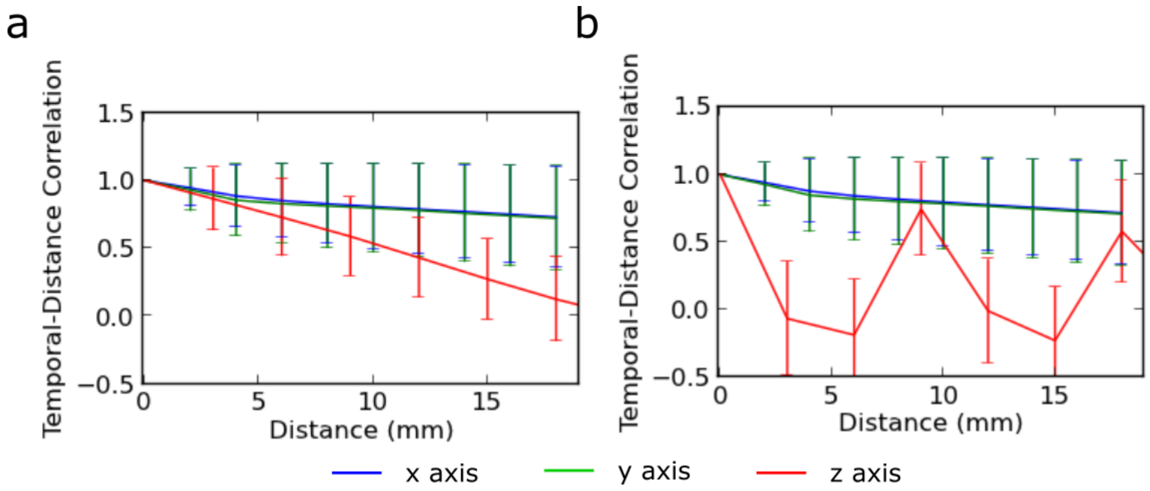

Figure 2.3: fMRI temporal distance correlation function for sequential and interleaved data. The temporal distance correlation function is calculated along all 3 axes for sequentially acquired data (a) and interleaved data (b). The temporal distance correlation function decreases faster along z than it does for x and y. This is because the z axis is the slice selection axis, meaning that voxels along z are offset both spatially and temporally. However, each slice is acquired instantaneously, so along x and y there is only spatial decorrelation. The effect of temporal decorrelation is even more dramatic in (b). The peaks along the z axis line in (b) indicate slices that were acquired next in the sequence, which have higher correlations than their neighbors even though they're spatially further away.

2.2.2 Interleave Parameter Extraction

In simulated data, the fMRI interleave parameter can be reliably extracted as the first local maximum of the temporal distance correlation function along the slice selection axis. Even though the temporal-distance correlation functions monotonically decrease by increasing the distance η, there is a significant amount of variation in the temporal-correlations at each η, as shown by the standard deviation bars in Figure 2.3. There are many sources contributing to these variations, such as local neuronal activity, involuntary head motion, and physiological noise. In the real data these variations are even larger and often obscure the clear peak along the z axis. To solve this issue, a dimensional reduction can be performed before computing the temporal correlations to help average out much of this noise.

One way to perform dimensional reduction would be to average the temporal distance correlation function across all voxels. However, computing the temporal distance correlation for all voxels in the first place is a computationally intensive process. It would be better to perform this reduction on the raw data itself before the temporal correlation function is calculated. Fortunately, averaging the data before computing a single correlation is equivalent to computing all the correlations and then averaging, save for a scaling offset. This is demonstrated in appendix A.

Dimensional reduction is performed on the data by averaging within each slice. Averaging the signals of all voxels within a slice will reduce the variations of the signals due to factors other than interleaved slice acquisition, while preserving the variation due to slice timing between two adjacent slice signals. For instance, given an fMRI signal $f(x, y, z, t)$, a slice average over the x/y plane can be obtained with equation (2.4):

$$f_{slice}(z,t) = \frac{1}{NM}\sum_{x}\sum_{y} f(x,y,z,t) \tag{2.4}$$

where N and M are the number of voxels in the x and y axes, respectively. This is called a *slice signal*. Equation (2.4) can be re-formulated for the other two planes (x/z, y/z) as well. In our x/y averaged signal, each slice along the z axis has an averaged slice signal, and their spatial correlation is given by $\rho\big(f_{slice}(z,t), f_{slice}(z',t)\big)$. By plotting every possible pairwise correlation of the slice signals, a matrix of correlations can be created, as shown in Figure 2.4. This matrix is called a cross-correlogram.

An fMRI image sampled sequentially (no interleave) will have a correlation pattern similar to the one shown in Figure 2.4a. The series of “1’s” along the diagonal axis represent the correlation of a slice compared to itself, which is always the maximum. Moving away from the diagonal axis, we see a generally decreasing function as we compare a slice to slices further and further away.

In an interleaved fMRI image, we would expect slices to have a higher correlation with those slices sampled immediately before or after them, than with slices sampled at some later time. We see this in Figure 2.4b. In our analysis, this appears as additional diagonal “stripes” in the cross-correlogram. These stripes indicate an increase in the correlation of two spatially separated slices, which is consistent across the entire image. The distance between these stripes is the interleave value.

Even after dimension reduction, there are cases where the cross-correlogram is noisy, and not as clear as the one shown in Figure 2.4b. Because of this, a simple peak detection algorithm is insufficient to reliably extract the interleave parameter. In some images, the interleave slice is not always indicated by a sharp peak as shown in Figure 2.3b. Instead, the correlation may gradually increase until the interleave

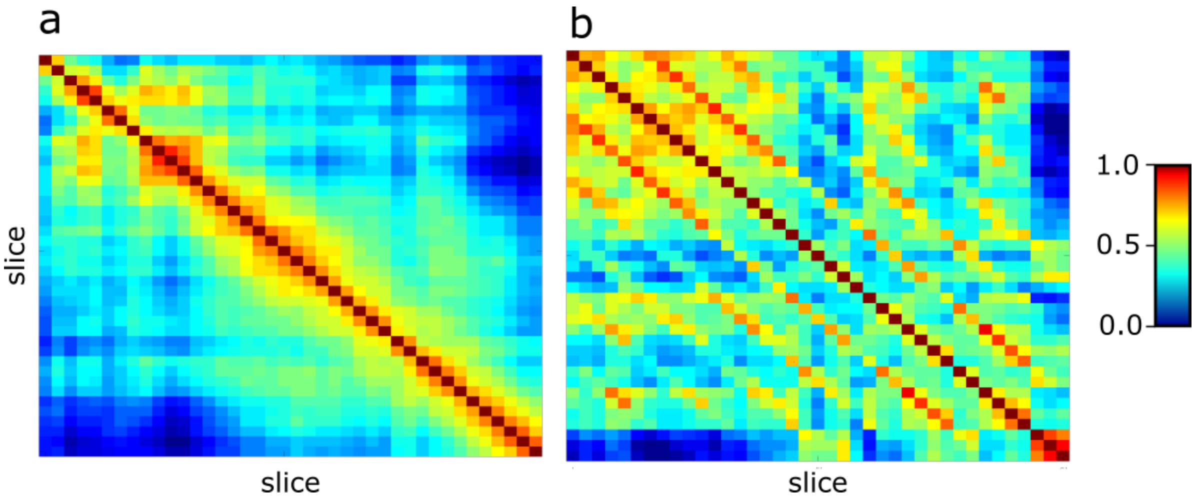

Figure 2.4: Cross Correlegram of sequentially acquired and interleaved data.

The cross correlgram is calculated for two datasets. First, the slice signal is calculated for each slice. Then, the temporal distance correlation is computed for each slice signal to all other slice signals. This is done for sequentially acquired data (a) and interleave acquired data (b). For sequential data, there is a smooth decrease in the correlation function as you move away from the diagonal. For the interleaved data, there are clear peaks, evenly spaced every 6 slices as you move away from the diagonal. In this case, 6 is the interleave parameter of that data.

slice is reached, at which point it decreases rapidly. Through observation it was determined that the second derivative of the signal, in those cases, provides a better indicator of where the first interleaved slice is taken. This is shown in Figure 2.5. The average cross correlogram over all slices is plotted in Figure 2.5(a). The true interleave value in this example is 6, meaning there should be a peak 6 slices away from slice 1. While there is technically a peak here, it is extremely small, and very similar to the surrounding values. Figure 2.5(b) shows the averaged second derivative of this subject's cross correlogram. We now see a large drop at slice number 7. Though it is clear from Figure 2.5 that the second derivative easily picks out the global maximum, there are still cases in which it also fails to do so; specifically in an even-odd interleave, where many local minima may exist. In these cases, statistical inference can be used to provide a measure of certainty in the detected interleave parameter.

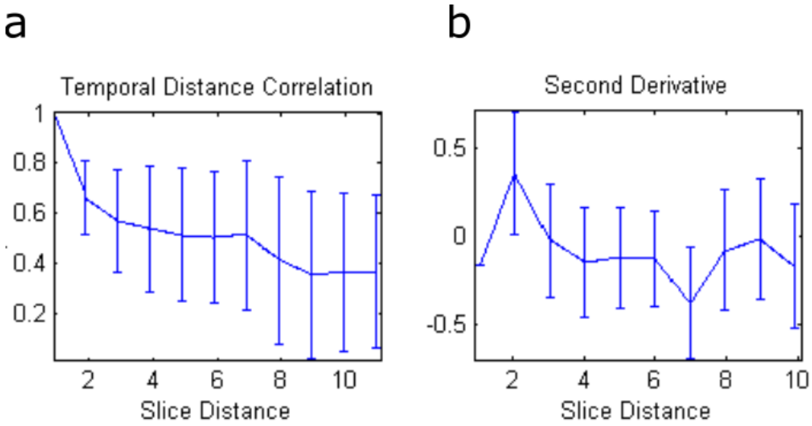

Figure 2.5: The average temporal distance correlation function and its second derivative. The average temporal distance correlation function over all slices in real data is plotted in (a). A peak in this plot would indicate the interleave parameter of the scan. While there is an extremely small peak at slice 7, it's too similar to its neighbors for an algorithm to reliably detect it. To aid this process, the second derivative of each slice's temporal distance correlation function is taken, and averaged across all slices, shown in (b). In this plot, there is a much clearer trough at slice 7, which is used as the primary feature for interleave parameter detection.

2.2.3 Statistical Inference

We perform a simple statistical analysis to detect the local minimum that is most significantly different from its neighbors. We identify all local peaks in the original data, and all local troughs in the second derivative. Each peak and trough is compared to its neighboring samples using a basic student t-test, giving two p-values per peak/trough, describing the significant difference of the peak/trough to its neighbors. The significance of each peak/trough is "averaged" as the geometric mean of the p-values. The peak with the most significant p-value is taken as the interleave estimate from the original data, while the trough with the most significant p-value is taken as the interleave estimate from the second derivative, which are not necessarily the same values. If both the temporal-distance function and its second derivative select the same interleave value as most significant, then that value is reported as the interleave parameter. Otherwise, the most significant minimum of the second derivative is selected unless the value from the original function is more significant by an order of 10^{α}. We biased our decision towards the second derivative, because it often gives more accurate results. We set $\alpha = 1.5$ in our examination, which gave the most accurate results overall. However, others might find that different values optimize their process. This statistical analysis helps detect the interleaved parameters in extremely noisy and hard-to-detect cases. Low certainty values may require a manual inspection of the data to verify the interleave value.

2.2.4 Validation on Real and Simulated data

We used both simulated and real data to examine the success rate of the detection method proposed in this paper. Using the method described in [39] to generate our simulated data, we generated 10 minutes of scan, with in-plane resolution of 112x112, and 37 slices with voxel size 2x2x3 mm^3 and a TR of 2 seconds. A neuronal stimulus sequence containing 20 pulses with random onset (at least 10s apart) and width (5 to 30 second) was independently created for each ROI. The neuronal stimulus sequences were convolved with the canonical hemodynamic impulse response function included in SPM to generate the underlying BOLD signal. Subsequently, cardiac (f=1.005 Hz) and respiratory (f=0.25 Hz) noises were added to the signal. To simulate the interleaved slice acquisition, the original high frequency sampled signals (f_s=20 Hz) were subsampled with f_{ss}=0.5 Hz and with a time-shift specifically set for each slice according to the interleaved parameter. Ten scans were generated each with 6 different interleave parameters, from one to six (one indicating no interleave). To simulate the head motion, we displaced each volume of the simulated fMRI data using different transformation matrices. The transformation matrices were obtained from real subjects' involuntary movements in the scanner using typical re-alignment algorithms.

Real data were obtained from our group's on-going studies of task-based and resting-state fMRI data as well as datasets collected outside our group. 56 resting-state and 300 task-based fMRI data with interleave parameters of 6, as well as 205 task-based fMRI with even-odd interleave were examined. To expand the examination of our method to datasets collected outside our group, we examined 474 randomly selected fMRI images from the *fcon_1000* dataset [18], which is available online for public use.

2.3 Results

The developed algorithm detected the interleaved parameter in all 60 simulated images with 100% accuracy. For 356 on-site fMRI data images acquired with an interleaved parameter of 6, the detection accuracy dropped to 91%. For the 200 task-based fMRIs with even-odd interleave, the accuracy was 93%. For the 474 randomly selected resting-state fMRI scans from *fcon_1000* dataset, the accuracy was 97%. It is important to note that the *fcon_1000* dataset is collected in 23 sites, each with different scanner and acquisition pulse sequence. Some images were excluded from this group, as it was unclear whether the algorithm was correct or incorrect upon manual inspection.

2.4 Discussion

STC, as an important pre-processing step of fMRI data, cannot be implemented without knowledge of the interleave parameter. In the case of fMRI data header files, finding the correct interleave parameter is a nontrivial task- especially for old data shared online with minimal or no explanation. This was so problematic that some of the neuroimaging software packages suggested removing STC from their pre-processing pipeline, despite many studies emphasizing its necessity [3]. In this chapter we proposed and developed a technique which retrospectively detects the interleave parameter, using only fMRI data. We showed successful detection of the parameters on simulated data and a very high success rate on in-house and off-site fMRI data. Our technique is built upon a very simple property of temporal-distance correlation functions in spatiotemporal fMRI signals. In addition, we shared the developed Matlab function on our lab webpage as well as github for public use [5]. With this problem addressed, STC can now be applied on any data set even with missing slice order information. Now that STC can be applied to any fMRI scan, an optimal STC method can be developed for universal application to any dataset.

3 Optimal Slice Timing Correction

3.1 Introduction

STC is fundamentally a temporal process that requires a full time-series to operate on. Using the assumption that an fMRI scan has no motion, or has had motion optimally corrected for, STC can be thought of as a purely signal processing problem, outside of the context of fMRI. This chapter focuses on the derivation of an optimal STC routine, its development for use on fMRI images, and its validation in a wide range of scan conditions.

3.1.1 Existing Methods of STC

STC accounts for a given slice's temporal offset by interpolating the signal in the reverse direction of the imposed offset delay. This is an important step in fMRI, as the benefits of STC have been shown in numerous studies [40], [41]. The slice-timing problem arises from the fact that the offset $\varphi(z)$ changes across slices as a function of z. Conventional interpolation-based techniques operate on the discrete signals and estimate the value between sample points. Mathematically this can be represented by the convolution of the sampled signal, $f[\boldsymbol{r}, n]$ with an interpolation kernel h:

$$\hat{f}[\boldsymbol{r}, n] = \sum_{k=0}^{N-1} f[\boldsymbol{r}, k]\, h(\,nT_s - k - \varphi(z)) \tag{3.1}$$

where $\hat{f}$ is the shifted/interpolated signal.

It should be emphasized that while all interpolation can be represented as upsampling, filtering, and downsampling, it is the shape of a kernel's frequency response $H(\omega)$ that determines the quality of the reconstructed signal. An ideal boxcar frequency response would perfectly reconstruct the sampled signal, reducing interpolation error when resampling at an offset. Therefore, the more an interpolation kernel resembles a boxcar, the better it does at reconstructing the signal. Two widely used fMRI data analysis software packages, statistical parametric mapping (SPM) [42] and FMRIB software library (FSL) [43], use different version of *sinc* interpolation (SPM: *sinc*, FSL: Hanning window *sinc*) for their STC module. Figure 3.1 shows the time and frequency domain of these kernels, as well as the frequency domain of an ideal boxcar.

Sinc interpolation can be represented as convolution of the fMRI signal with the following kernel,

$$h_S(t) = \frac{\sin(\pi t/T_s)}{\pi t/T_s} \tag{3.2}$$

Figure 3.1 shows the time and frequency domain of this kernel. It should be emphasized that ripples in the pass band of the *sinc* kernel are due to truncation of the signal in the time domain, and become worse as the signal is truncated further. To attenuate the rippling artifact, a smooth window function is often applied so that the kernel reaches zero by the final time point with no discontinuities. FSL uses a Hanning window for this purpose, which is described as:

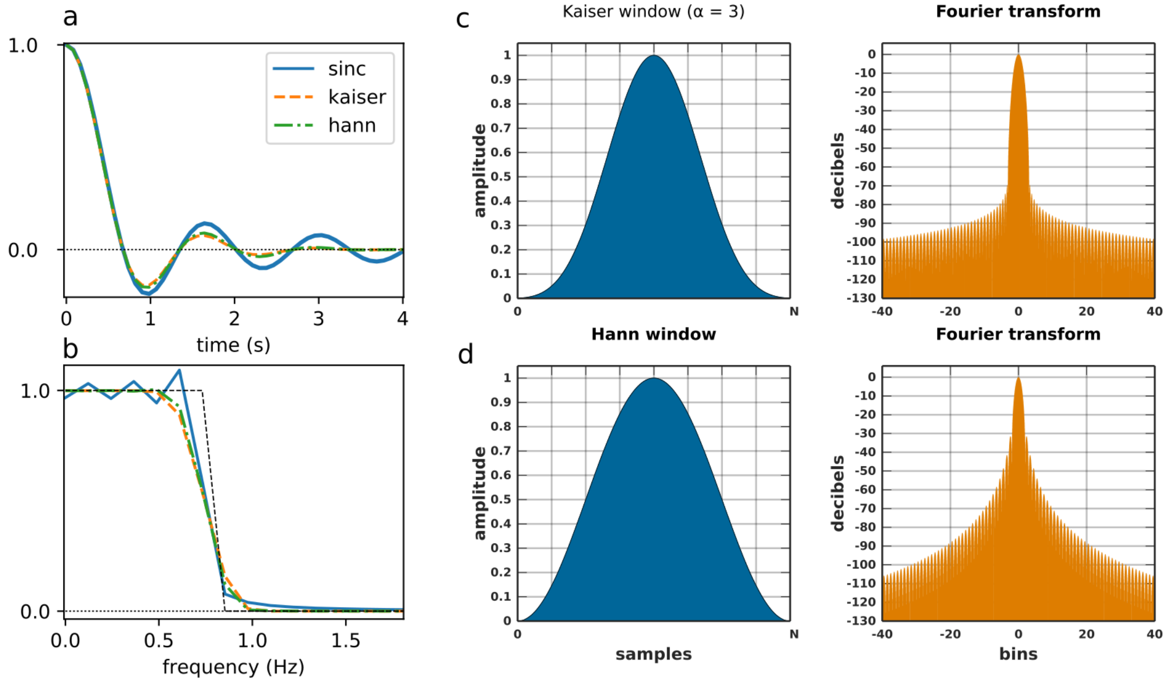

Figure 3.1: Time and frequency domain plots of kernels for sinc, Hanning window sinc and Kaiser window sinc.

(a) The time domain representation of a sinc function smoothed with a Hann and Kaiser window. (b) The frequency domain of these kernels, with an ideal boxcar filter outlined as a black dashed line. It is clear from this that the smoothing windows both prevent ringing in the pass band of the filter, which is seen in the truncated non-windowed sinc (Blue line). While both the Kaiser and Hann window appear to behave similarly, there are more obvious differences in the frequency domain of each window. (c) and (d) show the time domain and frequency response of a Kaiser window and Hann window respectively, with their fourier transform. It's clear from this image that the Kaiser window provides a steeper cutoff, as well as better stop-band suppression for all but the highest frequencies.

$$w_{hann}(n) = 0.5\left(1 - \cos\left(\frac{2\pi n T_s}{T_s N - 1}\right)\right) \tag{3.3}$$

where N is the length of the sequence. By examining the frequency domain of this kernel we can see that much of the rippling has been removed, however some still remain.

3.2 Methods

3.2.1 Sampling Theory

Shannon-Nyquist sampling theory states that a signal can be optimally reconstructed if the sampling rate is twice the maximum bandwidth of the original signal. In fMRI, the signal of interest is the underlying BOLD signal. If we assume that the canonical double gamma HRF curve (commonly used in linear modeling of hemodynamic responses) is realistically close to the shape of the real HRF, then spectral analysis of this curve reveals that the hemodynamic response function has 99.9% of its energy in the frequency range of [0, 0.21] Hz, as shown in Figure 3.2.

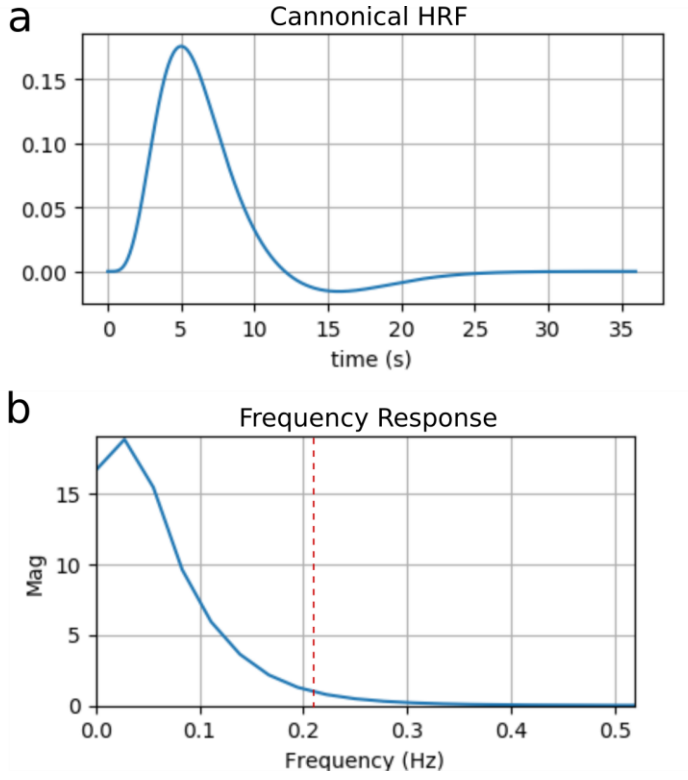

Figure 3.2: The Cannonical double gamma HRF and its frequency domain.

a) The canonical double gamma HRF, which was designed from experimentally derived data. b) The magnitude of the frequency domain of the HRF. The red dashed line indicates 0.21 Hz, marking the upper frequency that contains 99.9% of the signals energy.

According to the Shannon-Nyquist sampling theorem, this means that the BOLD signal can be fully recovered, no matter the sampling delay, if the signal is sampled faster than 0.41Hz. A typical fMRI sampled at 0.5 Hz (TR = 2 seconds), so this is sufficient to reconstruct the signal completely. This theoretical concept is the foundation of our proposed optimal method for STC.

3.2.2 Low-pass Filter Design

The optimal low-pass filter is a continuous *sinc* function, which extends infinitely in both directions away from the origin. Because a signal cannot be sampled infinitely, a truncated version of the sinc function is used in digital signal processing. The more truncated a sinc function becomes, the more ringing is present in its frequency domain. This ringing will lead to an inaccurate reconstruction, and is best to minimize. A simple solution to this problem is to simulate a longer sinc function. However, arbitrarily increasing the length of the sampled sinc function also has its drawbacks. Generally, every digital filter needs to operate on a certain number of initial time points before it can function properly. This is called the initialization period, which is ½ the length of the filter. Thus, for any signal filtered with a filter of length N, the first N/2 and last N/2 time points of the filtered signal are not considered accurate. If the filter length is comparable to the length of the time-series being filtered, this can result in substantial loss of reliability for many of the time-points. Because of this, shorter filters are desirable, in order to minimize the initialization period. One final challenge with filter design is that any discontinuity will also result in ringing in the pass-band of the frequency domain. This means that if the final points in the sampled *sinc* function do not smoothly transition to zero, the reconstructed time-series may have errors.

We employ three strategies to mitigate these filter-design challenges, which are discussed in detail here: 1) A tradeoff between high filter order and pass-band ringing is established, choosing a slightly larger order than is found in most slice timing routines. 2) Odd-symmetric padding is applied to minimize errors in the initialization period. 3) A window function is applied to the sampled *sinc* function to ensure the filter gradually converges to zero.

Upsampling is the first step in image reconstruction. When STC is applied, the data must be resampled at a temporal offset to account for the sampling delay of a given slice. Even with temporal upsampling, if this offset is not a factor of the higher sampling rate, then additional interpolation will be necessary. For this reason, it's optimal to choose a frequency that is a multiple of N_s/TR Hz, where N_s is the number of slices. The simplest implementation of this is to just use N_s/TR Hz as the upsampled frequency, which perfectly aligns the sampling times of the upsampled signal with the acquisition time of each slice. For example, an fMRI volume with a TR of 2 seconds and 30 slices would be upsampled to 15Hz. Thus, in 2 seconds, there are 30 samples, each corresponding perfectly with the acquisition time of a slice.

Even with upsampling, padding is necessary to reduce the artifacts in the initialization period of the filter. For our STC method we addressed this issue with the following tactic: Padding is applied using an "odd" reflection scheme, where the padding is carried out by reflecting the time-series, and subtracting the reflected values from 2x the edge values. This scheme prevents the introduction of high frequency artifacts that may be present when a simple mirror padding routine is applied. This is especially obvious in data with an increasing or decreasing linear trend, which is common in fMRI (Referred to as scanner drift). An

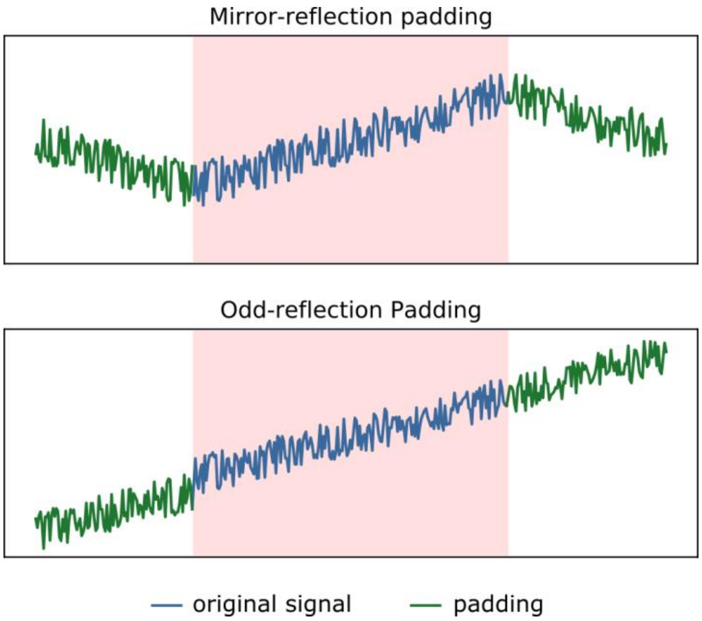

Figure 3.3: Mirror padding vs Odd padding.

A time-series is padded using two different techniques. The original time-series is shown in blue, within the pink box. Samples outside this range are shown in green, and are added by the respective padding routines. In mirror padding (top), the time-series is simply appended to itself in reverse order. This destroys linear trends, and introduces high frequencies not present in the original data. In odd padding (bottom), linear trends are preserved, and a more representative time-series is created.

example of this is shown in Figure 3.3, where mirror padding introduces abrupt changes in the time-series, while odd padding continues the linear trend. Only half of the time-series is reflected on the front and back of the signal, so the total length of the padded signal is twice the original. This allows us to use higher order filters with larger initialization periods.

For our STC method, a Kaiser window is added to the *sinc* interpolation kernel to help smooth the ends of the signal and remove any discontinuities, allowing for a shorter sampling of the *sinc* function, resulting in a lower order filter. A Kaiser multiplicative windowing function offers less pass-band rippling and faster stop-band drop off than a Hann window, as shown in Figure 3.1 (c) and (d). This window is created with equation (3.4)

$$w_{kaiser}(n) = \begin{cases} \dfrac{I_0\left(\pi\alpha\sqrt{1-\left(\dfrac{2nT_s}{T_sN-1}-1\right)^2}\right)}{I_0(\pi\alpha)} & 0 \le n \le N-1 \\ 0 & otherwise \end{cases} \tag{3.4}$$

where I_0 is the zero order modified *Bessel* function of the first kind, and α is an arbitrary shaping coefficient. This kernel in plotted in Figure 3.1 (a) for the comparison purpose.

A simplified representation of our filter-shift (FS) method for optimal STC is presented in Figure 3.4 using simulated fMRI data for illustrative purposes. Figure 3.4a shows the underlying BOLD signal (light blue) as well as the contaminated fMRI signal (dashed-line) with simplified physiological noise. For simplicity and illustration purposes we only add exaggerated physiological noise and ignore the other fMRI artifacts, contaminants, and noise. Multiple fMRI signals with different offsets are then sampled with the same frequency, simulating the effect of irregular sampling of adjacent slices in fMRI data. Figure 3.4(b) shows those sampled signals separately, highlighting the apparent difference between them. Figure 3.4(c) shows the signal upsampled by padding with zeros between samples, and Figure 3.4(d) shows the upsampled signal after lowpass filtering with a delay that is equivalent to their offset in original sampling. By lowpass filtering, we band limit our signal to the frequencies of interest, which provides a significant advantage over other STC techniques. Finally to obtain the recovered signal in the same sampling rate, we downsample the data to the scanner's sampling rate (TR=2 seconds, 0.5Hz) as shown in Figure 3.4(e).

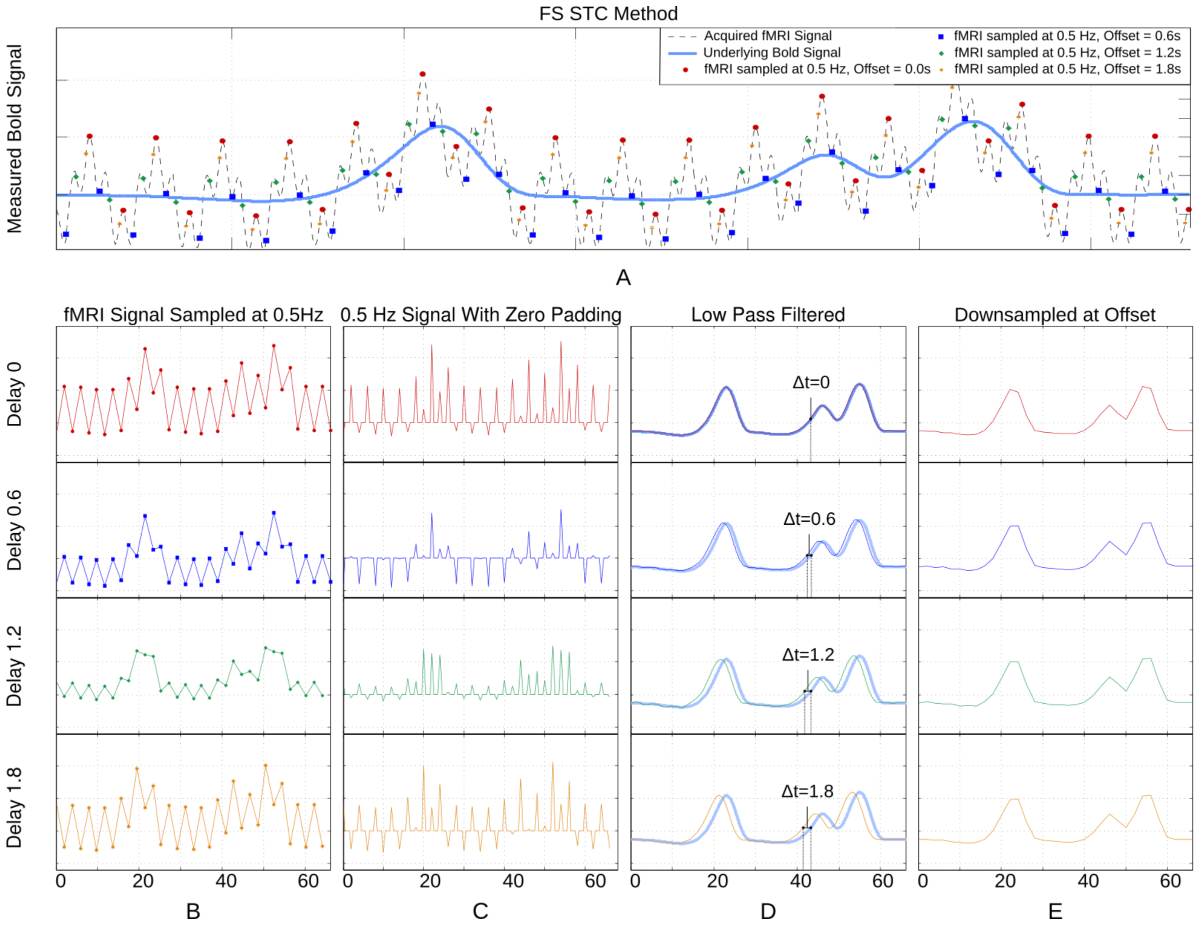

Figure 3.4: A visual description of the Filter Shift STC method.

A visual description of the Filter Shift STC method showing high frequency simulated data, the effect of down-sampling at various offsets, and how the original signal can be reconstructed with upsampling and low pass filtering regardless of offset. (A) An underlying bold signal (blue) is contaminated with physiological noise (black dashed) and sampled at 0.5Hz with different offsets (colored markers). (B) Each offset yields visually different low-frequency signals. (C & D) These signals are upsampled and LPF to remove noise. The result is a shifted version of the original bold signal. (E) By resampling the high frequency with the same offset results in identical low frequency signals.

Depending on the frequency the fMRI data is upsampled to, this process can significantly increase computation time. However, upsampling is achieved with zero padding and lowpass filtering, meaning that many of the values in the filtering step will be zero. This is shown in Figure 3.5. For a given BOLD time-series, shown in red, upsampling is achieved by zero-padding, shown as the blue circles between the original red samples. Determining the value of the BOLD signal at an arbitrary time, t_{off}, is the summation of the signal multiplied with the sinc function, centered at that offset. It is apparent that the majority of the sinc function's timepoints are simply multiplied with a zero-value sample. Only the timepoints where the sinc function overlaps the red samples will contribute to the summation. Thus, to resample the BOLD signal at a shifted offset, zero padding can be skipped all together by simply downsampling the high frequency sinc function at the desired offset, and convolving the two low frequency time-series. This greatly reduces the computations necessary, making the entire process fast and efficient.

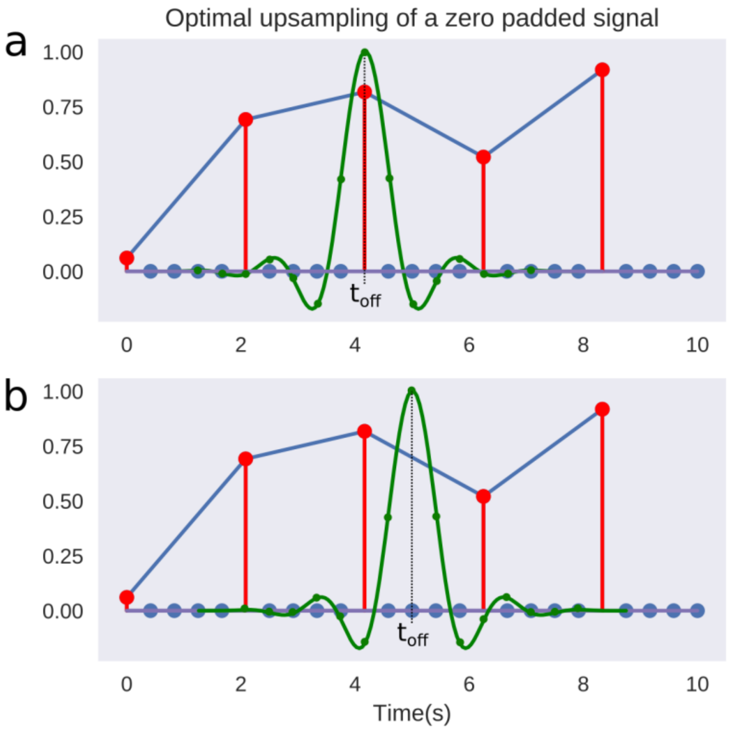

Figure 3.5: Optimization of the lowpass filter step in STC.

A sampled BOLD signal (red) is upsampled with zero padding (blue circles). Lowpass filtering this signal with a windowed sinc function (green) results in a high temporal resolution BOLD signal. The value of the high resolution signal at any given point t_{off} is given by the summation of the BOLD signal multiplied with the sinc function, centered at t_{off}. The majority of these points are multiplied with zeros. Only the timepoints of the sinc function that align with a red sample contribute to the actual value. Rather than convolving two high resolution signals where many of the computations are meaningless, and then downsampling at a given offset, the high frequency sinc function itself can be downsampled, with an offset equivalent to the desired time shift. The convolution of this downsampled sinc with the original BOLD signal produces results identical to the high-resolution method, but with significantly lower computational and memory requirements.

3.2.3 Simulated Data

Real fMRI data sets are problematic for evaluating the quality of one method over another because the true underlying BOLD signal is always unknown. Because of this, simulated datasets were used so that processed images could be compared to a known, true underlying BOLD signal. The generated simulated data in this chapter were used to: 1) evaluate the performance of our proposed FS method in comparison to existing STC methods with controlled levels of motion and noise, 2) examine the effect of different interleave acquisition sequences on STC, 3) examine the effect of short scan length on our proposed method, 4) to examine the effect of TR on STC, and 5) to examine the effect of spatial smoothing on STC.

The morphology of our simulated fMRI scans come from a real subject's data by temporally averaging all its volumes. Processing the same subject's structural image with FreeSurfer [44], [45] and using inter-modal rigid-body registration with FSL [46] gives us brain region masks in the fMRI space. Neuronal activity stimuli consisting of sequences of 20 boxcar pulses with jittered onsets (at least 10 s apart) and randomly generated durations (0.5 to 3.5 s) were created for each region. The neuronal stimulus for each voxel was convolved with the canonical double gamma HRF to generate the hemodynamic response. This signal was generated at a frequency high enough to simulate interleaved slice acquisition for a given TR and number of slices (upsampled to a frequency equal to N_S/TR, where N_S is the total number of slices. This allows one sample for each slice, and eliminates any need for further interpolation.). Null data (random noise) were assigned to voxels that were not assigned a hemodynamic response. To simulate cardiac and respiratory variations in the fMRI signal, a simplified approach was taken, using a single sinusoid at f_c=1.23 Hz for cardiac and another sinusoid at f_r=0.25 Hz for respiratory noise. The magnitude of the cardiac signal is modulated with the inverse of the distance of the voxel from the nearest artery. Thermal noise was then added to the signal. The temporally averaged volume is used to obtain the mean value at each voxel, which was used to shift the mean of the hemodynamic signal and to scale the standard deviation of the signal to 1% of the mean value comparable to a robust signal in the visual cortex. We used the same averaged volume for all simulated data sets to control for the significant difference in the morphology of the brain, which eliminates the need for spatial normalization to compare the results.

To have the most realistic simulation of motion’s interaction with interleaved slice acquisition, we simultaneously simulated the motion and slice sampling. Motion parameters were extracted from real subjects by taking the inverse of their spatial realignment transformation matrices at the original sampling rate (TR). We then upsampled these motion parameters (6 parameters) using spline interpolation to the same sampling frequency as the BOLD signals generated for each region. By applying the upsampled parameters to the volume at each sample point we can specify the exact position of the volume at any fractional time between the two TRs. This results in the most realistic simulation of the interaction between slice timing and motion. Different interleave types can be simulated by sampling the slices in the appropriate order.

Twenty simulated scans were used for the evaluation of our proposed FS method and the effect of noise and motion on STC. Each fMRI scan was simulated with twelve different combinations of noise and motion levels. Three different thermal noise levels were used, consisting of white noise that made up 0, 20, and 40% of the signal’s energy. For each noise level, four different motion profiles were simulated: high, medium, low, and no motion. The motion levels were classified by a set of real subjects’ mean frame-wise displacement (mFWD) inside the scanner (low: mFWD < 0.1mm, med: 0.25mm < mFWD < 0.4mm, high: 0.6mm < mFWD < 0.7mm) [19]. Generated fMRI scans consisted of 10 minutes of scanning with an in-plane acquisition matrix of 112×112, and 37 slices. The voxel size was set to 2×2×3 mm^3. Since our real data are acquired with a Philips scanner and with an interleave type in which every other $\sqrt{N_s}$ slices are acquired, we also simulated the same interleave type by skipping 6 slices between any two consecutive slice acquisitions. The default TR was equal to 2 seconds for these experiments. Thus, with 20 scans each simulated under 12 different conditions, we created 240 unique fMRI scans. In addition, 13 more fMRI scans were simulated and resampled at 6 different TR’s ranging from 0.5s to 5s for an additional 78 fMRI scans. In total, 338 fMRI scans were simulated for this study.

3.2.4 Real Data

The ideal task for testing the effectiveness of STC should have high temporal sensitivity and a robust BOLD signal across all subjects. Higher level cognitive tasks are not robust enough across subjects, and it would be difficult to say for certain whether any changes in the statistics are closer to the true underlying neuronal activity or not. Block design tasks are typically more robust, but lack the temporal sensitivity necessary and would be unsuitable for examining small temporal inaccuracies. Because the BOLD signal induced by visual stimuli generates robust activation in the primary visual cortex, an event related visual stimulus was used for evaluation of STC methods using real subjects' fMRI data. Thirty right-handed healthy subjects (17/18 young/old; percent female: 0.53/0.61, age mean ± std: 25.5/64.9 ± 2.4/2.2 years) were presented with visual (flashing checker boards) stimuli with random onset and duration (event-related design) while undergoing functional magnetic resonance imaging. To ensure attention to the stimuli, subjects were asked to respond with a button press at the conclusion of each visual stimulus. Functional images were acquired using a 3.0 Tesla Achieva Philips scanner with a field echo echo-planar imaging (FE-EPI) sequence [TE/TR = 20ms/2000ms; flip angle = 72 degrees; 112x112 matrix size; in-plane voxel size = 2.0 mm x 2.0 mm; slice thickness = 3.0 mm (no gap); 41 transverse slices per volume, 6:1 Philips interleaved, in ascending order. Participants were scanned for 5.5 minutes with at least 37 events of visual stimuli. Subjects were stratified based on their mFWD over the entire scan period. Ten low motion (mFWD < 0.14 mm), ten medium motion (0.14mm ≤ mFWD < 0.2mm), and ten high motion (mFWD ≥ 0.2mm) subjects were selected for each group.

3.2.5 fMRI Data Processing and Statistical Analysis

Both simulated and real data underwent various preprocessing pipelines consisting of the following modules: rigid body spatial realignment (motion correction or MC) was applied with FSL (*mcflirt* [47]), performing registration of all volumes to the middle one. STC (temporal realignment) was performed using our in-house method FS, as well as the FSL and SPM default techniques. All STC methods temporally aligned the data to the first slice, acquired at the beginning of the TR. We also created a "gold standard" method to compare STC techniques by constructing a slice-dependent shifted regressor for each slice. These shifted regressors account for the slice dependent acquisition offset delay. This method only applied a low pass filter to the data, as most STC techniques inherently have a small amount of low pass filtering. For a reliable comparison, the same filter parameters used in our FS method were used for the Shifted Regressor (SR) technique. In theory, this method should produce the best results, if no 3D processing algorithm (e.g. 3D smoothing, or 3D spatial transformation) has been applied in the pre-processing, as those methods combine data from different slices with different offset delays, which would alter the signals of each voxel.

In order to focus purely on the effect of different STC methods, only the specified preprocessing steps are applied to the data. We developed a standard generalized linear model (GLM) in Python and used it to model observed fMRI data $\boldsymbol{Y}$ at each voxel as a linear combination of regressors $\boldsymbol{X}$ which were created by convolving the double gamma HRF with the stimulus timing function. We used a standard GLM model shown below:

$$\boldsymbol{Y} = \boldsymbol{X} \cdot \beta + \boldsymbol{e} \tag{3.5}$$

where β coefficients were obtained using the least-square estimate and given by:

$$\beta = (\boldsymbol{X}^{\boldsymbol{T}}\boldsymbol{X})^{-\boldsymbol{1}}\boldsymbol{X}^{\boldsymbol{T}}\,\boldsymbol{Y} \tag{3.6}$$

To obtain the significance level of the voxel's activation associated with the stimuli of interest, standard GLM statistical inference was performed to obtain the t-statistics for each voxel independently [48]. We used voxel-wise t-statistics as the evaluation criteria for our method comparisons, as well as investigating the effect of different acquisition settings and artifacts on the effectiveness of STC. All statistics used in the results are from this native-space, subject-level analysis.

3.2.6 Voxel Selection

Assessing the effectiveness of STC methods is extremely challenging due to its interaction with motion [49], and the fact that its improvement is slice-dependent. The benefit of STC could appear absent if the majority of activation falls on a slice with low temporal delay due to the fact that very little temporal shifting is encountered in these slices. This is analogous to examining the effect of motion correction on data with extremely low motion. In most typical STC techniques, one slice is chosen as the "reference slice", and all other slices are shifted temporally to match the time at which the reference slice was acquired. The effect we see due to STC is directly proportional to the size of this temporal shift. In fact, if the activation falls on the reference slice, then no shifting occurs, and we will see absolutely no difference between STC and uncorrected data. This could be mistaken as evidence that STC may not be required in the preprocessing pipeline.

We demonstrated this challenge by showing how the improvement due to STC is dependent on the acquisition offset delay in a typical real subject's fMRI data. We selected two adjacent brain slices with maximum difference between offset delays. While both slices present the same level of activation, the low delay slice is shifted only slightly with STC, and so it sees minimal change. On the other hand, the high delay slice is shifted significantly, and so it experiences a more profound and measureable change. This is visible in the resulting analysis when comparing t-statistics from a pipeline with STC to a pipeline without STC. Figure 3.6 shows the difference in t-statistics before and after STC on two adjacent slices with maximum offset delay difference (slices 18 and 19 with 1.8 and 0.15 seconds offset delay respectively) in real data after being smoothed with a 5mm 2D Gaussian kernel. Areas of significant activation are outlined in green. Warm colored areas indicate an improvement in t-statistics compared to uncorrected data. This illustrates the challenges involved in evaluating STC methods using real fMRI data. Figure 3.6(a) shows that the t-statistics in slice 19 have very little benefit from performing STC, as the difference between the

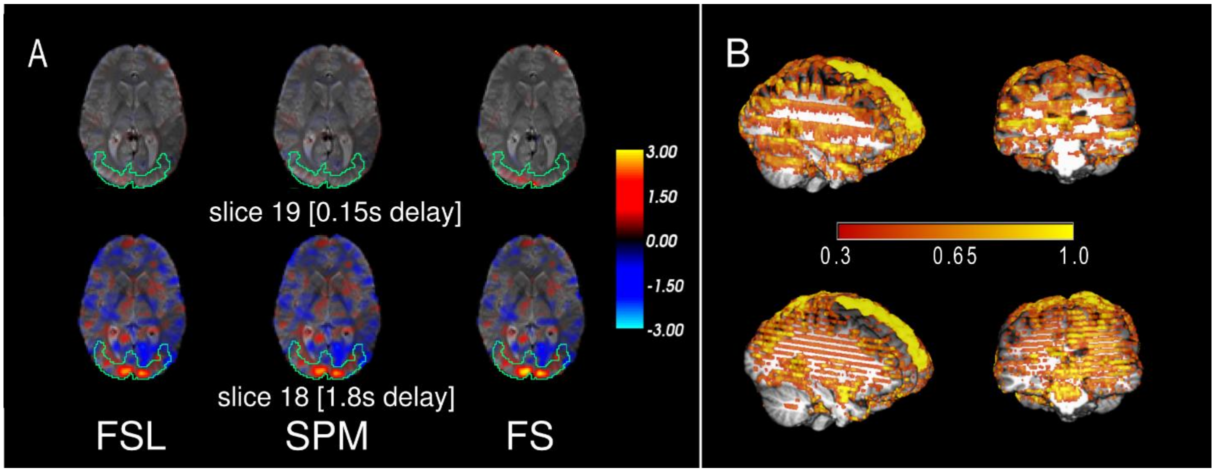

Figure 3.6: Difference in t-statistics between STC and uncorrected data on two adjacent slices with different acquisition delays in real data.

The benefit of STC varies from slice to slice, depending on the acquisition delay. Significantly activated areas are outlined with a green line for both slices. A) Difference in t-statistics for uncorrected vs. STC data in two adjacent slices. Slice 18 (1.8s delay) has t-statistics significantly larger than those in uncorrected data with differences as large as 3. Slice 19 (0.15s delay) has very few differences from uncorrected data. Note that because this is a difference map, this simply indicates that all methods, including uncorrected, perform similarly well on low-delay slices. B) A 3D visualization of the difference between t-statistics in the FS STC data and uncorrected data. The stripes along the z axis are present at high acquisition delay slices in data collected with Phillips interleave 6 (top), and even-odd.

uncorrected statistics is small. However, their adjacent voxels in slice 18, even though they have the same level of activation (delineated by green lines in Figure 3.6(a)), have significant improvement over uncorrected data.

There's also noticeable blue regions throughout the brain, indicating a decrease in t-statistics. This compared to uncorrected data does not indicate poorer performance on the part of the STC data. A decrease in t-statistics can be an improvement in the following ways: 1) An uncorrected time-series from a voxel unrelated to the task is erroneously correlating with a regressor (Type I error), and this correlation is removed or reduced after the time-series is shifted during STC, or 2) An uncorrected time-series from a voxel that is negatively correlated to the task is erroneously calculated to be uncorrelated (Type II error), and the correlation can be seen after the time-series is shifted during STC. An example of this would be with the default mode network, which has significant deactivations during task performance. STC is going to improve the t-statistics of the deactivation by making them more negative, which shows up as a reduction in t-statistics.

This clearly demonstrates the slice dependency of STC performance. Figure 3.6(b) visualizes the same concept in a 3D view of the brain with both Philips (top), as well as even-odd (bottom) interleave, where the color overlay represents the t-statistics difference between STC data and uncorrected data. Note that in regions of activation, this difference is significantly higher than the color bar's maximum. In order to show whole-brain differences and capture the spatial pattern induced by interleaved acquisition, the threshold has been set artificially low. It is clear from this figure that slices acquired in the beginning of the TR benefit significantly less from STC compared to slices acquired later in the TR. The same phenomenon has been shown for sequentially acquired data in previous studies. This paper is primarily concerned with the effects of STC on fMRI data in different preprocessing pipelines. In order to evaluate this, we must examine voxels that are affected by the STC process. The evaluation of the STC methods and their interaction with other processing steps would be meaningless if it is done on slices with minimal or no time delay, just as evaluating motion correction technique on scans without motion would give invalid results. Because of this, we focused only on high delay slices to examine the effect of STC and its interaction with preprocessing steps where it's most detectable, rather than comparing the effect of STC across all slices.

For real data, we selected slice 17, (1.46s delay from the beginning of the TR), and for simulated data we selected slice 18 (1.8s delay from the beginning of the TR). We selected the left superior frontal (LSF) region as our region of interest (ROI) for simulated data since the superior frontal region is one of the few regions that spans over 20 slices, thus including slices with various acquisition delays. Therefore, we can guarantee that some part of the region will fall in a high-delay slice regardless of motion and subject morphology. It also spans from the center of the brain to the frontal region, which will capture many different kinds of motion artifacts, as the same motion may produce different, even opposite signal changes in different locations in the brain [19]. Only voxels in the LSF ROI were used in all simulated data analysis, and the known underlying BOLD signal assigned to the LSF ROI was used as our regressor.

For real data, we created an ROI for each subject that included voxels where we expected significant visual activation. This ROI was created by transferring a group level activation mask for the visual stimulus back into each subject's native space. This group level activation mask was created by running a full default FSL first level analysis, which consists of the following steps: a) spatial realignment, b) STC, c) 3D smoothing with FWHM=5mm, d) intensity normalization e) temporal filtering (125s cutoff) f) GLM with prewhitening, and a second level analysis including: a) spatial normalization, b) full Bayesian linear model [50], [51], and c) cluster-wise multiple comparison correction (z threshold 2.3, cluster significance threshold $p = 0.05$). Only voxels in the activated regions were used in our real data analysis. Region masks for real and simulated data can be seen in Figure 3.7. The large ROI from the group level is only used to confine voxel selection to an area that is neurophysiologically task-relevant, to avoid false positives. For instance, we want to prevent selecting a false-positive voxel in the motor cortex for visual stimulation. One could just replace these ROIs with an anatomical mask of the visual cortex without having a significant alteration on the results. For real data, the average size of this region across all subject's native space was 8704.3 voxels (104.6 cm^3), with a standard deviation of 974.6 voxels. When confined to a slice of high delay, the average size of this mask was 514.0 voxels (6.2 cm^3), with a standard deviation of 83.4 voxels. Despite the fact that this ROI was identified using a pipeline that performs MC before STC, the spatial smoothing used in the group level analysis makes the resulting mask large enough so that it will not bias the results to favor MC before STC pipelines. The large ROI is necessary, as individual differences in head position and brain function do not guarantee that all subjects will have significant activity in a single anatomical region if it's too small. While it's possible that this ROI may cover different anatomical regions over different subjects, the purpose of the group level analysis was to identify regions functionally and neurophysiologically associated with the task. This allows us to identify the regions that are most likely to have the same underlying BOLD signal. This region spans over multiple slices, giving us a good chance at identifying significant voxels within the functional region, on a slice of high temporal delay.

Only voxels in this ROI that intersected the chosen slices with high temporal acquisition delay were used. We used the SR technique to obtain the significantly activated voxels within the ROI without applying any spatial smoothing. In addition, the SR method does not require an extra STC step, thus making the choice of STC before or after re-alignment irrelevant. For any given subject, 20 voxels that had the highest t-statistics from the SR pipeline were identified. The t-statistics of these 20 voxels were used to compare all STC methods and scan parameters for that subject. We then use a one tail repeated measures t-test on these values to compare the effectiveness of each pipeline. While we are using 30 fMRI scans from real and 20 from simulated data, each scan provided us with 20 voxels, each of which provides a unique fMRI measurement from different locations in the brain. In other words, at each voxel location, we can establish

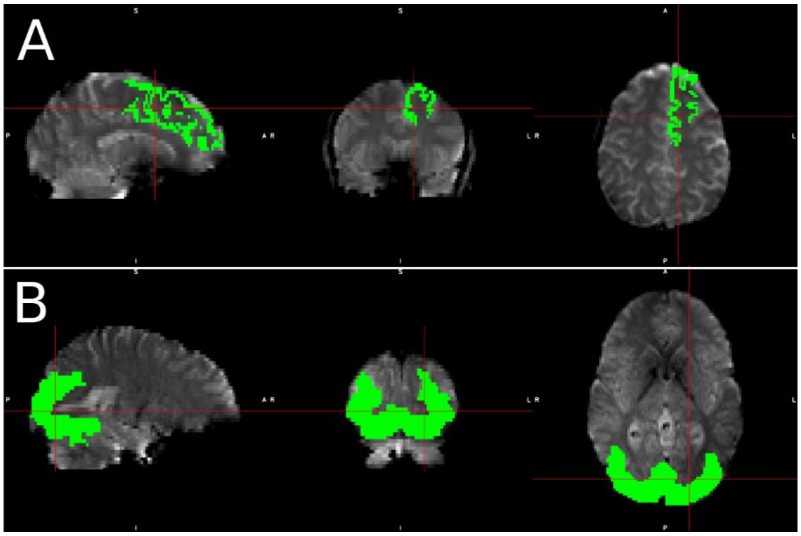

Figure 3.7: Spatial maps for ROI's used in real and simulated data.

A) Simulated data ROI map, which was identical for each simulated subject. This ROI was the anatomical region defined by Freesurfer as the left superior frontal region. B) Real data ROI map, which was generated from the significant activation in a standard group level analysis and transformed back into each subject's native space. The ROI varied slightly from subject to subject due to individual subject morphometry.

an independent but similar comparison between the STC methods. Because of this, we consider each voxel a degree of freedom (DoF), giving us 199 DoF for real data (10 subjects for each motion level), and 399 for simulated data. The SR method theoretically does the best job identifying the regions that truly match the expected signal. By using the voxels with the highest statistics from this method, we identify the 20 voxels that are most likely to be true positives, thus minimizing the possibility of type I error confounding our analysis, and allowing us to focus mostly on the effects of interpolation error from STC. It is important to note that these are not necessarily the 20 highest voxels for the other STC methods. Furthermore, from subject to subject, the location of these voxels is not constrained, as not every subject will exhibit the strongest response in the same location. Within each subject, we are comparing the same group of voxels across all different STC methods, so it is appropriate to use a repeated measures t-test to see if the preprocessing pipeline had any significant effect on the GLM, as done previously in the literature [39]. Our processing pipeline is illustrated in Figure 3.8.

The low number of voxels used in the comparison was chosen because certain real subjects only had 20 significant voxels present in both the region of interest and the high-delay slice. The reason this number is low is because we do not perform spatial smoothing, which greatly increases the number of significant voxels, at the cost of a lower maximum t-statistic. In order to perform a repeated measures t-test, we need to compare values from the same voxels across multiple datasets. To ensure that the voxels we were comparing were in fact statistically significant in every comparison, we use the highest 20 voxels.

3.2.7 Comparison of FS With the Existing STC Methods

The goal of this experiment is first to show the necessity of performing STC on fMRI data, and then to demonstrate the superiority of our proposed optimal STC technique (FS) in comparison to the existing ones, using simulated and real data. In addition, we investigated the effect of fMRI artifacts (involuntary head motion and noise) on the effectiveness of performing STC on fMRI data. For simulated data, three different levels of noise and four different levels of motion were simulated to contaminate the fMRI data, as explained in section 3.2.3, whereas in real data we stratified subjects based their head motion profile to three different levels as explained in section 3.2.4

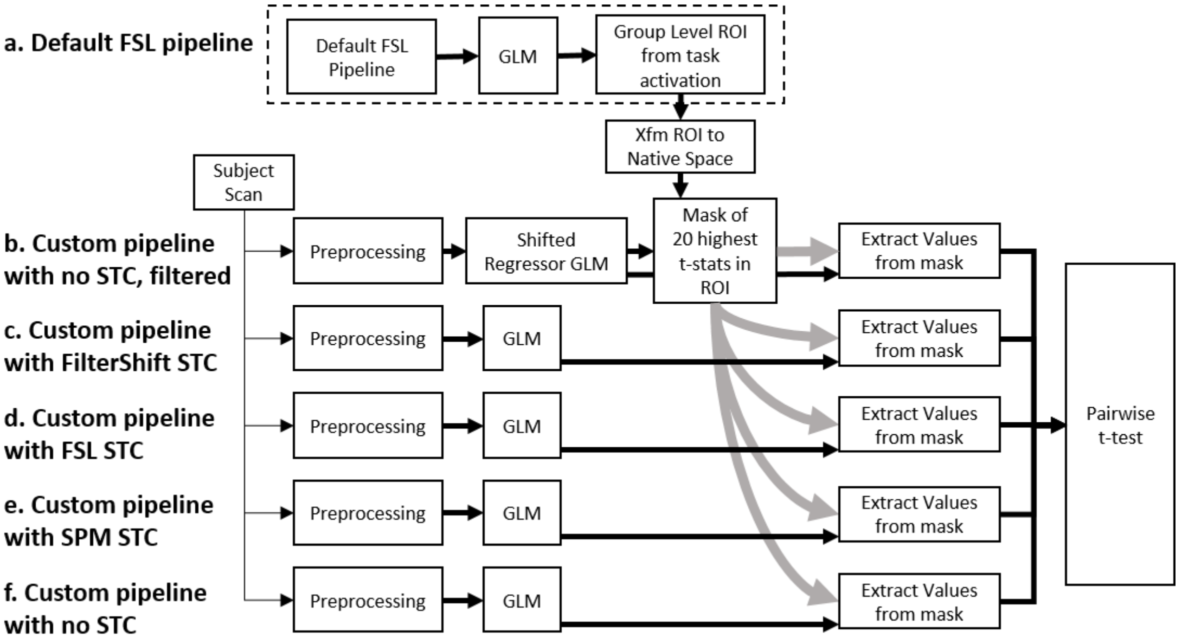

Figure 3.8: A flowchart of the processing pipeline for real data.

a) A default group level GLM is run on all subjects to obtain a region of activation, which is binarized into a mask and transformed back into each subject's native space. This mask is used as an ROI to examine t-statistics from 5 different processing pipelines: b) No STC is applied, but the data is temporally lowpass filtered, and slice-dependent regressors shifted to account for the acquisition offset are used. c) Our in house FS STC method is used. d) FSL STC is used. e) SPM STC is used. f) No STC is used, and regressors are not shifted to account for slice offset. The statistics from pipeline b are used to identify 20 voxels with the highest t-statistics in the ROI. The standardized beta from these 20 voxels are then extracted from the other pipelines, and the values are compared in a pairwise t-test.

For each combination of motion and noise level in simulated data we obtained the statistical parametric maps associated with one regressor. For simulated data, the regressor contained the underlying neuronal stimuli for the LSF ROI, while for real data the regressor contained the visual stimuli timecourse. Higher t-statistics indicates the superiority of a method as compared to the others since it could recover the original underlying BOLD signal with more accuracy.

The interaction between the effectiveness of STC and the level of motion/noise can also be examined using the voxel-wise t-statistics. We anticipate that increasing motion will reduce the benefit of STC, since motion has much higher destructive effect than the slice timing offset delay. If increasing the motion/noise level would result in smaller t-statistics, then we can conclude that there is a significant interaction between the STC gain and level of motion/noise.

3.2.8 STC and Short fMRI Datasets

Because FS employs a higher order filter than other STC methods, there is an inherent initialization period that cannot be ignored. Our method is employed with substantial padding to avoid any such problems; however, scans with fewer time points may be more susceptible to initialization artifacts. If the data is not padded sufficiently, or is padded incorrectly, this initialization period may introduce artifacts into the data, reducing its accuracy. We examine the validity of our method as compared to FSL and SPM STC techniques, as they have a much smaller initialization period. Our goal then is to show that the statistics from our method remain in agreement with FSL and SPM, two of the most widely used software packages available, for all practical scan lengths.

As the number of samples in a scan decreases, the statistical power of the measurement also decreases. By reducing the number of time points in a scan, we expect to see the statistics gradually decrease. Because our method employs an FIR lowpass filter with a moderate initialization period, we would also expect that once the time-series is short enough that the half-length odd padding becomes shorter than the filter order, our method will begin to perform significantly poorer than the others. This was experimentally tested on a subset of 5 simulated subjects (no motion, no noise) as well as 5 real (low motion) subjects. Both the real and simulated data were truncated step-wise with decremental steps of 10 volumes, down to a length of 20 volumes. After each truncation, STC and a GLM regression were run, and the statistics were saved for further analysis. As described in section 3.2.6, the voxels with the top 20 t-statistics were extracted from SR method within the real/simulated ROIs in the full-length data case, and the same voxel's t-statistics were used from each truncated data set.

3.2.9 STC on fMRI Data With Short TR

It has been suggested that for short (<2s) TRs, the benefit of STC is not worth the possible errors introduced by the process [52]. It is generally considered that with such short TR, STC is an unnecessary step with little value. This is based on the assumption that the BOLD signal is generally quite slow, and so any signal change due to temporal offsets is likely to also be small. However, the GLM is extremely sensitive to small shifts in signals, and to our knowledge no study has quantitatively demonstrated that STC is futile for short TR acquisitions. With the development of multiband EPI and improvements in the pulse sequence, whole brain volumes can be acquired in just fractions of a second [13]. With the growing popularity of short-TR data, it is important to examine the benefits of STC on various TRs. To do this, we simulated 13 additional subjects with low motion and low noise, in the same manner as described in section 3.2.4 (10 minute scan with random event related stimuli). Each subject's high-resolution BOLD signal was resampled at 2, 1, 0.5, 0.33, 0.25, and 0.2 Hz, to simulate TRs of 0.5, 1, 2, 3, 4, and 5 seconds. This resulted in 6 data sets per subject. The full 10 minutes were sampled at each TR value so that the length of the simulated scan varied as a function of TR. We then performed all 4 STC methods on each subject's data. Each TR was separately evaluated by identifying the top 20 voxels from the SR method as described in section 3.2.6. The values of these voxels were then extracted across all other STC methods in the TR. This was repeated for all TRs, and the average t-statistics of each STC method were plotted as a function of sampling rate.

3.2.10 STC and Spatial Smoothing

STC is particularly sensitive to any sort of image processing/analysis that spans over multiple slices, the most common of such processes is 3D spatial smoothing. Smoothing is generally done to enhance the robustness of the statistical analysis results and reduce false positive rates [40]. Our goal in this experiment is to investigate the effect of 3D smoothing on the effectiveness of STC. Four different Gaussian non-linear smoothing kernels with FWHM = 3.5, 5, 6.5, and 8 mm were used to smooth simulated and real data using FSL's smoothing method. Smoothing was applied by spatially convolving each 3D volume in the time-series with the appropriate 3D Gaussian kernel. For real data, the effect of smoothing was examined on high, medium, and low motion scans. For simulated data, low motion scans were used, and the effect of smoothing was examined for interleave 1, interleave 2, and interleave 6 acquisition methods. Each fMRI scan was first motion corrected and slice timing corrected before the various smoothing kernels were applied. We compared the relative performance of each STC method to all others within each level of smoothing, where higher t-statistics are considered better performance. For each motion/interleave case for real/simulated data respectively, the corresponding "unsmoothed/SR" image was used as the reference image for voxel selection.

3.3 Results

3.3.1 Performance of FilterShift Compared to Other STC Methods

Figure 3.9 shows the t-statistics from the parametric maps obtained from uncorrected and STC simulated data (interleave 6). The fact that for all conditions the mean t-statistic for STC data is always greater than the mean t-statistic for uncorrected data indicates that it is always beneficial to perform STC. Specifically, Figure 3.9 shows that FS STC outperforms all other methods, except for in high motion/high noise conditions. In the no motion, no noise case, which has the most optimal conditions for signal reconstruction, FS t-statistics were 415% higher than uncorrected data, while FSL and SPM were 51% and 47% higher respectively. FS yields significantly higher t-statistics than all other STC methods ($p<0.001$) for all levels of motion and noise, except for high motion with 20% and 40% noise levels. At high motion and no noise, FS still significantly outperforms FSL and SPM, where FS t-statistics were 51% higher than uncorrected data, and FSL and SPM were 32% and 33% higher respectively. Adding noise to this condition reduced all the t-statistics to a point where the differences were insignificant ($p>0.05$). Still, the high motion and high noise case shows that the application of any STC is still beneficial, and each method improved the t-statistics by on average 33%.

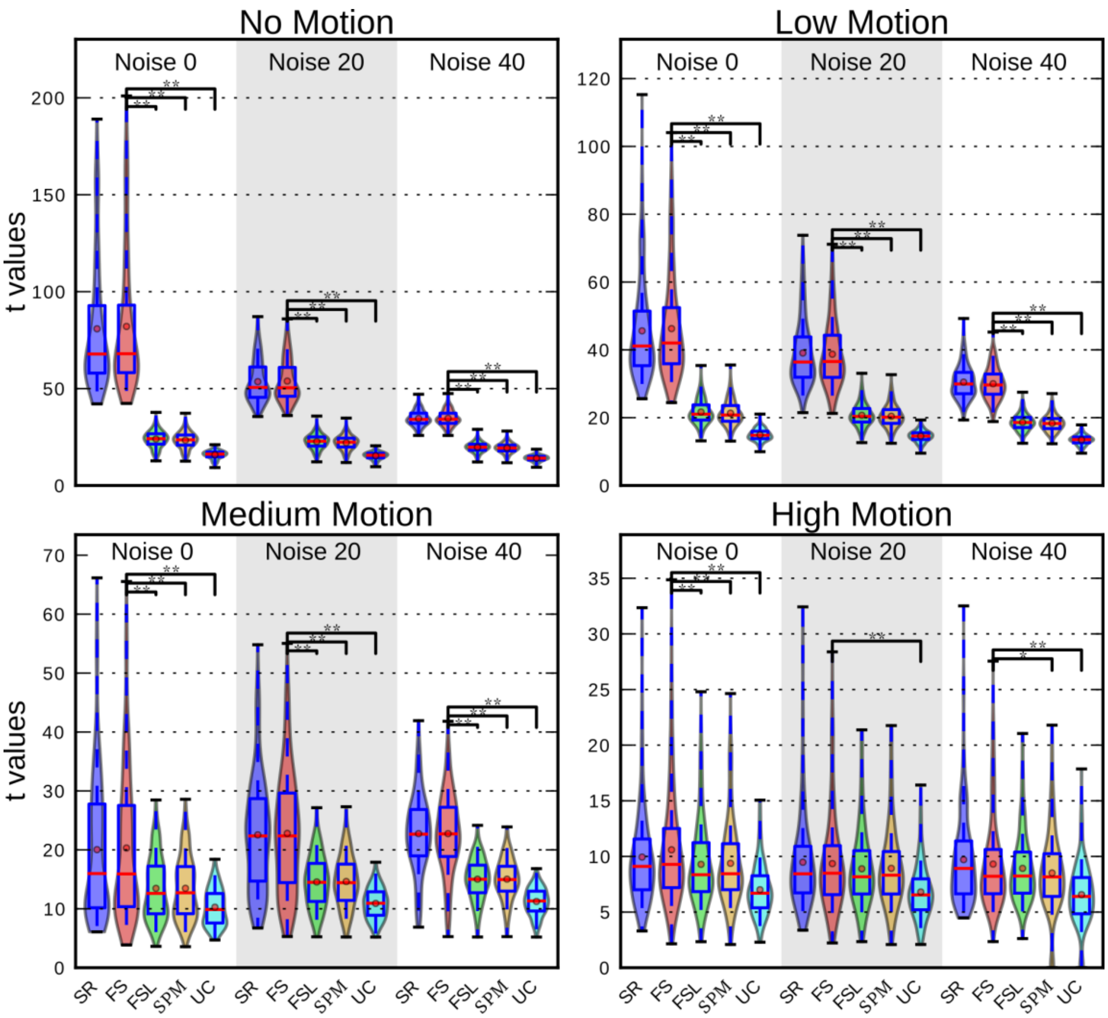

Figure 3.9: Voxel-wise t-statistic comparison of STC methods on simulated data.

STC data and uncorrected data from the LSF ROI in simulated data for various noise and motion levels with interleave 6**.** STC was carried out with three methods: FSL, SPM, and FS. The analysis was carried out for high, medium, and low motion cases, as well as three different SNR conditions (Noise 20 indicates that 20% of the signal's energy is from white noise, and so on). Each violin plot contains values from 20 scans. Higher values indicate that a STC method had higher z scores than data that was analyzed with no STC. Two stars indicate that these z differences are also significantly different from our method (FS), t<0.001, one star indicates significance p<0.05.

The twofold interaction of noise and motion on STC gain is also shown in Figure 3.9. The effect of adding noise to data is that the average t-statistics decrease linearly, but at different rates. This results in lower variance between methods, meaning all methods become more similar in performance. In reference to the no noise no motion case, mean FS t-statistics decrease 34% and 54% with the addition of 20% and

40% noise respectively (noise 20 and noise 40 in Figure 3.9). FSL and SPM both decrease 6% for the noise 20 case and 17% for the noise 40 case. Finally, uncorrected data reduces just 3% and 12% respectively.

Motion has a similar effect, in that it decreases the average t-statistics and reduces the variance; however, its overall effect is larger than the effect of noise. From the no noise no motion case, the addition of low, medium, and high motion reduces FS t-statistics by 44%, 75%, and 87% respectively. FSL's t-statistics were reduced by 11%, 44%, and 61%, while SPM's t-statistics were reduced by 9%, 43%, and 58%. Finally, uncorrected data was reduced by 6%, 36%, and 55%. The variance of the mean t-statistics for each method also decreased much faster with the addition of motion. It's clear from these results that the presence of noise and motion both reduce the effectiveness of all STC techniques, however FS remains significantly better for most cases, and never performs worse than FSL or SPM, even in the high noise/high motion case. It should be emphasized that by using simulated data, these results were obtained while controlling for differences in baseline fMRI activity and brain morphology, both of which have a stronger deteriorating effect on the results than the offset delay in slice acquisition.

Figure 3.10 shows the t-statistics from the top 20 voxels in slice 17 from the SR (gold standard) case, extracted for all methods from real data. As with the simulated data, Figure 3.10 shows that STC is always beneficial in processing real fMRI data, regardless of the technique, even though the degree of its improvement significantly decreases with any increase in the level of motion. With low motion, t-statistics from FS were 33% greater than uncorrected, while FSL and SPM were 31% and 28% greater, respectively. This illustrates the superiority of the proposed FS method as compared to the FSL and SPM methods, since the voxel-wise paired t test shows a significant increase in the t-statistics of the resulted parametric maps with FS ($p<0.001$). Higher levels of motion decrease these values and the differences between them, and in the medium level of motion the t-statistics from FS are only significantly higher than SPM and uncorrected data. Finally, in high motion subjects FS shows no significant improvement to the other STC techniques ($p>0.05$) whereas it still significantly improves the t-statistics in comparison to uncorrected data ($p<0.001$). The t-statistics from subjects with medium motion were on average 4% lower in FS, and 1% lower in FSL and SPM, as compared to the low motion subjects. High motion subjects had t-statistics 19% lower for FS, 14% lower for FSL, and 15% lower for SPM.

Figure 3.10 also presents the results of the gold standard (SR) STC method. In all levels of motion, FS performed closest to the SR method, indicating that it is more optimal than FSL and SPM. In real data, the contamination from thermal noise, motion, and physiological noise is much more complex than in the simulated data. It is also apparent from this that the effects of motion are not as obvious as in the simulated data due to the additional sources of contamination in real data.

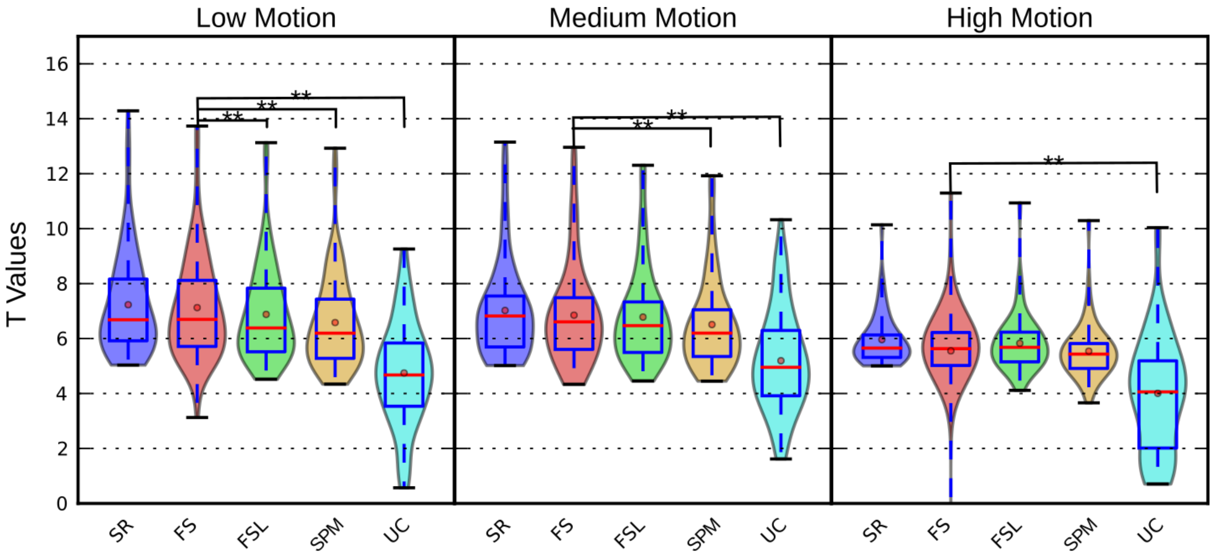

Figure 3.10: Voxel-wise t-statistic comparison of STC methods on real data.

STC data and uncorrected data in the visual ROI in real data for various motion levels with interleave 6**.** The top 20 voxels from the Shifted-Regressor method were identified from the slice with high delay (Slice 17) that intersected the region of significant activation. The values from these voxels were then extracted from all other STC methods for comparison. Methods that are significantly different than the proposed method ($p < 0.001$) are indicated with a star, pair-wise t-test.

3.3.2 Effect of Scan length on STC

Figure 3.11 shows the top 20 voxel's mean t-statistics from five low-motion subjects plotted against the length of a truncated scan for both real and simulated data. As expected, our method performs better than both FSL and SPM for the majority of the scan lengths. In the simulated data, the fluctuations in the statistics from FSL and SPM appear to be exaggerated. This is likely due to the sensitive nature of the GLM on a very clean signal. Similar fluctuations are present in the FS data, however the amplitude is much lower. In the real data, we see a much better example of how all the statistical methods have similar slope at each point. This verifies the consistency and reliability of each method against the others. In both the simulated and real data, there is a critical scan length where the FS method no longer outperforms FSL and SPM. In real data, this value is at approximately 30 time points, which is comparable to the calculated length of the filter's initialization period, 23 scans. For the simulated data, FS performs worse than FSL at 38 time points, and performs worse than SPM at 33. For all lengths greater than this, the statistics agree with our previous analyses, so we can assume that this divergence is due to the larger initialization period for the low pass filter in the FS method.

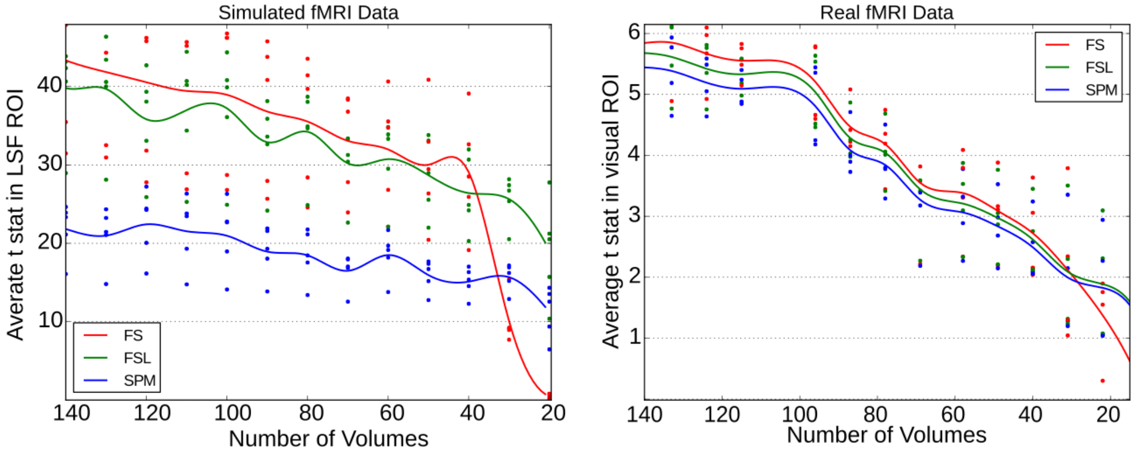

Figure 3.11: Performance of STC methods vs scan length.

(Left) Simulated data: top 20 t-statistics vs length of scan by method for five subjects, extracted from the slice with maximum delay (slice 17) in the region with significant activation. Divergence between our STC method and controls occurs at ~ 38 volumes. (Right) Real data: top 20 t-statistics vs length of scan by method for five subjects. Divergence occurs at ~ 27 volumes

3.3.3 Effect of TR on STC

Figure 3.12 shows the mean t-statistics of each method from the experiment described in section 3.2.9 plotted as a function of TR. As the TR increases, the average t-statistic of the selected voxels decreases in all slice timing methods, including the SR and FS methods. T-statistics in uncorrected data also decrease significantly as the TR increases, due to an increasing temporal misalignment between the model-predicted signal and the observed fMRI signal, as well as the general effect of a lowering number of sample points. In addition, we see the difference between STC data and uncorrected data increase with TR, as an indication that STC is more and more critical at high TRs. However, at low TR's, the difference between FSL, SPM, and uncorrected data becomes insignificant. We do not see such behavior for SR and FS data, which actually continue to improve exponentially as the TR shortens. This is in agreement with the sentiments from the literature that there is minimal benefit of STC for TRs less than 2s, as these studies would have used FSL or SPM STC methods. At a TR of 2, FSL and SPM are performing 15.6% better than uncorrected data, while SR and FS perform 85.6% better. These values gradually increase, to where TR=5, FSL and SPM perform 55.7% better than uncorrected, while SR and FS perform 101.1% better. For the lower TRs of 1.0 and 0.5 seconds, FSL and SPM converge to the uncorrected data, to where the difference becomes insignificant (a 5% and 2.2% difference respectively). However, SR and FS continue to outperform uncorrected data by 83.2% for a TR of 1s, and 88.0% for a TR of 0.5s. This is mainly due to the aliasing of the physiological signals in fMRI data into the frequency spectrum of the BOLD signal. By increasing the sampling rate, the aliased artifacts from physiological noise move outside the BOLD signal spectrum, and can be removed by filtering with same cutoff frequency (0.21 Hz).

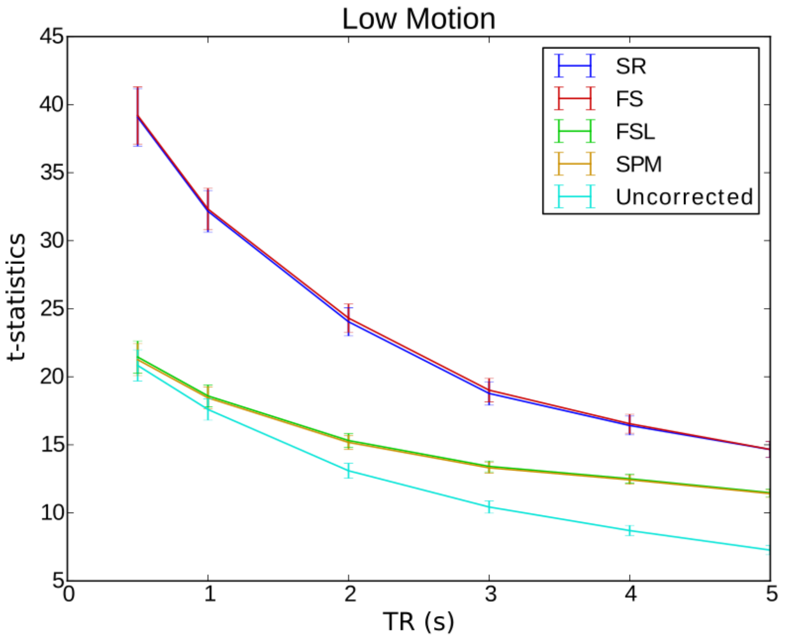

Figure 3.12: Effect of TR on STC in simulated data.

T-statistics from LSF region in simulated data with TRs varying from 0.5 to 5 seconds extracted from a slice with maximal delay (slice 18). Error bars represent the 95% confidence interval, calculated from the extracted t-statistics for each method across all 13 subjects.

3.3.4 Effect of Spatial Smoothing on STC

We compared the effect of spatial smoothing on STC using both real and simulated data. Figure 3.13 shows the results across simulated subjects with low motion for various types of interleave acquisition. For simulated data, increasing the kernel size reduces the mean t-statistics monotonically as kernel size increases for all STC data under all interleave scenarios. Significant differences in statistics are marked with a star for $p<0.01$, and a double star for $p<0.001$. For interleave 6, FS's mean t-statistics dropped 62% from the unsmoothed case when smoothed with the 8mm kernel, while FSL and SPM decreased 46%. Interestingly, mean t-statistics from uncorrected data only decreased monotonically for sequential (interleave 1) and even odd (interleave 2) acquisition. For interleave 6, the mean t value is 26% higher than the unsmoothed case at FWHB of 3.5 mm, and 8% higher than the unsmoothed case at FWHM of 5mm. Beyond 5mm, the smoothed uncorrected data no longer performs better than the unsmoothed data, dropping 9% below the unsmoothed case for 6.5mm, and 22% below for 8mm.

In sequential data (Interleave 1) the SR method performs significantly better than the proposed FS method in most smoothing cases. As the slice acquisition order increases, SR performs worse as compared to FS for any given kernel. For interleave 1, SR and FS are comparable until a smoothing kernel of 6.5mm. For 6.5 and 8mm, SR outperforms all other STC methods ($p < 0.001$). This improvement is maximum at the 8mm smoothing kernel, where the average t-statistics for SR are 0.1% higher than FS. For interleave 2, SR no longer outperforms FS in any of the smoothed datasets, and in fact is significantly worse ($p < 0.001$), with the largest difference occurring at the 3.5mm smoothing kernel, resulting in t-statistics 3.9% lower than FS. Finally, for interleave 6 the smoothing continues to lower the quality of the SR method, again making it perform significantly worse than FS in all smoothed datasets ($p < 0.001$). This difference is largest at the 5mm and 6.5mm kernels, resulting in t-statistics 8.0% lower than FS. In all these cases, SR still outperformed all other STC methods, including uncorrected data ($p < 0.001$).

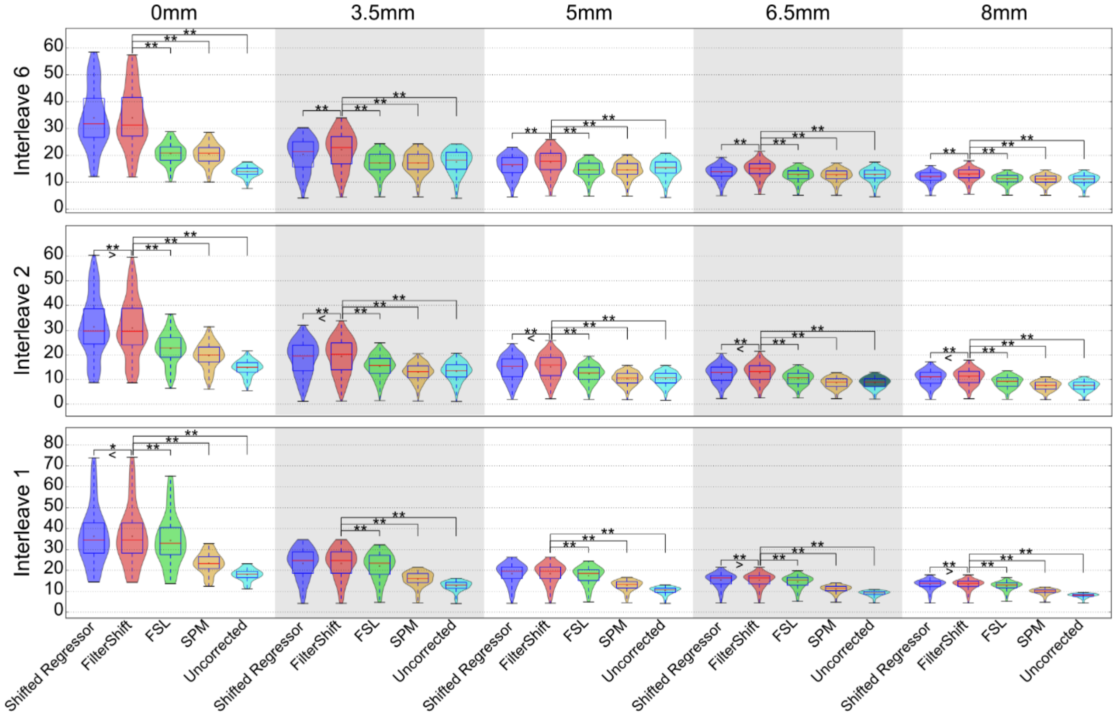

Figure 3.13: The effect of spatial smoothing on simulated data with STC.

Violin plots show the resulting top 20 t-statistics for 20 simulated data sets processed with smoothing kernels of 0, 3.5, 5, 6.5, and 8mm (columns). We examined the effect of smoothing for sequential (interleave 1), even-odd (interleave 2) and every 6th (interleave 6) acquisition (rows). For each interleave/smoothing condition, statistics were compared across 5 STC conditions: Shifted Regressor, FS, FSL, and SPM STC methods were examined, as well as uncorrected data. For each interleave, the voxels with the top 20 t-statistics were identified from the unsmoothed Shifted Regressor case. The values of these 20 voxels are plotted for all other STC methods and all other smoothing conditions. The effect of smoothing is seen as a lowering of the mean t-statistics, as well as reducing the variance across STC methods due to the distribution of slice-dependent errors. For interleaved data, the Shifted Regressor method, which is supposed to be a gold standard, performs worse than our proposed FS method due to these distributed errors. '<' and '>' Symbols indicate which mean is greater for cases that are not easily distinguishable.

3.4 Discussion

Reconstructing a true underlying signal from a sampled version by upsampling and lowpass filtering has been a common practice in digital signal processing field for quite some time. However, such a simple and optimal technique had not been fully utilized in fMRI data processing until we introduced our optimal STC method. We have demonstrated the benefit of STC on fMRI data in both real and simulated data which had already been shown in the literature [39]–[41], [53]. However, the slice-timing problem is fundamentally intertwined with many confounding factors such as involuntary head motion during scanning. Because of all the interactions between these factors, it's often difficult to intuitively say if slice-timing correction would provide any benefit to the analysis. We examined the effect of motion on the effectiveness of STC, and showed that even though the effectiveness of STC deteriorates with increasing levels of movement, it still remains beneficial to be executed as a preprocessing step. In addition, we showed that our proposed method (FS) outperformed both FSL and SPM's STC in every case, aside from the highest level of motion.

Simulated data showed the absolute superiority of our proposed FS method in optimal and even noise/motion-contaminated conditions. In real data, FS still outperformed the existing method, however the gain was much smaller than in simulated data with the same level of motion contamination. This suggests that there are remaining harmful sources of error that we have not taken into account in our simulation. The differences in brain morphology or the disturbance in the homogeneity of the magnetic field due to other factors may be some of these sources. Despite this, our method generated results better than or comparable to the existing STC methods for all level of motions in real data. Studies may acquire subjects with higher levels of motion than those here, but we can gather from the simulated data that it's unlikely FS will ever perform worse than FSL or SPM. In fact, the highest noise/motion level present in our subjects (mFWD > 0.6mm) has been shown to cause un-resolvable problems in functional connectivity analysis of resting state fMRI data, so it's unlikely that data with significantly more noise/motion would be considered useable [19].

Although very short scan lengths did have a significant impact on the FS STC technique, there was no detectable effect on scans until the scan length is shortened to about 35 time points. Typically, fMRI scans are much longer than this, and it would be very rare for this case to present itself in a research or clinical study. However, if the initialization period is a concern, this filter length can be reduced significantly with a tolerable amount of inaccuracy. One can anticipate reducing the filter length by one order of magnitude would only introduce a 5% loss of accuracy. Another possibility is to use infinite impulse response (IIR) filter, which requires a much lower filter order to achieve the same level of accuracy.

However, one might face the non-linear phase issue of the IIR filter, which needs to be addressed before being able to utilize it for fMRI data.

The effectiveness of STC interacted in a complex and nonlinear fashion with the TR of the fMRI scan. For traditional interpolation techniques, we were able to show that the benefit of STC is indeed minimal and insignificant at very short TRs. It may seem unusual that SR and FS STC do not converge with the other methods as the TR decreases. In theory, the errors introduced by interpolation through FSL and SPM's STC should become smaller and smaller, and approach the quality of the proposed FS method. Additionally, the sampling rate should not affect the quality of the shifted regressor or FS as long as the signal is band limited and the sampling rate is twice the Nyquist frequency. The inherent low pass filter present in our method is responsible for the significant increase in t-statistics at shorter TR. The BOLD signal contains high-frequency physiological noise, which can alias into the BOLD signal bandwidth, contaminating the signal in a way that cannot be removed by lowpass filtering. Increasing the sampling rate decreases the amount of aliased noise, until all the contaminants lie outside the pass-band. Once the noise is outside of the pass-band, the filter is significantly more effective, and is able to remove more noise from the signal.

When spatial smoothing is applied, the t-statistics from all methods reduce. For small smoothing kernels, it may appear that uncorrected data can actually outperform FSL and SPM, however it is important to remember that we examine a high delay slice, which is smoothed with the surrounding, low delay slices. If a low delay slice were examined, the uncorrected data would be smoothed with the surrounding, high delay slices, and we would not see the same increase as we do here. This can be seen in the sequential data, where the surrounding slices have a delay similar to the slice we're examining. In that case, we see no initial increase in correlation with the 3.5mm kernel, just a sharp drop. Even for interleave 2 and 6, as the kernel size increases, uncorrected data eventually performs worse than FSL or SPM. Importantly, our proposed method outperforms the SR method for smoothing kernels greater than 3.5mm. Based on the other experiments in this study, it may appear that the SR method is an optimal solution for the slice timing problem. In these other experiments, we presented a minimal preprocessing pipeline that is extremely uncommon in modern fMRI studies. The vast majority of fMRI preprocessing pipelines contain many other steps, including some sort of 3D spatial smoothing step. Any preprocessing step that involves a 3D operation (Such as motion correction or spatial smoothing) will destroy all benefit of the SR technique. For example, spatial smoothing uses a Gaussian kernel to calculate a weighted average of a voxel with all its surrounding voxels. If this kernel spans across slices, it averages signals with different temporal delays. This distorts the signal, and removes all benefit of slice-based regressors. Applying STC before spatial smoothing will outperform any slice-based regressor method. Since smoothing is a desirable preprocessing step, slice-based regressors cannot be considered an optimal solution to the slice timing problem.

Our analysis showed that there are still many sources of error and artifacts in fMRI data that overshadow the benefit of STC. Motion proved to be the most destructive confound in our analysis. In simulated data, high motion reduced t-statistics to a fraction of their value in motionless scans. Additionally, it significantly reduced the effectiveness of all STC methods, including our proposed optimal method. This was surprising in simulated data, as only slice-wise rigid-body motion was simulated, omitting spin-history artifacts and k-space filling artifacts. This means that even small misalignments between slices can create artifacts that cannot be moved with traditional realignment techniques. Motion is even more destructive in real data, as it contains the full range of motion-associated artifacts not present in the simulation. In order for our STC routine (or any STC routine) to perform optimally, it must operate on a clean signal, with as few artifacts as possible. It is clear from these results that current realignment techniques are unable to fully address the motion problem, and remove motion related artifacts. This causes issues for any preprocessing step to be carried out, and will lower the statistical power of any analysis, which may result in inaccurate conclusions drawn from noisy data with false positives or false negatives. To address this issue, motion correction must be examined critically in the context of a typical fMRI preprocessing pipeline. Additionally, a novel motion correction routine operating on first-principles of the interaction of motion with the MR signal is necessary to remove the remaining artifacts, which realignment is unable to correct.

4 Developing an Optimal Motion Correction Routine

4.1 Introduction

Motion is one of the most prominent sources of noise and artifacts in fMRI. Significant amounts of work has been devoted to reduce the artifacts of motion in the fMRI signal [49], [54], [63], [55]–[62]. Presently, there are two major directions of research in the fMRI motion problem: One direction is to remove motion related variance from motion contaminated data (retrospective correction), while the other is to prevent motion artifacts from occurring in the first place (prospective correction).

Perhaps the most common retrospective correction technique used in the field is the correction of spatial misalignment. Spatial misalignment is a consequence of head movement inside the scanner from volume to volume. Misalignment causes voxels to sample different locations in the brain over time. Spatial realignment using rigid body registration is often utilized to correct for misalignment retrospectively as a preprocessing step [64]. While rigid-body registration operates based on the assumption that head motion only occurs between volumes, in reality, motion continuously contaminates entirely/partially the acquired slices, and/or volumes, and may cause artifacts that persist after motion has ceased. Therefore, the effectiveness of spatial realignment is limited only to the volumes acquired well before and after the occurrence of motion. Though some slice-based registration methods exist [49], [65], they still will be unable to recover signal from regions that are under-sampled due to motion (such as part of the head moving out of the field of view (FOV) of the scan).

Typically, spatial realignment is unable to remove all motion related variance from the time-series. Because of this, it’s also common for researchers to attempt to subtract motion-induced signals from the data. In theory, this could reduce some of the variance present in these partially acquired slices/volumes that rigid body realignment can’t correct for. A major challenge with removing motion related variance is that it’s difficult to summarize three dimensional motion, and more importantly its effect on the signal, with a single metric (such as framewise displacement). Often times motion is described with any number of signals derived any number of ways, from simply using the motion estimates (and often numerous related measures such as their derivatives, time-delayed versions, and their exponentials) [63], [64], taking average signals from CSF or white matter voxels [66], [67], or by identifying motion related signals using ICA [68]. Additionally, advanced multi-echo pulse sequences have been used which allow researchers to separate BOLD (T2*) signal fluctuations from other sources of signal fluctuation, including those due to motion. By separating these signals, a more accurate regressor describing motion variance can be used to residualize the data [69], [70]. Despite all these advancements, one of the most effective existing retrospective techniques involves censoring all the volumes acquired not only during motion but also before and after its occurrence [63].

The other major direction of research, motion artifact prevention, aims to prevent these sources of variance from entering the scan in the first place. This strategy can be as simple as creating custom-padded molds for the subject to rest their head in during the scan [71], to the more advanced and technically challenging implementation of prospective motion correction. These techniques are desirable because they not only prevent misalignment, but also prevent another, even more destructive motion artifact known as "spin-history" artifacts [63], [64]. Spin-history artifacts arise due to the fact that fMRI operates in a steady-state by periodically exciting a slice with a relatively short repetition time (TR) which does not allow a full recovery of the net magnetization. If the steady-state of a system is perturbed, it can have a lasting effect on many volumes into the future, until steady-state can be reached again. Any over/under excitation due to motion-related displacement of the slice will disrupt the equilibrium of the steady-state acquisition, which causes spin-history artifacts. This can be caused with out-of-plane translation or rotation. These motions are particularly harmful, as they introduce both within-volume misalignments that distort the reconstructed image as well as spin-history artifacts that alter the magnitude of the signal. An example of spin-history artifacts are shown in Figure 4.1. The top row shows the effect of out-of-plane rotation that occurs half-way through an acquisition, while the bottom row shows out-of-plane translation. The first column shows an image sampled without motion, where each slice is represented by a different color. The center two columns show the effect of motion on the true location of the sampled slices, as well as the resulting reconstructed image. Note that both spin-history artifacts *and* slice-misalignment are present in this reconstruction, and that this kind of intra-volume misalignment results in a distorted image that cannot be corrected for with rigid body registration. The final column shows the volume immediately after motion. In this volume, spin-history artifacts are still preset (both over and under-excitation), and the volume is misaligned. While misalignment can be corrected for with rigid body registration, retrospective correction for spin-history artifacts is extremely challenging, and to our knowledge, there is no existing method to effectively restore the underlying signal once contaminated with spin-history artifacts [55], [64], [72], [73]. It is for this reason that prospective methods (which prevent spin-history artifacts) are proposed to address this issue. In prospective motion correction, the scanner coordinate system (defined by the gradient orientation) is constantly updated to "follow" any motion the subject's head may undergo. The optimal prospective method would require real-time motion tracking and gradient adjustment at each dwell time, which poses a technical challenge to be implemented with the current technology. However, current motion tracking and gradient adjustment are available for slice-by-slice application, and are implemented in several research laboratories [54], [73]–[81].

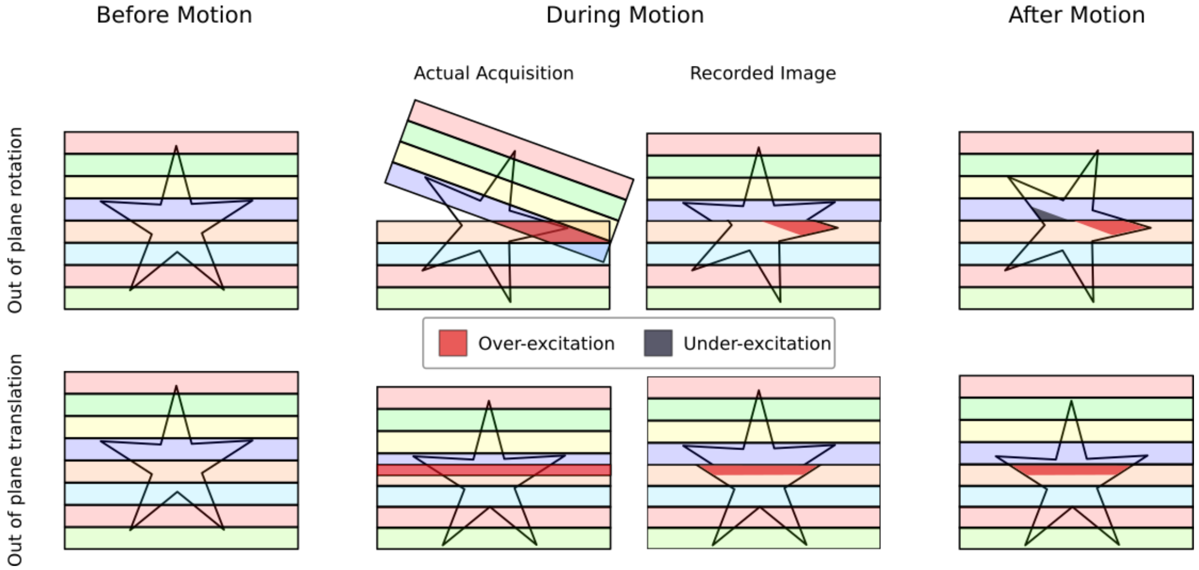

Figure 4.1: An illustration of spin-history artifacts for out-of-plane rotation and out-of-plane translation. An object is sampled slice by slice, from top to bottom, where each slice is shown as a colored bar. Without motion, the entire object is sampled normally without any artifacts, as shown in the first column. The center two columns represent image acquisition with motion, where the motion occurs half way through the acquisition of the object. The "Actual Acquisition" shows the actual location of the sampled slices for the given motion, while the "Recorded Image" shows the resulting reconstruction of the motion-contaminated volume. Finally, the column on the right shows the acquisition of the next volume, which is motionless, but is misaligned and has spin-history artifacts.

In its current state, slice-based prospective techniques leave an important motion artifact uncorrected: the motion artifacts caused by the displacement of k-space filling. K-space filling artifacts occur when motion disrupts the uniform sampling of k-space. Artifacts such as blurring, ghosting, or ringing in the reconstructed image are common effects of k-space displacement. Because of the small magnitude of the BOLD signal relative to the motion artifacts, it is imperative that these artifacts be optimally corrected or removed. Therefore, these artifacts will still need to be addressed, even if spin-history artifacts are prevented.

We start by investigating the distinct effect each kind of motion (such as translation versus rotation or in-plane versus out-of-plane) has on the acquired image by examining the theory of MR signal generation and the Bloch equation. Some of the findings were striking, for instance out-of-plane translation is shown to have zero effect on the MR signal during k-space filling. It is clear from our findings that a hybrid method is necessary to create an artifact free time-series: a prospective correction of the gradients to prevent spin-history artifacts, and a retrospective correction to remove any remaining artifacts due to distorted k-space filling. Using the results of our analysis, we propose a retrospective motion correction technique: Discrete reconstruction of irregular fMRI trajectory (DRIFT), to correct for within-slice motion artifacts. DRIFT does not require a real-time implementation. Instead our method retrospectively estimates the motion-related k-space displacement and places each k-space sample at its true location according to the type and amount of motion observed at each dwell time. In the presence of motion, the new k-space sampling points may not fall on a regular and uniformly spaced grid which prevents use of the inverse fast Fourier transform (IFFT) to reconstruct the images. Instead, we used an irregular inverse Fourier transform (IIFT) that is irregular in the frequency domain, but discrete in the spatial domain. An IIFT is significantly more time consuming, but it can be applied retrospectively and without a need for real-time implementation. To show the validity of our findings, and to demonstrate the effectiveness of our method, we used a comprehensive fMRI simulator to generate artifacts from various motion profiles. We evaluated the effectiveness of our proposed method by correcting every different type of motion, individually and in combination, using our fMRI simulator. We have also evaluated our method using a rotating phantom inside 3T Siemens Prisma scanner.

4.2 Theory

To study the effect of motion on the MR signal, it is essential to independently investigate the effect of each type of motion using the theory of MR signal generation and the MR signal equation. By examining the different components present in standard MR signal equation, the effect of motion can be modeled mathematically, and the signal change can be evaluated for any specific kind of motion. The signal detected by the coils in the MRI scanner is dependent on the proton density ρ of all the tissue excited by the latest RF pulse at a spatial location $\boldsymbol{r}$. This signal is commonly approximated as:

$$s(t) \;=\; \int_{\boldsymbol{r}} \rho(\boldsymbol{r}) e^{-i\boldsymbol{k}(t)\cdot\boldsymbol{r}}\, d\boldsymbol{r} \tag{4.1}$$

where $\boldsymbol{k}(t)$ is the k-space coordinate, defined as:

$$\boldsymbol{k}(t) \;=\; \gamma \int_0^t \boldsymbol{G}(t)\, dt \tag{4.2}$$

where γ is the gyromagnetic ratio and $\boldsymbol{G}(t)$ is the gradient vector, describing the strength of the magnetic gradients along the x, y, and z axes at time t. This equation demonstrates how a sequence of applied gradients change the location in the k-space over time. The pattern in which consecutive points of k-space are sampled during EPI is called the k-space “trajectory”, and the time between two consecutive sampling points in k-space is called the dwell time. The k-space trajectory traces a path along k-space, sampling the MR signal at designated points along the way. When each designated point in the trajectory has been acquired, a complete image can be reconstructed. This happens over a very short period of time, typically 60ms, which is twice the echo time (TE) of the fMRI pulse sequence.

The most common trajectory for sampling k-space in fMRI is a Cartesian grid. A Cartesian grid trajectory can be seen in Figure 4.2 (a), with its reconstructed image in (b). If the grid has uniformly spaced samples, the image can be reconstructed with an IFFT. Without loss of generality, we will assume for the rest of this article that the x axis is the frequency encoding direction, y is the phase encoding direction, and z is the slice selection direction.

4.2.1 Formulating the Effect of Motion on the MR Signal

We can now consider two coordinate systems: The object, $\boldsymbol{r_{ob}}$, and the scanner, $\boldsymbol{r_{sc}}$. Without motion, these coordinate systems are static, and we simply set them equal to each other, where $\boldsymbol{r} = \boldsymbol{r_{ob}} = \boldsymbol{r_{sc}}$. However, this no longer holds true if the object moves. When motion is present, we must describe the object's location relative to its initial position at the time of excitation from the most recent RF pulse. If the object is initially aligned with the scanner's coordinate system, $\boldsymbol{r_{sc}}$, and moves in a way described by a rotation matrix R and a translation vector $\boldsymbol{T}$ we can describe a point in the object's coordinate system in terms of the scanner's coordinates:

$$\boldsymbol{r_{sc}} = R(t)\boldsymbol{r_{ob}} + \boldsymbol{T}(t) \tag{4.3}$$

and it follows that we can describe a point in the scanner in terms of the object's coordinates:

$$R^{-1}(t)\boldsymbol{r_{sc}} - R^{-1}(t)\boldsymbol{T}(t) = \boldsymbol{r_{ob}} \tag{4.4}$$

This means a rotation of the object in the scanner is equivalent to the scanner making an inverse rotation while the object is stationary [82]. Treating the motion in the latter way actually results in a simplified analysis. To model the motion as a stationary object with an inverse rotation of the scanner, we re-derive the k-space equation to account for this rotation, as the spatial coordinate $\boldsymbol{r}$ is now changing with time. This process, along with the original derivation of k-space, is outlined in appendix B, and the results are shown here:

$$s(t) = \left(e^{i\gamma\int_0^t \boldsymbol{G}(t)\cdot\boldsymbol{T}(t)dt}\right).\int_{\boldsymbol{r_{ob}}} \rho(\boldsymbol{r_{ob}})e^{-i\boldsymbol{k}_R(t)\cdot\boldsymbol{r_{ob}}}\, d\boldsymbol{r_{ob}} \tag{4.5}$$

where $\boldsymbol{k}_R(t)$ is the new k-space location, which includes the motion related displacement, and is defined as:

$$\boldsymbol{k}_R(t) = \gamma \int_{\mathbf{0}}^{\boldsymbol{t}} R^{-1}(t)\boldsymbol{G}(t)dt \tag{4.6}$$

There is also an additional translation term which appears in front of the integral as it has no dependence on the spatial location $\boldsymbol{r}$. Equations (4.5) and (4.6) can now be used to examine the effects of different types of motion on the MR signal during k-space filling.

4.2.2 Effect of Translational Movement on the MR Signal

We first begin by examining the exponential term outside the integral, which corresponds to the effect of translation. To understand the motion artifact due to translation from a theoretical point of view, we can expand the dot products in equation (4.5), and reformulate the exponential in terms of its gradient vector components:

$$e^{i\gamma \int_0^t \boldsymbol{G}(t)\cdot\boldsymbol{T}(t)dt} = e^{i\gamma\left(\int_0^t G_x(t)T_x(t)dt + \int_0^t G_y(t)T_y(t)dt + \int_0^t G_z(t)T_z(t)dt\right)} \tag{4.7}$$

where $G_x(t)$ and $T_x(t)$ are the components of the gradient and translation vectors along the x axis, respectively. The same notation is also used for the gradient and translation along the y and z axes. As seen in equation (4.7), a gradient must be present along a given axis for translation in that direction to have any effect on the MR signal. However, a typical EPI pulse sequence uses only the frequency and phase encoding gradients during readout, and the slice selection gradient $G_z(t)$ is off during the entire period of k-space filling, making any translation along the z axis irrelevant to the MR signal. Artifacts due to translation along z only occur when the next z gradient is applied, which is usually concurrent with the next RF pulse, causing spin-history artifacts. Thus, if the subject's motion can be tracked, and the gradients can be adjusted to compensate for motion before the next RF pulse, the out-of-plane translation will have negligible effect on the acquired MR signal. This is not surprising since every tissue in the slice would still experience the same x and y gradient magnitude as it moves along the slice selection axis. On the other hand, translation along the x and y axes will cause a proportional phase shift in the acquired MR signal. This can be corrected for by multiplying the detected signal by an inverse phase shift to cancel out the artifacts of the translational motion. For bulk motion, the entire k-space is multiplied by a single phase shift, while for gradual motion occurring during k-space filling, each point in k-space is multiplied with a unique phase shift, dependent on the subject's motion at that point in time.

4.2.3 Effect of Rotational Movement on the MR Signal

We now examine the effects of in-plane rotation θ_z around the z axis, and out-of-plane rotation θ_x, and θ_y around the x, and y axes, respectively. For simplicity of notation, we drop the time index in this calculation and separately formulate the effect of each rotation by multiplying the gradient vector $\boldsymbol{G}$ by the respective rotation matrices for a rotation around each axis:

$$R_x\,\boldsymbol{G} = \begin{bmatrix} G_x \\ G_y\cos(\theta_x) - G_z\sin(\theta_x) \\ G_y\sin(\theta_x) + G_z\cos(\theta_x) \end{bmatrix} \qquad (4.8)$$

$$R_y\,\boldsymbol{G} = \begin{bmatrix} G_x\cos(\theta_y) + G_z\sin(\theta_y) \\ G_y \\ -G_x\sin(\theta_y) + G_z\cos(\theta_y) \end{bmatrix} \qquad (4.9)$$

$$R_z\,\boldsymbol{G} = \begin{bmatrix} G_x\cos(\theta_z) - G_y\sin(\theta_z) \\ G_x\sin(\theta_z) + G_y\cos(\theta_z) \\ G_z \end{bmatrix} \qquad (4.10)$$

Again, since there is no active gradient along z axis during the k-space filling, we can further simplify the above equation for rotational motion.

$$R_x\boldsymbol{G} = \begin{bmatrix} G_x \\ G_y\cos(\theta_x) \\ G_y\sin(\theta_x) \end{bmatrix} \tag{4.11}$$

$$R_y\boldsymbol{G}(t) = \begin{bmatrix} G_x\cos\left(\theta_y\right) \\ G_y \\ -G_x\sin\left(\theta_y\right) \end{bmatrix} \tag{4.12}$$

$$R_z\boldsymbol{G}(t) = \begin{bmatrix} G_x\cos(\theta_z) - G_y\sin(\theta_z) \\ G_x\sin(\theta_z) + G_y\cos(\theta_z) \\ 0 \end{bmatrix} \tag{4.13}$$

These equations demonstrate that both in-plane and out-of-plane rotations will introduce displacement to the sampled k-space locations. In the case of Cartesian sampling, the samples no longer lie on the expected uniformly spaced grid. This is illustrated in Figure 4.2 (c), which demonstrates an exaggerated in-plane rotation that occurs during the k-space acquisition. Figure 4.2 (d) shows the reconstructed image of this rotated k-space, with the associated reconstruction artifact for in-plane rotation. In the next excitation of this slice, if the gradients are not prospectively adjusted, the k-space samples will be uniform, but rotated, as shown in Figure 4.2 (e). The consequence of this is misalignment of the reconstructed image, shown in Figure 4.2 (f). It is important to note that the in-plane rotation artifact is limited to the slice in which the motion occurs, and will not contaminate future slices, other than misalignment.

The absence of a z gradient significantly reduces the magnitude of k-space sampling artifacts caused by an out-of-plane rotation around either the x or y axis. Equation (4.11) demonstrates that for typical rotations during a single k-space filling (usually less than 2 degrees) the magnitude of the gradient experienced by the object will remain around 99% of the original gradients, with only a small fraction appearing in the object's z axis, since cos(2°) = 0.99939, and sin(2°) = 0.035. Further, the gradient experienced along the axis of rotation remains unchanged, meaning if the object rotates around the x axis, it still experiences the same x gradient as it did before rotation. However, rotation around the z axis changes both the x and y gradients experienced by the object, and creates larger k-space sampling artifacts. In

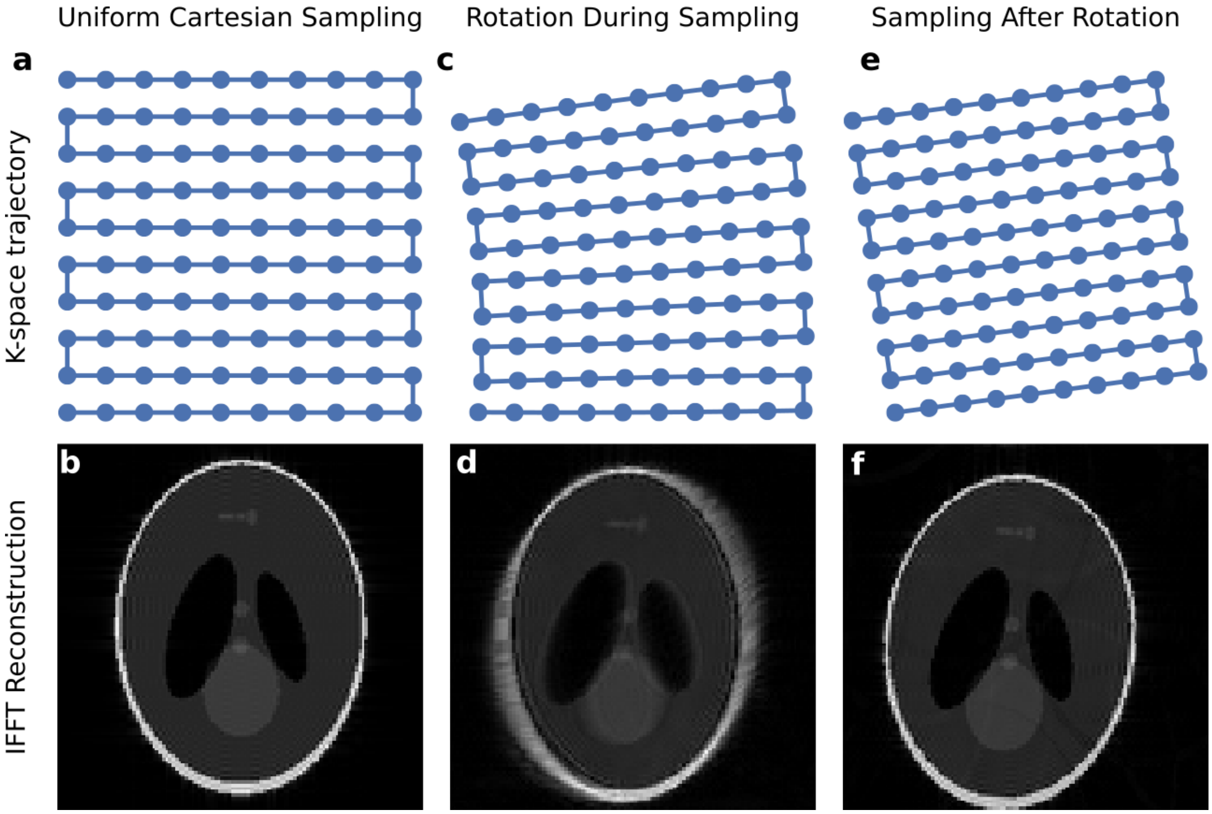

Figure 4.2: An illustration of the effect of motion on k-space sampling, and their associated artifacts.

(a) The EPI pulse sequence is designed to sample an evenly-spaced Cartesian grid in k-space (b) which results in a clean reconstruction. (c) Motion *during* K-space readout (in this instance, in-plane rotation) results in a distorted k-space. (d) This leads to artifacts in the reconstructed image. (e) K-space readout of a stationary, but rotated image is equivalent to sampling a rotated but uniform grid. (f) This leads to a reconstructed image without artifacts, but that is rotated by the inverse of the k-space rotation.

other words, we expect that in-plane rotation to generate larger displacement in the k-space locations, and therefore larger artifacts, than the out-of-plane rotation. To summarize the major theoretical points made in this section: 1) Translation along an axis can only cause signal artifacts if a gradient is present along the same axis. 2) Translation can be corrected for by multiplying the raw data with the appropriate phase shifts. 3) Rotation can be modeled directly as a change in k-space coordinates, and 4) In-plane rotation is significantly more detrimental than out-of-plane rotation.

4.2.4 Discrete Reconstruction of Irregular fMRI Trajectory (DRIFT)

We propose to use the derived equations for motion contaminated k-space to modify the classical fMRI reconstruction algorithm in a way that accounts for and removes all motion artifacts. Presently, all fMRI images are reconstructed using an IFFT, shown in equation (4.14).

$$s[m,n] = \frac{1}{N_x N_y} \sum_{k_y = 0}^{N_y - 1} \sum_{k_x = 0}^{N_x - 1} S[k_x, k_y] \cdot e^{i2\pi(k_x m/N_x + k_y m/N_y)} \qquad (4.14)$$

Where s is the reconstructed image at spatial coordinate [m, n], $S[k_x, k_y]$ is the sampled k-space point at k-coordinate k_x, k_y, and N_x, N_y is the total number of samples in the x and y axis respectively. In the IFFT, m, n, k_x, and k_y are discrete values, and it is assumed that every sample is evenly spaced in the range k = 0 to N-1, hence the relative frequency contribution of each sample is k/N of the maximum frequency.

While the IFFT algorithm fails to reconstruct the motion contaminated image, we can modify equation (4.14) to account for samples that are offset from their customary k/N location. If the motion is accurately measured, the true location of each k-space sample can be calculated from equation (4.6). It is at this point that most reconstruction steps would “regrid”, by interpolating k-space to estimate the values at uniform k/N locations. At no point do we interpolate our k-space, making our algorithm distinct from regridding methods. Instead, we modified (4.14) to account for irregularly sampled k-space, while leaving the image space discrete, making it a special case of a nonuniform Fourier transform.

For our purposes, it is more convenient to express the k coordinates k_x and k_y not as discrete variables, but as an array of k_x, k_y coordinates in the order in which they were sampled. We define these arrays as $k_x(t)$ and $k_y(t)$, which are given by equation (4.6). Essentially, $k_x(t)$ is the true x coordinate of k-space acquired at time t. Likewise, $k_y(t)$ is the true y coordinate of k-space acquired at time t. In this format, plotting $k_x(t)$ vs $k_y(t)$ would trace the k-space sampling trajectory, like those shown in Figure 4.2 (a), (c), and (e). We also add a phase compensation factor to account for translation induced phase shifts, shown in equation (4.15):

$$s[x,y] = \frac{1}{N_x N_y} \sum_{t=0}^{N_x N_y - 1} \left(\boldsymbol{e}^{-iT(t)}\right) S(t)\, e^{i2\pi\left(k_x(t)x/N_x + k_y(t)y/N_y\right)} \tag{4.15}$$

$$T(t) = \gamma \int_0^{\boldsymbol{t}} \boldsymbol{G}(t') \cdot \boldsymbol{T}(t')dt' \tag{4.16}$$

where and $S(t)$ is raw fMRI data at coordinates $k_x(t)$ and $k_y(t)$. If there is no translation, $T(t)$ equals zero, and so the exponential factor reduces to 1. The full equation reconstructs irregularly sampled k-space trajectories into discrete image space. The DRIFT algorithm can be applied directly to motion-contaminated data.

If the rotation $R(t)$ is known at every dwell time, equation (4.6) can be used to calculate $k_x(t)$ and $k_y(t)$. One way to achieve this would be to use a high-speed motion capture camera, which could record the subject's position at every point in time. This could then be used retrospectively to reconstruct the raw data when time is not an issue. However, the dwell time in a typical fMRI acquisition is anywhere between 5-12μs, which would require around 200,000 fps, which is well beyond the capabilities of MR compatible video cameras. If motion cannot be measured at every dwell time, we are still able to estimate the k-space coordinates at each dwell time if motion is sampled at a reasonably fast rate. In order to determine how fast the motion must be sampled for our estimations to be accurate, we examine the motion profile of over 6,000 scans, and found that 99% of real subjects' motion parameters are between +/- 0.5mm for translation, and +/- 0.5 degrees for rotations over a 2 second TR. Even for the extreme outliers, the maximum rotation found was 7 degrees over a 2 second TR. The primary concern with sampling such high rotations is the smoothness of the movement between samples. Typically, biological movements are relatively slow. One of the fastest motions a human can make is a blink of the eye, and even this lasts around 200ms. As head motion is certainly slower than this, we determine that measuring the motion once per slice (usually around 60ms) is more than enough to accurately estimate the motion using linear interpolation. This corresponds to a frame rate of less than 20 fps, which is easily achievable for any MR compatible video camera. In fact, many cameras are capable of recording over 200 fps, which would even further improve our motion estimates.

Because of the relatively slow nature of biological movements, we can assume that the amount of motion at each dwell time can be estimated by linear interpolation. For example, to model in plane rotation, if $k_x(t)$ and $k_y(t)$ are the intended motion-free k-space coordinates, the motion contaminated coordinates can be estimated as:

$$k'_x(t) \ = \ k_x(t) \, cos\left(\frac{t\theta}{N_x N_y} + \alpha\right) - k_y(t) \, sin\left(\frac{t\theta}{N_x N_y} + \alpha\right) \tag{4.17}$$

$$k'_y(t) \ = \ k_x(t) \, sin\left(\frac{t\theta}{N_x N_y} + \alpha\right) - k_y(t) \, cos\left(\frac{t\theta}{N_x N_y} + \alpha\right) \tag{4.18}$$

Where α represents any bulk rotation that has already occurred before k-space sampling (Accounting for offsets as in Figure 4.2 (e)). This evenly distributes a rotation of angle θ over $N_x * N_y$ time points, thus making $k'_x(t)$ and $k'_y(t)$ an incrementally rotated version of the intended trajectory, $k_x(t)$, $k_y(t)$. A similar procedure can be used to calculate the k-space coordinates for any rotation around the x and y axis.

By using either the estimated k-space coordinates from equations (4.17) and (4.18), or the true k-space coordinates from equation (4.6), we are able to completely recover irregularly-sampled k-space images for all plausible motions expected to be found in a typical fMRI scan. This algorithm is extremely versatile in its application. Not only can it be applied on a slice by slice basis to correct for k-space motion artifacts, but it can also be used to correct for bulk in-plane motion artifacts to realign slices and volumes without the need for interpolation. DRIFT is a slice-based correction routine which can remove artifacts due to distorted k-space filling, and correct for bulk misalignment within plane. Out of plane misalignment and any associated spin-history artifacts cannot be corrected for by DRIFT, highlighting the need for prospective motion correction.

We now rigorously test the performance of our method in a variety of realistic fMRI conditions, using both real and simulated data. We use FSL's Physics-Oriented Simulated Scanner for Understanding MRI (POSSUM) [82], [83], a Bloch-equation based fMRI simulator to confirm the theory section of this paper. We examine the effects of various in-plane and out-of-plane motions on the fMRI signal, and the ability of DRIFT to remove them. Finally, we use a rotating phantom to test the application of our method on 3T Siemens Prisma scanner.

4.3 Methods

4.3.1 Simulated Data

In order to create our simulated data, POSSUM requires a set of acquisition parameters, a pulse sequence, and a target object with a defined geometry and spatially varying T_1 recovery and T_2 relaxation rates as inputs. The POSSUM simulator then takes the pulse sequence and target image as inputs, and generates an MR signal by simulating the proton spins in a static magnetic field, and solving the Bloch equation at every point in time during the scan. POSSUM also simulates rigid body motion of the object for any given motion parameters, which carries out motion at every update of the Bloch equation, allowing for the simulation of motion during readout and RF excitation.

Our simulated fMRI data in this study consisted of 21 brain volumes, each with 7 slices, with simulated motion occurring during the acquisition of the center slice (slice 4) in volume 10 for all cases. Our target object was POSSUM's default high resolution brain image (voxel size 1mm x 1mm x 1mm, FOV 181mm x 217mm x 181mm), containing tissue segmentation for white matter, grey matter, and CSF. Each tissue type has a pre-defined T_1 recovery, T_2 relaxation, and proton density value: (Grey matter: T1 = 1.331s, T2 = 0. 051s, ρ = 0.87. White matter: T1 = 0.832s, T2 = 0.044s, ρ = 0.77. CSF: T1 = 3.7s, T2 = 0.5s, ρ = 1.0). For all simulations, the read direction was aligned with the x axis, and phase encoding along y. Slice selection was performed along the z axis, and the main magnetic field strength was 3 Tesla. Noise is added to the simulations to represent a realistic scan. POSSUM simulates system noise as independent, additive white Gaussian noise in the receiver channels, so the noise is present in the k-space before reconstruction. We chose a standard deviation of 0.01658 (units of intensity) to match the temporal SNR found in the real data acquired for this experiment, defined as the mean temporal signal divided by the standard deviation of the noise (commonly called tSNR) [84]. No B_0 inhomogeneities or chemical shifts were added to the simulation to better focus on the effects of motion. The fMRI scan dimensions were 112x112x7 voxels, with a voxel size of 2x2x4mm, giving a 224x224x28 FOV. Our simulated pulse sequence had a TE of 60 ms, a TR of 1.0s, and a 60 degree flip angle. We choose a higher TE than most fMRI pulse sequences to magnify motion artifacts for the purpose of highlighting how motion effects the fMRI signal.

We chose 10 different kinds of motion with two different motion profiles to simulate in POSSUM. These motions are categorized as in-plane and out-of-plane and listed in table 1: 1) 5 degree rotation around z. 2) 5mm translation along x. 3) 5mm translation along y. 4) 5mm translation along both x and y together. 5) 5mm translation along y with a 5 degree rotation around z. 6) 5 degree rotation around x. 7) 5 degree rotation around y. 8) 5mm translation along z. 9) 5 degree rotation around y with prospective motion correction, and 10) 5 mm translation along z with prospective motion correction. Scans 1-5 simulate “in-plane” motion, meaning the motion occurs in a way so that the excited tissue remains within the plane of acquisition, and does not cause any disruption to the steady-state. These scans demonstrate DRIFT’s ability to remove k-space motion artifacts from in-plane motion. Scans 6-8 demonstrate out-of-plane motion with the harmful effect of spin-history artifacts, and scans 9-10 simulate prospective motion correction and demonstrate that if spin-history artifacts are avoided, DRIFT can again correct for any readout motion artifacts that are present.

The profiles of the simulated motion relative to the pulse sequence are shown in Figure 4.3. The RF pulse, z, y, and x gradients are depicted in the first 4 lines, respectively. The 5th line, labeled “Mot”, refers to the relative displacement of the object, and can in general refer to any type of motion. The line can indicate a translation, rotation, or combination of the two along any or multiple axis, and is intended to demonstrate the relative timing of the motion in the pulse sequence. In Figure 4.3 (a), motion begins at the first point of k-space sampling, and continues linearly until the end of slice acquisition. The target then remains at its final position for the remainder of the scan. This is referred to as motion profile “a”, and would result in misalignment, as well as spin-history artifacts if out-of-plane motion is present. The second motion profile, shown in Figure 4.3 (b), begins the same as Figure 4.3 (a), where motion starts at the beginning of k-space sampling and ends and the end of readout. However, in this profile, the object returns to its original position before the next RF pulse, as indicated by the "Mot" line returning to zero. This would not cause spin-history artifacts, regardless of the type of motion. This is referred to motion profile "b", and is equivalent to adjusting the gradients to account for subject motion, as in prospective motion correction.

While each of the above simulations were created with exaggerated movements to examine the effects of different types of motion on an fMRI image, it is important to also examine the effect of real subject motion in our simulation. Therefore, another simulation consisting of 41 volumes is performed with similar acquisition and target parameters as our previous simulations, but with in-plane rotation and translation parameters estimated from a real subject motion during a task-based fMRI scan (mean framewise rotation = 0.4 degrees, and mean framewise translation = 0.3mm). 36 in-plane rotation measurements were used from this simulation, and the first 5 volumes were simulated with no motion to reach the steady-state, and volume 5 was used as a reference volume. We use this simulation to demonstrate the effectiveness of DRIFT on a scan with more realistic motion, rather than the large, isolated movements used in our previous simulations. Each rotation/translation occurs over the length of a full TR, rather than a single TE, as in the previous simulations.

Simulation Type	**Sim #**	**Motion Type**	**Motion Profile**	**Rx**	**Ry**	**Rz**	**Tx**	**Ty**	**Tz**
In-plane	1	*Z-axis Rotation*	*a*	-	-	**5°**	-	-	-
	2	*X-axis Translation*	*a*	-	-	-	**5mm**	-	-
	3	*Y-axis Translation*	*a*	-	-	-	-	**5mm**	-
	4	*X and Y-axis Translation*	*a*	-	-	-	**5mm**	**5mm**	-
	5	*Z-axis Rotation and Y-axis Translation*	*a*	-	-	**5°**	-	**5mm**	-
Out-of-plane	6	*X-axis Rotation*	*a*	**5°**	-	-	-	-	-
	7	*Y-axis Rotation*	*a*	-	**5°**	-	-	-	-
	8	*Z-axis Translation*	*a*	-	-	-	-	-	**5mm**
	9	*Y-axis Rotation*	*b*	-	**5°**	-	-	-	**-**
	10	*Z-axis Translation*	*b*	-	-	-	-	-	**5mm**

Table 1: 10 motion profiles used for simulated data

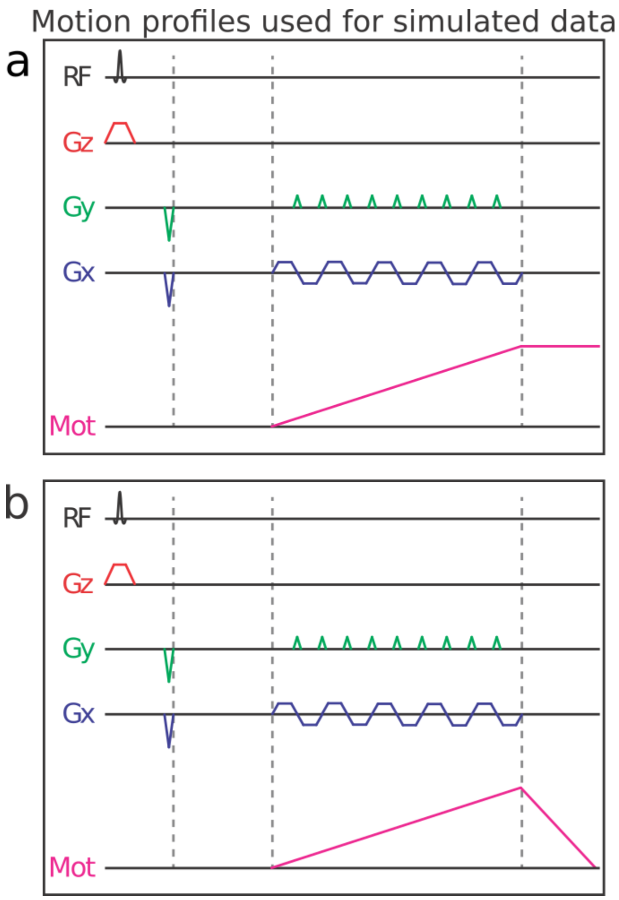

Figure 4.3: An illustration of the motion profiles used in simulated data

(a) The motion begins after RF excitation at the start of k-space readout. Motion ramps continuously until the end of k-space readout, at which point the object stops moving and remains at its new position. (b) The motion begins as in (a), after RF excitation and at the start of k-space readout. Motion ramps continuously until the end of k-space readout, at which point the object quickly returns to its original position before the next RF pulse.

4.3.2 Real Data

An in-house MRI-compatible phantom capable of in-plane rotation was developed and used to acquire our real data using a Siemens 3T Prisma scanner. The phantom consists of two parts: an imaging portion which has identifiable geometry and can be filled with agar gel, and a driver portion, which includes fan blades and can be rotated with air pressure in a controlled manner. We designed the phantom using FreeCAD, and fabricated the structure using a Formlabs Form 2 stereolithography 3D printer. The phantom is a hollow cylinder 2.25 inches tall with a 4 inch diameter. The phantom was printed with photoreactive resin RS-F2-GPCL-04 consisting of a proprietary mixture of methacrylic acid esters and photoinitlators. Several geometric shapes protrude from the base of the phantom to provide contrast for scanning, shown in Figure 4.4. An agar solution was created and poured into the phantom and allowed to solidify. The agar solution was 15% salt by weight to prevent bacterial growth on the agar gel. The phantom was mounted on the driver portion to allow for rotation. A pressure regulator was used to maintain a relatively constant PSI which allowed a controlled rate of rotation. Rotation rate was measured through manual realignment of fMRI scans. A full depiction of our setup is shown in Figure 4.5.

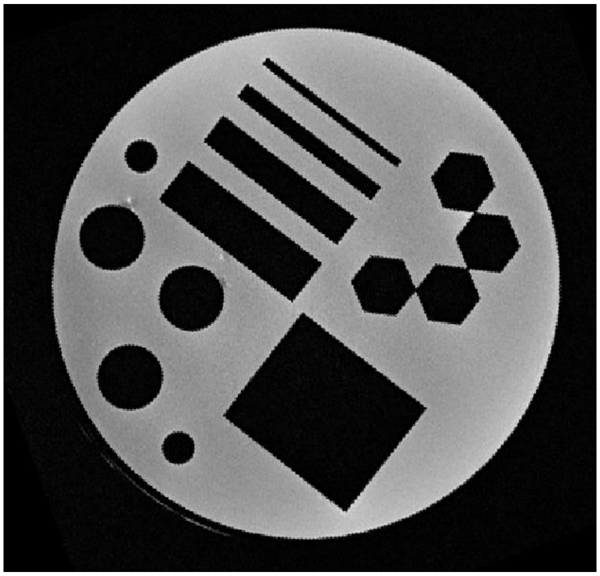

Figure 4.4: A high-resolution T2 image of the agar filled phantom used for real data scans.

We began the scan with 10 seconds of motionless volumes to use as a reference and to calculate SNR at baseline. Then, the airflow was turned on to allow moderate rotation to take place over the next 40 seconds. The airflow was shut off in time to allow the phantom to come to rest for the final volumes of the scan. The framewise rotations for our scan ranged between 1 and 130 degrees with a median rotation of 54.5 degrees (0.15 hz). One coronal slice was acquired with a 64x64 matrix, with an FOV of 127x127x2mm. We used a basic EPI pulse sequence, with a TR/TE of 1.0s/30ms, flip angle 90, with no slice acceleration. The phantom was placed inside a 64 channel head coil which was used for image acquisition. We acquired 60 volumes, the first 10 of which were stationary, followed by 38 volumes of motion, and an additional 12 volumes at the end of the scan with no motion, but at a random angle offset from the initial orientation. Both the Siemen's reconstructed DICOM images, as well as the raw data were acquired and used in processing.

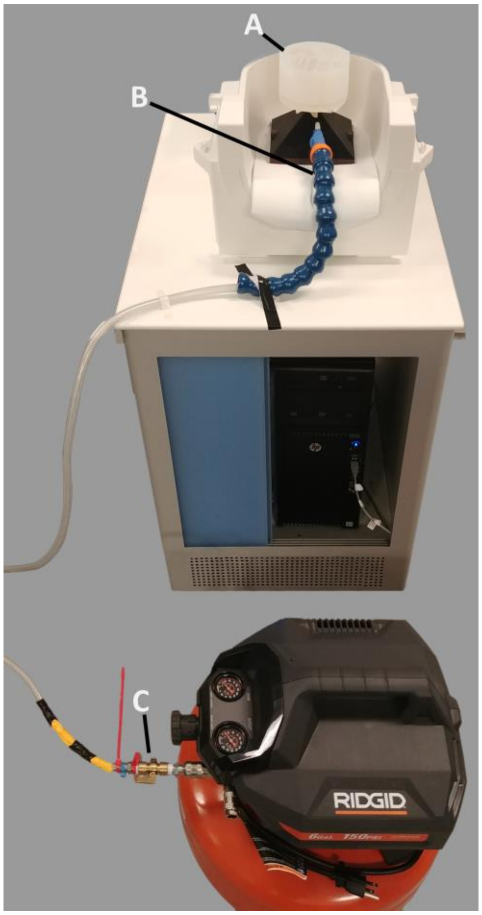

Figure 4.5: Setup of the rotating phantom.

(A) The imaging section of the phantom rests atop its rotating stand in a head coil. (B) A directional nozzle focuses air flow onto the fan blades in the rotating stand. (C) The pressure regulator and flow control valve which allow us moderate control over the degree of rotation.

4.3.3 Simulated Data Processing Pipeline

The reconstruction provided by POSSUM is contaminated with k-space motion artifacts and misalignment, and is referred to as the “uncorrected” data, meaning no motion correction has been applied. We then use fMRI realignment software to perform rigid body realignment on the data. This is referred to as the “realigned” data set. Because the motion parameters are known, we are able to provide precise rotations and translations to the realignment software, eliminating any possible artifacts due to inaccurate motion estimation. For the volume in which motion occurs in, half of the slices are acquired normally, then motion is applied during one slice, and the remaining half of the slices are acquired with misalignment. This is problematic for rigid body registration, as half the brain is misaligned. For this volume, the average motion across all slices was used to realign the volume. Finally, we create the “DRIFT” reconstruction using the provided pulse sequence, known motion parameters, and raw data. We calculate the effect of motion on the k-space trajectory using custom python code that evaluates equations (4.6) and (4.7). We then use these true k-space coordinates to reconstruct the raw data using DRIFT.

While most modern MRI scanners discard initial volumes that aren’t in steady-state, POSSUM leaves the scans in the simulation. These volumes have a different intensity and contrast than the later volumes that have reached steady-state. We discard the initial 5 volumes from the simulations, at which point the voxel’s have settled to 99.99% of their steady-state value. After reaching the steady-state, we do not expect to detect any change in the reconstructed images except the additive white Gaussian noise. Any further change in the signal should be attributed to the motion. We quantify the effect of motion for each reconstruction by computing the percent difference (PD) between each motion contaminated/corrected slice and the uncontaminated slice acquired in volume 8, henceforth referred to as the reference volume. Percent difference is computed by following equation.

$$\mathrm{PD} = \left[\frac{S(x,y,z,t)}{S(x,y,z,t_{ref})} - 1\right] * 100 \qquad (4.19)$$

Where t_{ref} is the timepoint of the reference volume to be used as a baseline. We then calculated the PD for a motionless volume (“Before Motion”, volume 9), the volume in which the motion occurred (“During Motion”, volume 10), and the volume acquired immediately after motion (“After Motion”, volume 11). Any error in the “Before Motion” volume is due to noise, while any additional error in the “During Motion” volume is due to motion artifacts during slice acquisition. Finally, any changes in the volume after motion are due to bulk motion and/or spin-history artifacts. For the 10 scans examining exaggerated subject motion, PD is calculated only for slice 4, which is the slice that motion occurs in, and will have the artifacts associated with k-space displacement. For the simulation with real subject motion, we chose volume 5 to be used as a reference volume (as all previous volumes are not in steady-state, and all following volumes have motion), and calculate the PD over the entire volume, since motion now occurs over the entire volume rather than one single slice. 95% confidence intervals are bootstrapped for the PD’s of each reconstruction method and shown in the resulting analysis [85]. Statistical inference is done on voxel-wise PD values using a repeated measures two-sided t-test.

4.3.4 Real Data Processing Pipeline

There are very few tools available to process raw k-space data. Because our algorithm must be implemented in place of a normal IFFT reconstruction, it was necessary to create our own python code to reconstruct and process the images. First, the raw k-space data from all 64 channels is read into the processing pipeline where noisy channels are removed by examining the correlation of each channel with all other channels. A correlation below 0.5 was used as an exclusion threshold, which occurs only when the SNR is extremely low. Upon inspection, the channels omitted with this process had little or no recognizable image in its reconstruction. We then apply a small hamming window filter on the high-frequency k-space components to suppress high frequency noise, which is a common step in many k-space reconstruction routines [86]–[88]. The window is applied to the 14 outermost k space samples in the x and 7 outermost k-space samples in the y direction, as Siemen's oversamples in the read direction (x) by a factor of 2. We then use the calculated k-space coordinates with the DRIFT algorithm to reconstruct two images, one image from the odd read samples and one from the even read samples. The average of these two images is stored as the reconstructed image for a single channel. The channels are then combined using a root sum squared method. We also create a second reconstruction, using identical processing steps with the exception of the motion correction portion of DRIFT. This data by itself is not corrected for motion in any way, and is referred to as the "uncorrected" data set. We then run realignment on this data, using the same method described for simulated data, to evaluate the effectiveness of traditional realignment methods. This leaves us with three reconstructed scans: Uncorrected, realigned, and DRIFT corrected data. This gives us a direct comparison on the effect of DRIFT on the reconstructed data, with no additional confounds in the preprocessing stream.

To quantify the amount of motion at each volume, we used the scanner reconstructed images to manually estimate motion between volumes. The first volume was chosen as a reference. The absolute rotation of each volume relative to the reference was estimated visually using Freeview. We also measured the relative rotation of each volume to the previous volume. The relative rotation to the previous volume gives the total rotation over one TR. Dividing this rotation by the TR gives an estimate of the rate of rotation in degrees per second for that volume. This rotation is used to estimate the true locations of k-space samples as in equations (4.17) and (4.18). In the EPI pulse sequence implemented by Siemens, signal acquisition occurs during the ramp up, plateau, and ramp down portion of the readout gradient. This leads to non-uniformly spaced k-space samples. Siemen's fMRI reconstruction will use some form of regridding to compensate for this ramped sample trajectory, however since our method is already able to account for irregular sampling offsets, we simply use the true, nonuniform k-space points, and apply the appropriate rotation directly to them. An example of the sampling trajectory for a single read line is stored in the raw data header, which we extract and use to generate our k-space.

Due to intensity distortions and non-uniformity in the rotating reconstructed images, we could not use PD as our measurement for quantitative evaluation of DRIFT. Instead we calculate the mutual information between each volume in each reconstruction and a baseline volume. We generate our baseline volume by averaging the first 10 motionless scans. DRIFT is able to reconstruct the raw data without introducing any interpolation error or smoothing to the reconstructed image, whereas interpolation of any kind contains an inherent low-pass filter effect, causing a slight smoothing of the image. It is well known that smoothing can inflate or induce correlations between two images or signals [48], [89], [90]. For a fair comparison, we calculate the effective equivalent Gaussian smoothing kernel to replicate the smoothing induced by realignment. To do this, we extracted the final volume from the realigned scan, and calculated its correlation with the first volume in the uncorrected scan. The uncorrected scan was then smoothed with Gaussian kernels of increasing size, incrementing the FWHM by 0.1mm. We plot the correlation as a function of the smoothing kernel's FWHM in Figure 4.6 (a). The maximum correlation is taken as the effective FWHM of interpolation, corresponding to 2.38mm, or a standard deviation of 1.01mm. Upon visual inspection, the smoothed image was visually indistinguishable from the rigid-body realigned image, as shown in Figure 4.6 (b) and (c). We applied this kernel to both the uncorrected and the DRIFT corrected data to remove smoothing-induced correlation as a confound. Similar to the simulated data, statistical inference was carried out as a repeated measures two-sided t-test on mutual information measurements.

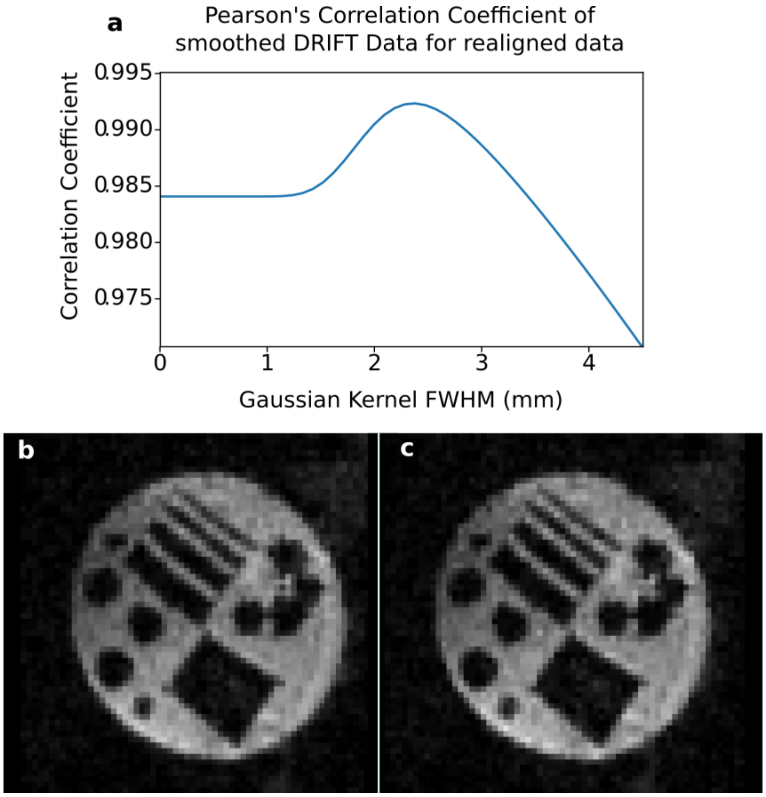

Figure 4.6: Estimation of smoothing effect of interpolation.

(a) A stationary but misaligned volume is selected, and it is realigned to a reference slice. The reference slice is then smoothed with progressively larger Gaussian kernels, and the correlation is calculated between the realigned volume and the smoothed reference at each iteration. A maximum correlation was found with a Gaussian FWHM of 2.3mm. (b) Volume 48 of the DRIFT corrected data with a 2.3mm FWHM smoothing kernel. (c) Volume 48 of the realigned volume, with no smoothing other than that inherent in interpolation.

4.4 Results

We first use simulated fMRI data to demonstrate that each type of motion generates strikingly different types of artifacts. Next we use data collected from a rotating phantom to establish the proof of concept for our proposed method of hybrid motion correction.

4.4.1 Effects of In-Plane Motion and Its Correction

In-plane motion does not disturb the steady-state of the EPI sequence, therefore they will not cause any spin-history artifacts. Figure 4.7 illustrates the results of our simulation for in-plane motion. In this simulation, during the acquisition of one slice (slice number 4) in volume 10, a 5 degree rotation around z and/or 5mm translation along the x or y axes is applied to the target object. The top row in Figure 4.7 depicts the artifact of each type of in-plane motion on the reconstructed image using simulated data with an exaggerated motion profile. To make the artifacts visually identifiable, the simulated motion in this row is three times larger than the motion used in bottom 2 rows. These exaggerated simulations are used only in the top row for visualization, and all statistical comparisons are carried out on the data described in the methods section. The blurring on the boarder of the brain and ringing effects inside the brain are visible in this row. Furthermore, a severe geometric distortion is also visible particularly for the combination of translation and rotation.

To investigate the actual differences in the fMRI signal, we computed the PD, as defined in the method section, between the selected slice (slice 4) in a reference volume (volume 8) and the slice acquired immediately before applying motion (in volume 9), the slice acquired during the motion (in volume 10), and the slice acquired immediately after motion (in volume 11). The middle row in Figure 4.7 shows the PDs for uncorrected, realigned and DRIFT corrected data. Before motion, there is a constant 3.8 PD across all three methods and for all five types of in-plane motion. This is due to the additive white Gaussian noise in our simulated data, and represents the lowest possible error in a motionless volume. Motion will introduce error and artifacts into the reconstruction, which will raise the PD above this value. Successfully correcting for motion will bring the PD back down to this baseline value.

The difference between uncorrected, realigned and DRIFT corrected slices became significant for the slice acquired during motion. As expected, realignment significantly reduced the motion artifact depicted in the top row in comparison to the uncorrected slices (PD_{diff}=6.6, $p < 10^{-5}$, for 5 degrees rotation around z; PD_{diff}=8.9, $p < 10^{-5}$, for 5mm translation along x axis; PD_{diff}=8.7, $p < 10^{-5}$, for 5mm translation along y; PD_{diff}=10.8, $p < 10^{-5}$, for 5mm translation along x and y; PD_{diff}=8.7, $p < 10^{-5}$, for 5 degrees rotation around z and 5mm translation along y). However, there are still remaining artifacts in all five cases of in-plane motions. Using DRIFT not only significantly reduces the PD between the realigned and DRIFT corrected slices (PD_{diff}=1.7, $p < 10^{-5}$, for 5 degrees rotation around z; PD_{diff}=1.9, $p < 10^{-5}$, for 5mm translation along x; PD_{diff}=1.2, $p < 10^{-5}$, for 5mm translation along y; PD_{diff}=2.3, $p < 10^{-5}$, for 5mm translation along x and y; PD_{diff}=1.9, $p < 10^{-5}$, for 5 degrees rotation around z axis and 5mm translation along y), but also the improvement reached the point that there was no significant difference between the motionless slice and DRIFT corrected slice during motion ($p > 0.05$ for all motions), suggesting that DRIFT can potentially remove the motion artifact completely from the motion contaminated slices acquired during any in-plane movement.

After motion, the PD for the uncorrected slice increases compared to the slice acquired during motion. This is due to the fact that motion contamination accumulates gradually over the k-space filling; as shown in Figure 4.2 (c), there is a negligible motion artifact in the beginning of k-space filling, whereas it becomes most dominant at the end. However, the slice acquired in the next volume is completely rotated/translated causing an increase in the PD for the uncorrected slice. While realignment should correct for post-motion displacement, the interpolation artifact during the spatial transformation prevents the PD from reaching its baseline value before motion, causing a significant difference between the realigned and DRIFT corrected slice (PD_{diff}=0.8, $p < 10^{-5}$, for 5 degrees rotation around z; PD_{diff}=1.0, $p < 10^{-5}$, for 5mm translation along x; PD_{diff}=0.6, $p < 10^{-5}$, for 5mm translation along y; PD_{diff}=1.6, $p < 10^{-5}$, for 5mm translation along x and y; PD_{diff}=0.7, $p < 10^{-5}$, for 5 degrees rotation around z and 5mm translation along y). This results highlight the superiority of the DRIFT motion correction technique even for simple instantaneous transformation compared to conventional spatial transformations.

The bottom row in Figure 4.7 shows the computed PD for slice number 4 in all 20 simulated volumes in uncorrected, realigned, and DRIFT corrected data. The dots on the curve mark the mean of the PD and the shaded band around each curve illustrate the 95% confidence interval at each point of computation. As demonstrated by this figure, all three scans reach their steady-state by volume five, and drop to zero at volume 8 (the selected reference for computing PD). They return to their steady-state value at volume 9. The motion contaminated slice in volume 10 demonstrates an abrupt increase in PD in both uncorrected and realigned slices whereas the DRIFT corrected slice remains unchanged. In volume 11, after the occurrence of motion, the uncorrected slice reaches its highest PD and remains constant from that point on, whereas realignment slightly but significantly reduces the PD of the slice acquired after motion and remains constant afterward. DRIFT corrected slices have unchanged PD that remain identical to the PD in "before motion" volumes, indicating a complete removal of in-plane motion artifacts.

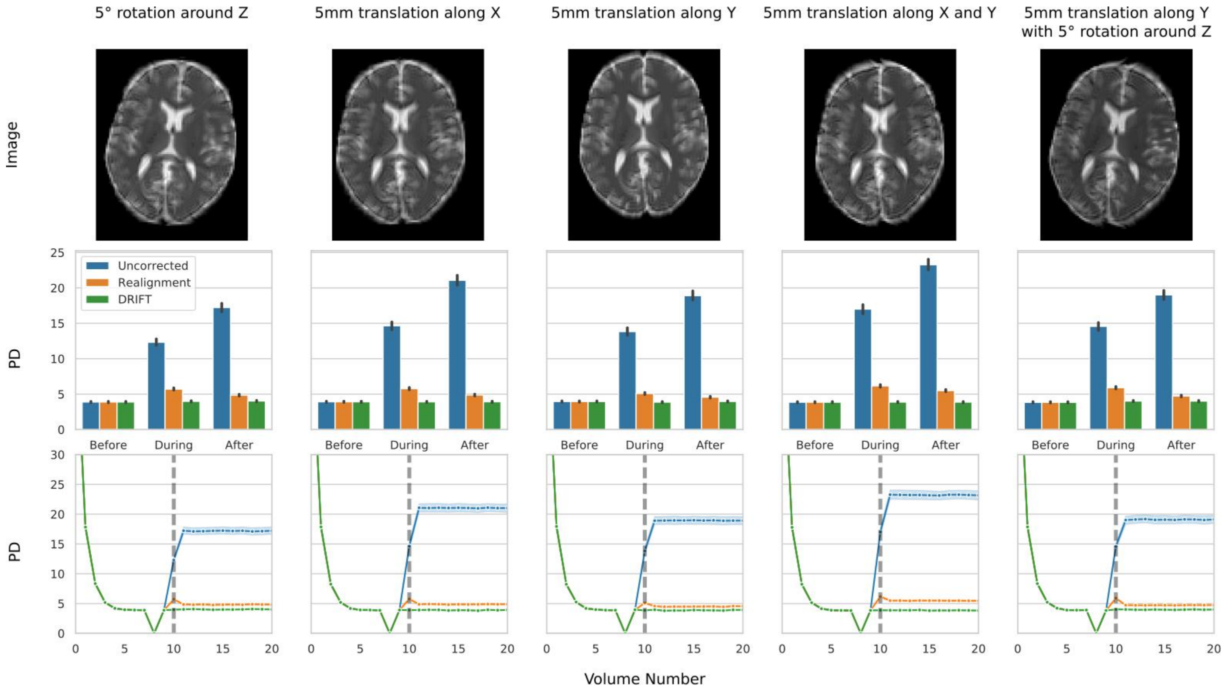

Figure 4.7: Artifacts and PD for in-plane motion, in simulated data.

(Top) Illustration of the artifacts that occur for different types of in-plane motion. (Middle) PD calculated for the slice in which motion occurs for the volume before, during, and after motion. (Bottom) Time-series of the PD calculated for the slice in which motion occurs for the entire simulation. Volumes 9, 10, and 11 correspond to the before, during, and after volumes respectively, used in the middle row.

To summarize, uncorrected data has the largest PD for all during and after motion volumes. Realignment significantly reduces this error, but is unable to account for k-space filling artifacts, and still has significant interpolation error in the volumes after motion. DRIFT significantly reduces the PD beyond what realignment can do in all cases, and all DRIFT reconstructed volumes are not significantly different from the motionless baseline.

4.4.2 Effects of Out-of-Plane Motion and Its Correction

As discussed in the method section, out-of-plane motion disturbs the steady-state of the fMRI acquisition, thus causing spin-history artifacts which has a lasting effect up to a few volumes after the occurrence of motion. Figure 4.8 illustrates the results of our simulation for out-of-plane motion. In this simulation, during the acquisition of one slice (slice number 4) in volume 10, we show the effect of a 5 degree out-of-plane rotation around x, a 5 degree out-of-plane rotation around y, as well as a 5 mm translation along z. In addition, in order to simulate the effect of prospective correction applied simultaneously with DRIFT, we rerun the simulations of a 5 degree rotation around y axis and a 5 mm translation along the z axis using the motion profile shown in Figure 4.3 (b), and applied a fast inverse motion to the target object to come back to its original location before application of next slice selection RF pulse.

The top row in Figure 4.8 depicts the artifact of each type of motion on the reconstructed image using simulated data with an exaggerated motion profile. To make the artifacts visually identifiable, the simulated motion in this row is three times larger for rotation and translations. These exaggerated simulations are used only in the top row for visualization. A white box is placed around each brain volume that has the exact dimensions of a motionless slice. The artifacts due to out-of-plane motion are extremely small, but can be seen as a slight compression of the image, indicated by a small gap between the brain and the white box, highlighted by red arrows. Note that there are no gaps for the z translation volumes. We have already demonstrated these results through equations (4.7), (4.11), and (4.12), where, according to our equations, the out-of-plane translation should not cause any artifact on the slice where the translation took place.

The middle row in Figure 4.8 shows the PDs for uncorrected, realigned and DRIFT corrected slice before, during, and after out-of-plane motion. Similar to in-plane simulations, before motion there is a constant 3.8 PD across all three methods and for all five types of out-of-plane motions, which is due to the additive white Gaussian noise. The difference between uncorrected, realigned and DRIFT corrected slices became significant for the slice acquired during motion. Out-of-plane rotations caused a slight but significant increase in the PD of the uncorrected slice in comparison to the motionless baseline ($PD_{diff}=0.9$, $p < 10^{-5}$, for 5 degrees rotation around x; $PD_{diff}=1.0$, $p < 10^{-5}$, for 5 degrees rotation around y). Interestingly, realignment makes the artifact even worse than the uncorrected slice ($PD_{diff}=5.8$, $p < 10^{-5}$, for 5 degrees rotation around x; $PD_{diff}=3.5$ $p < 10^{-5}$, for 5 degrees rotation around y). However, DRIFT completely removes the rotational artifact to a level that there is no significant difference between DRIFT corrected and the motionless baseline slices ($PD_{diff}=0.12$, $p > 0.05$, for 5 degrees rotation around x; $PD_{diff}=0.0$, $p > 0.5$, for 5 degrees rotation around y). For out-of-plane translation, as we predicted there is no significant difference between the translated and steady-state slice in uncorrected data ($PD_{diff}=0.1$, $p > 0.1$). However, realignment again fails to correct for out-of-plane translation ($PD_{diff}=16.2$, $p < 10^{-5}$ compared to the motionless baseline), where the DRIFT corrected slice has no motion artifact ($PD_{diff}=0.1$, $p > 0.1$ compared to the motionless baseline). This is mainly because realignment is a registration-based method that fails drastically for partially contaminated volumes.

As we discussed before, the dominant effect of out-of-plane motion takes place after motion, due to spin history. As shown in Figure 4.8 middle row, for uncorrected data the slice acquired immediately after the rotational and translational motions has a much higher PD compared to the slice where the motion actually took place ($PD_{diff}=12.0$, $p < 10^{-5}$, for 5 degrees rotation around x; $PD_{diff}=9.7$, $p < 10^{-5}$, for 5 degrees rotation around y; $PD_{diff}=14.3$, $p < 10^{-5}$, for 5 mm translation along z). While this is mostly due to misalignment, the PD of the realigned volumes are still significantly higher than the motionless baseline, despite being perfectly realigned ($PD_{diff}=2.9$, $p < 10^{-5}$, for 5 degrees rotation around x; $PD_{diff}=2.8$, $p < 10^{-5}$, for 5 degrees rotation around y; $PD_{diff}=3.5$, $p < 10^{-5}$, for 5 mm translation along z). This is because the spin history artifact contaminates the slice without causing any misalignment, thus making it impossible for a registration-based technique to correct for it. DRIFT also fails to correct for out-of-plane motion once that spin history artifact contaminates the slice. As shown in Figure 4.8, the PD of the DRIFT corrected slice acquired after motion is significantly higher than the one acquired during motion ($PD_{diff}=12.5$, $p < 10^{-5}$, for 5 degrees rotation around x; $PD_{diff}=10.6$, $p < 10^{-5}$, for 5 degrees rotation around y axis; $PD_{diff}=14.3$, $p < 10^{-}$

^{5}, for 5 mm translation along z), suggesting that correcting for spin-history artifacts is extremely challenging if not impossible.

While correcting for spin-history artifacts seems to be a challenge, preventing it with slice-based prospective motion correction methods has already been proposed and implemented in the field. In the next two simulations, we aim to show that the combination of prospective motion correction and DRIFT, as a retrospective method, can optimally remove the motion artifacts from the fMRI data. By changing the motion profile and applying a quick inverse motion immediately after acquisition of the slice (and before applying next RF pulse), we aim to simulate our proposed hybrid motion correction technique. As shown in Figure 4.8, a 5 degree out of plane rotation around y again has a slight but significant effect on the PD of the slice where the motion took place in comparison to the motionless baseline ($PD_{diff}=1.0$, $p < 10^{-5}$, for uncorrected; $PD_{diff}=0.8$, $p < 10^{-5}$, for realignment), which is optimally corrected with DRIFT ($PD_{diff} < 0.1$, $p > 0.1$). For a 5 mm out-of-plane translation, no significant change has been observed in all fMRI data, if spin-history artifact has been prevented ($PD_{diff} < 0.1$, $p > 0.5$), essentially validating out findings in equation (4.7).

The bottom row in Figure 4.8 plots the computed PD for slice number 4 in all 20 simulated volumes with out-of-plane motion. Again, all simulated cases and correction methods reach their steady-state by volume 5. The dots on the curve show the mean of the PD and the shaded band around each curve illustrate the 95% confidence interval at each point of computation. The first three graphs represent motion with spin-history effects. For rotation around x, rotation around y, and translation along z, there is an abrupt increase in PD for the realigned slice at volume 10 (the volume in which motion occurs). However, we see only a small increase in PD for uncorrected data, and no increase in PD for DRIFT at volume 10. In volume 11, we now see a large increase in PD for both DRIFT and uncorrected data. At this point, we also see that the PD for realigned data has decreased slightly from volume 10. Over the next few volumes, the PD in all three data sets will gradually decrease until leveling out at a new baseline around volume 13. This gradual decrease is due to spin-history, and represents the system slowly returning to steady-state. The final two graphs repeat two of these motions, (5 degree rotation around y and 5mm translation along z)

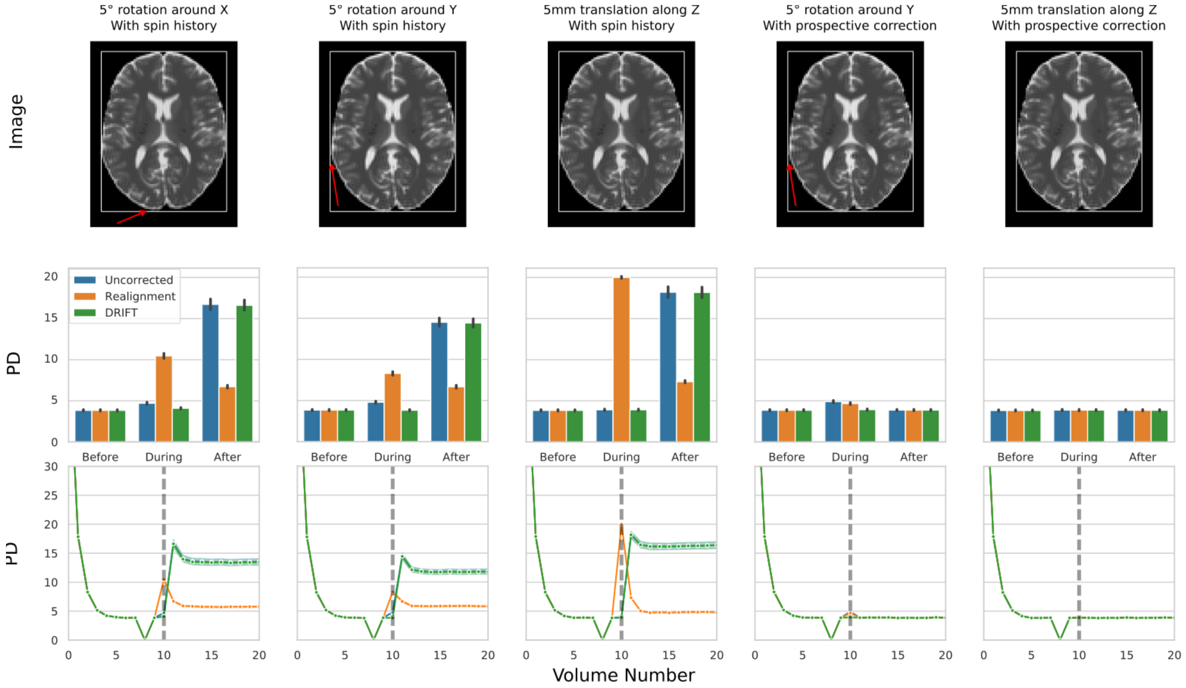

Figure 4.8: Artifacts and PD for out-of-plane motion, in simulated data.

(top) Illustration of the artifacts that occur for different types of out-of-plane motion. (middle) PD calculated for the slice in which motion occurs for the volume before, during, and after motion. (bottom) time-series of the PD calculated for the slice in which motion occurs for the entire simulation. Volumes 9, 10, and 11 correspond to the before, during, and after volumes in the middle row.

while preventing spin-history artifacts. In these simulations, there is no difference in the PD before and after motion for all correction methods, indicating a perfect removal of motion artifacts.

4.4.3 DRIFT Performance Using Real-Subject Motion Parameters

Up to this point, all simulations were based on synthesized motion profiles which were exaggerated and performed mainly for the purpose of studying and differentiating the distinct effect each type of motion has on the data. In this experiment, we extracted motion parameters from a real subject's typical fMRI scanning session and used it to simulate the effect of realistic motion on fMRI data. We used volume 5 as the reference volume where the fMRI signal reaches its steady-state equilibrium and computed volume-based PD to investigate the effect of realistic in-plane motion and evaluate the performance of our proposed motion correction technique. Figure 4.9 shows the results of this experiment. The three dotted black curves depict the in-plane motion parameters (rotation around z axis, transformation along x and y axes), and the solid black line indicates the total displacement due to the motion parameters. The blue solid line indicates the PD computed for uncorrected fMRI volumes, and the orange and green curves shown the PD for realigned and DRIFT corrected volumes. The insert illustrates a magnified sections of the plots where there is minimal movement in the target object. The shaded border with the same color indicates the 95% confidence interval at each volume.

At each time point, the realigned data had significantly lower PD compared to the uncorrected data (Average PD_{diff}=5.2, $p < 10^{-5}$ at each timepoint). Likewise, at every time point, DRIFT had an even lower PD than realignment. (Average PD_{diff} = 0.8, $p < 10^{-5}$ at each timepoint). Further, DRIFT performs much more consistently than realignment, as the variance of the PD over all volumes was 0.0008 for DRIFT, and 0.1744 for realignment. The insert to the right of Figure 4.9 contains a scatter plot of PD and displacement for uncorrected, realigned and Drift corrected volumes, with the slopes indicated as beta values. While displacement is associated strongly with the magnitude of the motion artifact in the uncorrected data, this

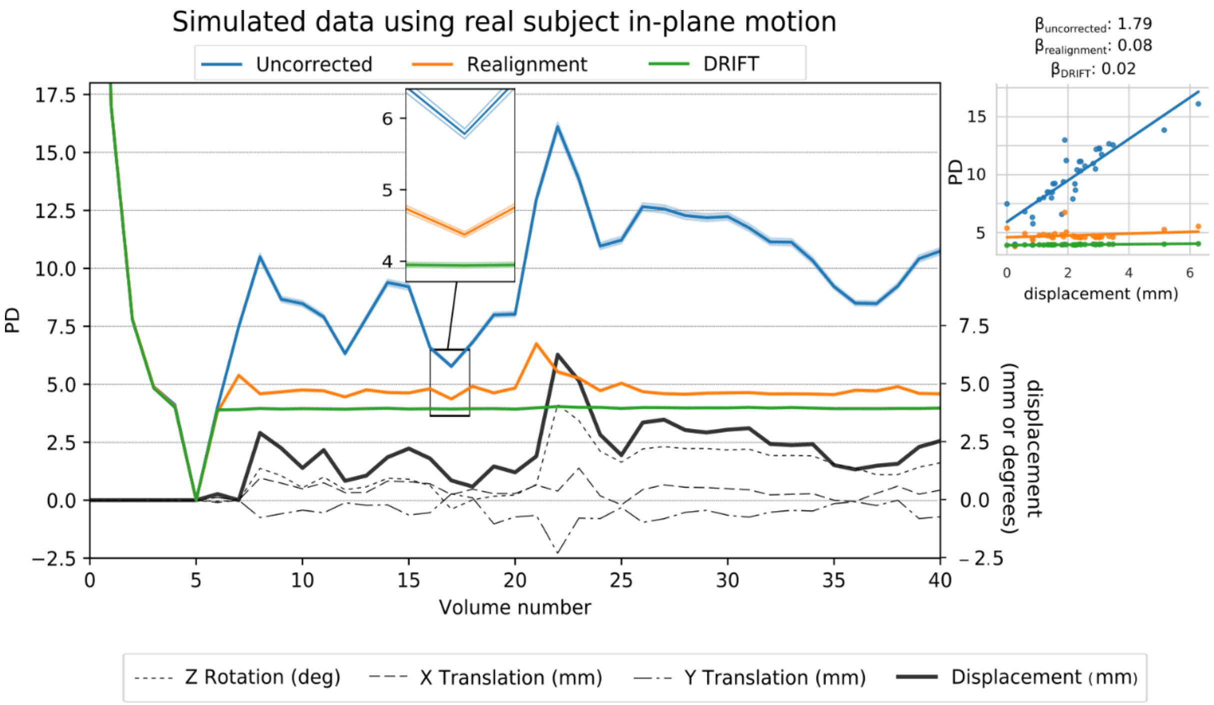

Figure 4.9: DRIFT correction on simulated data with real subject motion. Volume-wise absolute percent difference from baseline of 41 volume simulation with real subject in-plane rotation and translation for uncorrected, realigned, and DRIFT corrected data. Black dashed lines indicate the level of rotation, translation, and the solid line represents total displacement. Center inset shows an enlarged view of the 95% confidence intervals for the volume where uncorrected, realigned, and DRIFT have the smallest difference. Right inset shows the regression of framewise displacement to PD. Slopes are shown above as beta values.

association weakens by applying realignment to the fMRI data, and is completely removed using DRIFT, verifying the effectiveness of the DRIFT in removing realistic in-plane motion.

4.4.4 Evaluating DRIFT Using a Rotating Phantom

In our final experiment, we present the results of our rotating phantom inside the scanner as the proof of concept that DRIFT can potentially be used to attenuate motion artifacts during a real fMRI data acquisition. The top row of Figure 4.10 shows the reconstructed images using the in-house developed reconstruction pipeline for motionless, rotated, realigned, and DRIFT corrected slice, respectively. The bottom row of Figure 4.10 plots the mutual information computed between the reference volume and all other volumes acquired throughout the one minute scan for uncorrected (in blue), realigned (in orange) and DRIFT corrected (in green) slices. As demonstrated in this figure, while there is some fluctuation in the computed mutual information for the first 10 slices, the three different reconstructions produced identical mutual information at a mean value equal to 1.82, which provides the maximum possible mutual information for this data, given the level of noise present. Once the phantom starts moving, a higher mutual information indicates better removal of motion artifacts. Throughout the 40 second moving period, realigned images had higher mutual information than uncorrected images in 81% of the timepoints. DRIFT-corrected slices had in the highest mutual information for 100% of the volumes compared to uncorrected data, and in 90% of the volumes compared to realigned data. During the last 10 seconds of motionless scaning, there are differences between the reconstructed, realigned, and DRIFT corrected slices, which is due to the random orientation of the phantom when it stops moving. Finally, the box plot Figure 4.10 illustrates the significant differences between average mutual information obtained from the uncorrected (in blue), realigned (in orange) and DRIFT-corrected (in green) slices using bar-plots. For all but the initial 10 volumes, realignment significantly increased the mutual information by an average of 0.11 over the uncorrected data ($p < 10^{-5}$). DRIFT-corrected slices also significantly increased the mutual information by an average of 0.15 over the uncorrected data ($p < 10^{-5}$), and 0.04 over the realigned data ($p < 10^{-5}$). Given that the lowest mutual

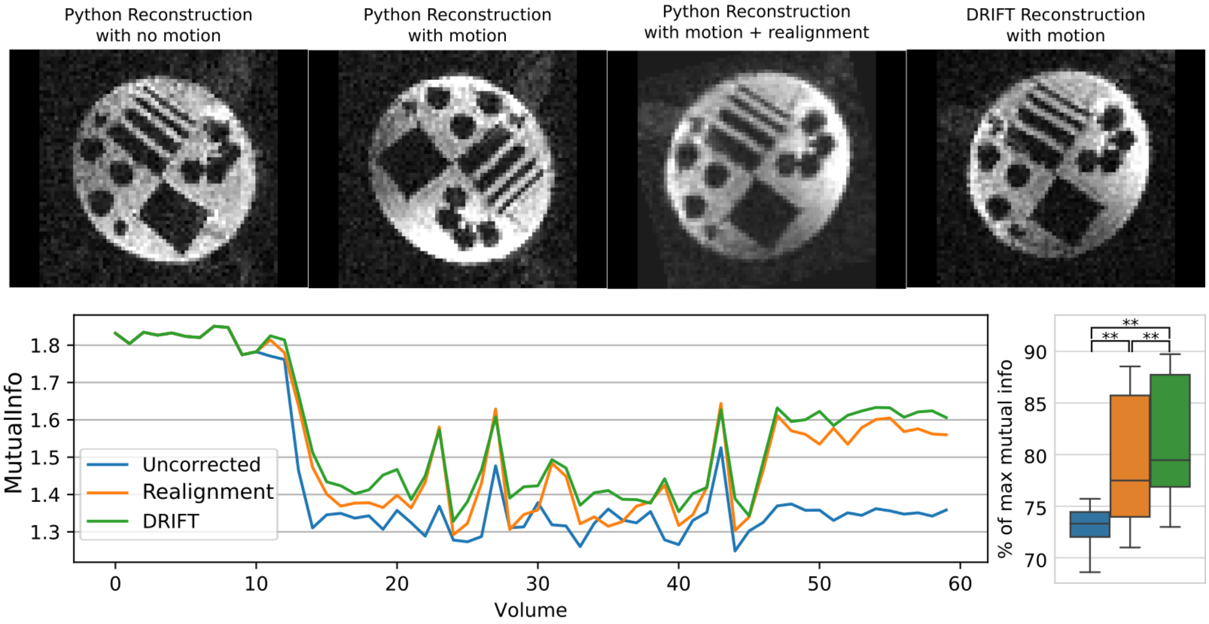

Figure 4.10: Mutual information of uncorrected, realigned, and DRIFT corrected images in real data
(Top) From left to right: 1: An example of a python reconstructed slice without motion. 2: A rotating slice reconstructed with python. 3: The same rotated slice, corrected with realignment. 4: The same rotated slice, corrected with DRIFT. (Bottom) The mutual information between each volume of real data to the reference volume. The reference volume is created by averaging the first 10 motionless volumes of the scan in the uncorrected dataset.

information for any method was 1.25, and the ceiling was 1.82, the total range of the mutual information was only 0.57. The increase in mutual information due to drift DRIFT compared to uncorrected data is 26% of the possible mutual information range, while the increase between DRIFT and realigned data is 7% of the possible range. Together, these results show the superiority of DRIFT in real fMRI scanning to correct for motion contamination during slice acquisition.

In this data set, the improvement of drift is hard to see on an individual volume, due to the small nature of the artifact as well as the presence of other noise sources. However, taking a temporal average of all motion contaminated volumes reveals subtle differences between DRIFT corrected volumes and realigned volumes. These averaged volumes are shown in Figure 4.11. Visually, the DRIFT reconstructed data showed higher contrast and sharper edges, as compared to traditional realignment which generated blurred edges and lower contrast. These “blurred” edges are not an artifact of smoothing, nor are they the result of improper motion estimates – DRIFT and realignment used identical motion parameters for correction. These misalignments are subtle distortions present due to uneven k-space sampling, much like the distortions seen around the edges of simulated data in Figure 4.7. DRIFT is able to remove many of these artifacts, improving the contrast and reconstructing a more accurate image.

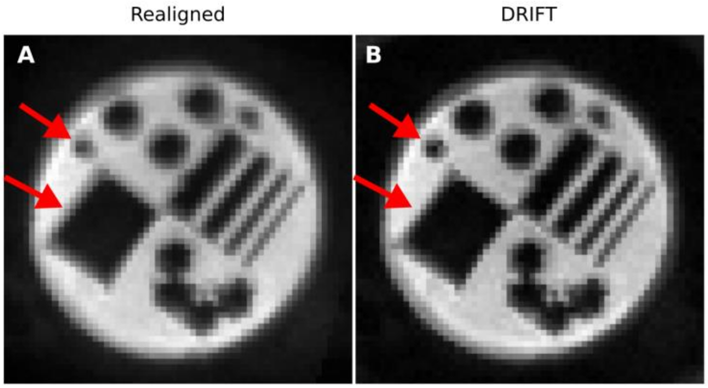

Figure 4.11: Comparison of time-averaged volumes from corrected scans for realigned data, Drift-corrected data with smoothing, and DRIFT-corrected data without smoothing

The 50 motion contaminated scans from the real data are corrected using either realignment or DRIFT. These volumes are then averaged over time. DRIFT corrected data has noticeably sharper edges. Identical motion parameters were used to correct for motion in DRIFT and realigned data, meaning that the blurring on realigned data is not just due to a poor motion parameter estimate. The sharpness of the DRIFT corrected image is due to the removal of motion artifacts throughout the scan. Removing the smoothing step enhances the

4.5 Discussion

In this chapter, we demonstrated the theoretical and practical validity of removing nearly all motion artifacts from fMRI scans. We separately examined common motion found in a typical fMRI scan to investigate reconstruction artifacts which were motion-type specific. We performed a theoretical formulation of the effect of each type of motion using the principles of MR signal generation and the Bloch equations. Next, using the simulated data, we demonstrated the validity of our theoretical findings. Based on our formulation and simulation findings, we argued that neither prospective nor retrospective motion correction methods can completely remove the motion artifacts. Therefore, using a hybrid motion correction method seems to be unavoidable. We then proposed a retrospective method that in combination with the existing slice-based prospective motion correction method, could potentially remove the remaining motion artifacts completely. Using the simulated data we demonstrated clear and substantial improvements in image reconstruction using our proposed retrospective method over other common motion correction routines.

4.5.1 *In-Plane Motion Simulation*

For all in-plane motion profiles, DRIFT completely removed all motion artifacts from the image. For in-plane rotation around the z axis, the motion artifacts are due to a k-space sampling offset similar to that of Figure 4.2 (c). Realignment is unable to correct for these artifacts, and only adjusts for any apparent misalignment. Surprisingly, in-plane rotation was not the most destructive form of in-plane motion. Translation along both x and y generated a larger PD measure than rotation around z, even though translation only disrupts the phase of the signal, and preserves the k-space trajectory.

The combination of motion profiles (y translation with z rotation, and x translation with y translation) increased the level of motion artifact, but not additively. For example, the PD for translation along x during motion was 14.7 for uncorrected data, while the PD for translation along y was 13.8. However, the combination of both x and y translation only increased the PD to 17.0, implying that the errors do not simply add on top of each other, but rather have some form of interaction. This held true for the rotation and translation motion combination as well.

4.5.2 *Out-of-Plane Motion Simulation*

For out-of-plane rotation, while it was expected that it would have less error than in-plane rotation, what was surprising was how the out-of-plane rotation artifact was visually nothing like the in-plane rotation artifact. Instead, a rotation around the y axis looked like a slight compression of the image along the x axis, while a rotation around the x axis resembled a slight compression of the image along the y axis. This agrees with a qualitative analysis of out-of-plane rotation, which can show that the gradients experienced by the object become compressed spatially during the rotation.

In general, in-plane motion has a higher PD in the “during motion” scan, but after motion these artifacts can be optimally removed through prospective motion correction, DRIFT, or to a lesser degree, realignment. Conversely, out-of-plane motion has relatively low PD in the “during motion” scan, but has lasting spin-history artifacts in the multiple volumes after motion that cannot easily be corrected for by any method, and so the uncorrupted signal is not recoverable. In the volumes after motion, DRIFT fails to correct for motion completely. Realignment is able to perfectly align the rotated volume with the reference, however spin-history artifacts are still present and are responsible for most of the PD in these volumes. This highlights that spin-history artifacts are an entirely different kind of artifact, unrelated to misalignment or k-space readout. Because of this, spin-history artifacts are extremely challenging if not impossible to correct for. Given these observations, spin-history artifacts should still be considered as more harmful than in-plane motion artifacts. This strengthens the argument that fMRI needs slice-based prospective motion correction to successfully address the motion problem.

Interestingly, realignment increased the PD for the “during motion” volume contaminated with out-of-plane motion. In theory, and depending on the difference measure being evaluated, realignment software should never result in a higher percent difference than uncorrected, as it runs a cost-function minimization routine. If all attempted orientations result in a larger error than the original position, no realignment will be done, and the error should be at most equivalent to uncorrected data. In our reconstructions, the realignment software was given the true motion parameters rather than allowing it to estimate the motion itself. This means that correcting for the true motion does not consistently reduce image differences when motion occurs across slices within a single volume. Because of this, difference minimizing cost functions may provide very unreliable motion estimates for volumes with high motion. This highlights the harmful effects of intra-volume motion and slice misalignment.

Out-of-plane translation and rotation *without* spin-history artifacts proved to be the least destructive of all motion types in our simulations. The simulation of out-of-plane translation is a critical piece of evidence for our motion correction method. It effectively demonstrates that out-of-plane translation only causes artifacts if it causes the following slices to be over or under-excited. prospective motion correction is already demonstrated to be accurate to around 0.3mm with optical and navigator tracking [54], [76], [91], and has shown great promise in its ability to compensate for motion on a slice by slice basis [76], [92]. Thus, with proper prospective motion correction, no additional motion correction of any kind would be necessary for out-of-plane translation.

4.5.3 Simulation With Real Subject Motion

For the previous 10 simulated scans used to demonstrate the different types of in-plane and out-of-plane motion artifacts in Figure 4.7 and Figure 4.8, the motion occurred entirely over one slice acquisition (two TE’s). The motion we used consisted of either 5mm translations or 5 degree rotations, which occurred along various axes. While it is rare for a subject to move 5 degrees or 5mm within a period of two TE's, in real fMRI scanning, this level of motion does fall well within physiologically possible ranges. Nonetheless, we were also able to show the superiority of our method on a simulated scan using a real subject's motion profile. In this particular simulation, not only was the motion taken from a real subject, but also it was simulated to happen gradually over the entire TR, not just during the readout of a single slice. DRIFT was still able to significantly improve the reconstruction in this realistic simulation.

The simulation with the subject's real motion parameters has smaller translations and rotations than the other 10 simulations, however it has the largest uncorrected error with a peak value of 16.1%, which is higher than any of the exaggerated motion errors. There are multiple explanations for this: first, although the relative volume-to-volume displacements are smaller than 5 degrees or 5mm, over the course of the simulation, the absolute displacement relative to the reference volume accumulates up to a total of 4.1 degrees of rotation and 2.3 mm of total translation at volume 22. Second, we demonstrated in the other simulations that the combination of motions is the more destructive than each motion individually. This simulation has three motion types occurring simultaneously: z rotation, x translation, and y translation, while our simulated data only ever had two motion types occurring simultaneously. Finally, this PD is calculated over the entire volume, rather than just a slice. This increases the number of high-contrast edges that contribute to large PDs.

4.5.4 Real Data Correction

For real data, we were able to show the benefit of DRIFT when added to the raw data processing pipeline. While the benefit may seem small, this experiment could be drastically improved to further enhance DRIFT. Primarily, exact sub-TR motion tracking was not available for this scan. If the motion is not accurately measured, this will cause additional errors in DRIFT's k-space mapping calculations. For this study, we took the relative deflection of the phantom between two volumes and estimated k-space rotations assuming constant rotation. In reality, it is possible the rotation experienced acceleration or deceleration during the TR. Further, DRIFT works best when working directly with the gradient profiles in the exact pulse sequence, as with POSSUM's simulated data, or at the very least a full k-space trajectory map. Our pipeline estimated a full 128x64 k-space trajectory from a single exemplar read line provided in the raw file header. Without exact knowledge of both the pulse sequence and the motion, we rely on estimating both of these parameters, which have detrimental effects on the results. Finally, the Siemen's raw data processing pipeline consists of approximately 20 to 30 signal processing steps, which take advantage of the pulse sequence design, adjustment volume for phase corrections, and several other system-dependent inputs that are used for a more accurate reconstruction. Our pipeline consisted of only 3 main processing steps. Integrating DRIFT into the full system pipeline would maximize its effectiveness.

If DRIFT can be integrated directly into a scanner's system, it can be used with any number of different pulse sequences. One particularly useful area would be 3D EPI. 3D EPI is a technique in which an entire volume is acquired in one RF pulse, and a three dimensional k-space trajectory is traced and sampled. This essentially makes the reconstruction a single 3D FFT rather than multiple 2D FFTs. Using the principles developed in this paper, our reconstruction algorithm could theoretically be applied directly to 3D sampled data, completely eliminating all artifacts during sampling. This would actually eliminate the need for prospective motion correction completely, as DRIFT could also be used to re-orient each volume, providing accurate motion estimates were still being recorded. Future work could involve developing this method for a 3D pulse sequence.

5 Conclusion

5.1 Interleave Detection

The omission of interleave parameters from fMRI data can cause problems for researchers. Even in the absence of motion, many of the preprocessing and statistical analysis steps rely on the assumption that each 3D volume of the 4D fMRI signal is sampled instantaneously. Breaking this assumption will result in a loss of sensitivity and potentially an increase in false negatives when identifying activated brain regions. By using the spatio-temporal properties of the fMRI signal, we developed an algorithm to retrospectively extract the interleave parameter using the temporal distance correlation function. We found that this algorithm was able to successfully extract the interleave parameter on simulated data 100% of the time. For over 1,000 real data scans taken from two separate imaging studies, as well as the fcon_1000 data set (which is collected from 23 separate sites) interleave parameter estimation was accurate for 94% of all scans. This provides researches with a tool to retrospectively extract an interleave parameter for old or shared data where such information may be missing. Without this parameter, the critical preprocessing step of slice timing correction cannot be carried out.

5.2 Optimal Slice Timing Correction

We have demonstrated that STC is a critical step in any preprocessing routine. In the presence of spatial smoothing, alternatives to STC such as slice-dependent regressors will actually perform worse than STC, despite the fact that they prevent the addition of interpolation errors. Upon critically examining the standard STC routines, we have discovered that from a signal processing point of view, they are far from optimal. Even without any motion present, these interpolation schemes do not preserve the frequency domain of the BOLD signal, introducing interpolation error into the signal.

By developing a STC routing based on Shanon-Nyquist sampling theory, and digital signal processing principles, an optimal method was developed. This method employs a computationally efficient algorithm that is equivalent to upsampling, lowpass filtering, and downsampling the original data at an arbitrary shifted offset, which is how it accounts for slice timing. This method performed significantly better than all other methods across various levels of motion, interleave, and TR in simulated data. If motion artifacts can be completely removed, our STC routine can completely correct for the temporal offsets induced by slice-based acquisition.

5.3 Motion Correction

Current strategies that attempt to regress out or remove motion related variance fail to address the motion problem from first principles, and therefor do not successfully model the motion. Motion artifacts are varied and are difficult to describe with just one regressor. Increasing the number of modeled motion effects can alleviate this problem, however this does not address the simple fact that removing motion related variance does not guarantee that the underlying signal is recoverable. Attempting to remove motion artifacts on a reconstructed signal is fundamentally flawed. Motion is not simply an additive noise, as shown through our simulations, and without proper correction, it will destroy the underlying signal. By correcting for motion artifacts in the raw data itself, we have the best likelihood of reconstructing an uncorrupted time-series.

We have developed a novel technique that both corrects for motion while simultaneously reconstructing the data. This method significantly attenuates the motion artifacts on a slice-by-slice basis. By correcting for artifacts in the raw k-space data, we are able to completely remove motion related artifacts and restore the original signal if the steady-state is not disturbed. We demonstrated in both real and simulated data that DRIFT lowers the error between motion contaminated volumes and the reference volume, indicating a better motion correction. This was tested and verified over a variety common motion profiles in fMRI. To extend the application beyond theory and simulation, a real fMRI scan was acquired and corrected with our method. DRIFT’s advantage over other motion correction methods is the fact that it corrects for motion in the raw data reconstruction itself. Not only does this eliminate the need for interpolation based motion correction in the reconstructed scan, but also, when combined with modern prospective motion correction, DRIFT could potentially eliminate all motion artifacts from fMRI scans.

5.4 Application & Future Work

Given the prior state of STC and MC routines commonly used in fMRI preprocessing, a significant number of artifacts remain in the data even after correction. Some of these artifacts are due to an incomplete model of the problem (e.g. not studying and modeling the effects of k-space distortion for different types of motion), while others are due to complicated interactions between the spatio-temporal components of the signal (e.g. the interaction of STC and MC). By critically examining these components separately, it became clear that motion must be corrected before any other preprocessing step can be carried out. Additionally, current MC routines are incapable of removing all motion related artifacts. DRIFT, combined with prospective motion correction and our STC routine, provides the cleanest possible fMRI signal in both temporal and spatial alignment, providing a fundamentally sound starting point for the rest of the preprocessing pipeline. Additionally, the removal of motion artifacts will increase the number of usable scans by up to 25% in some populations. This is an extremely significant number for most fMRI studies, and can be the difference between discovering or missing group level findings.

In the current state of these methods, STC is implemented as a standalone program in C++. Using the fast implementation described in this thesis, execution of this method takes less than a minute for the average fMRI scan. For future work, this method will be packaged with any future preprocessing methods developed by our lab, and available for use among researchers.

DRIFT is at an earlier stage of development, and has only been tested using simulation and the most basic reconstruction of real data. Operating outside of the scanner, many of the inputs for DRIFT are estimated or based off a template, rather than calculated from a known ground truth. Integrating DRIFT directly into the scanner’s reconstruction pipeline could greatly increase its effectiveness, however the optimal location in the pipeline would have to be determined, and it’s likely that numerous steps would have to be redesigned to accommodate DRIFT. For example, in many scanner reconstructions, an IFFT is performed along the x and y axis separately, with additional processing taking place in-between. It is not clear if this can be implemented with DRIFT without knowing the details of the intermediate processing steps. Additionally, it’s currently a computationally intensive correction method, taking over an hour to reconstruct 60 slices. Optimization of the algorithm could be implemented using a number of strategies, from lookup tables to parallel processing support. Finally, while motion was estimated manually in this experiment, a motion tracking method with both high spatial and temporal resolution would greatly benefit DRIFT, as it could provide more accurate measurements while significantly lightening the user burden. Thus, the future direction for DRIFT involves reducing the computation time, implementing the reconstruction into a commercial pipeline, and capturing 3D external motion measurements to use as inputs to the algorithm. We believe that these developments, alongside prospective motion correction, could reduce the vast majority of motion artifacts in fMRI, resulting in a cleaner and more reliable signal.

Bibliography

[1] L. Pauling and C. D. Coryell, "The Magnetic Properties and Structure of Hemoglobin, Oxyhemoglobin and Carbonmonoxyhemoglobin.," *Proc. Natl. Acad. Sci. U. S. A.*, vol. 22, no. 4, pp. 210–6, Apr. 1936.

[2] S. Ogawa, T. M. Lee, A. S. Nayak, and P. Glynn, "Oxygenation-sensitive contrast in magnetic resonance image of rodent brain at high magnetic fields.," *Magn. Reson. Med.*, vol. 14, no. 1, pp. 68–78, Apr. 1990.

[3] S. A. Huettel, A. W. Song, G. McCarthy, and others, *Functional magnetic resonance imaging*, vol. 1. Sinauer Associates Sunderland, MA, 2004.

[4] R. Valabrègue, A. Aubert, J. Burger, J. Bittoun, and R. Costalat, "Relation between Cerebral Blood Flow and Metabolism Explained by a Model of Oxygen Exchange," *J. Cereb. Blood Flow Metab.*, vol. 23, no. 5, pp. 536–545, May 2003.

[5] P. G. Haydon and G. Carmignoto, "Astrocyte Control of Synaptic Transmission and Neurovascular Coupling," *Physiol. Rev.*, vol. 86, no. 3, pp. 1009–1031, Jul. 2006.

[6] R. B. Buxton and L. R. Frank, "A Model for the Coupling between Cerebral Blood Flow and Oxygen Metabolism during Neural Stimulation," *J. Cereb. Blood Flow Metab.*, vol. 17, no. 1, pp. 64–72, Jan. 1997.

[7] D. Attwell and C. Iadecola, "The neural basis of functional brain imaging signals," *Trends Neurosci.*, vol. 25, no. 12, pp. 621–625, Dec. 2002.

[8] G. Wu, F. Luo, Z. Li, X. Zhao, and S.-J. Li, "Transient relationships among BOLD, CBV, and CBF changes in rat brain as detected by functional MRI," *Magn. Reson. Med.*, vol. 48, no. 6, pp. 987–993, Dec. 2002.

[9] T. Kato, A. Kamei, S. Takashima, and T. Ozaki, "Human Visual Cortical Function during Photic Stimulation Monitoring by Means of near-Infrared Spectroscopy," *J. Cereb. Blood Flow Metab.*, vol. 13, no. 3, pp. 516–520, May 1993.

[10] P. T. Fox, M. E. Raichle, M. A. Mintun, and C. Dence, "Nonoxidative glucose consumption during focal physiologic neural activity," *Science (80-.).*, vol. 241, no. 4864, pp. 462–464, 1988.

[11] N. K. Logothetis, "What we can do and what we cannot do with fMRI," *Nature*, vol. 453, no. 7197, pp. 869–878, Jun. 2008.

[12] A. Ekstrom, "How and when the fMRI BOLD signal relates to underlying neural activity: The danger in dissociation," *Brain Res. Rev.*, vol. 62, no. 2, pp. 233–244, Mar. 2010.

[13] M. T. Lippert, T. Steudel, F. Ohl, N. K. Logothetis, and C. Kayser, "Coupling of neural activity and fMRI-BOLD in the motion area MT," *Magn. Reson. Imaging*, vol. 28, no. 8, pp. 1087–1094, Oct. 2010.

[14] A. C. Silva, E. L. Barbier, I. J. Lowe, and A. P. Koretsky, "Radial Echo-Planar Imaging," *J. Magn. Reson.*, vol. 135, no. 1, pp. 242–247, Nov. 1998.

[15] J. I. Jackson, C. H. Meyer, D. G. Nishimura, and A. Macovski, "Selection of a convolution function for Fourier inversion using gridding (computerised tomography application)," *IEEE Trans. Med. Imaging*, vol. 10, no. 3, pp. 473–478, 1991.

[16] P. J. Beatty, D. G. Nishimura, and J. M. Pauly, “Rapid gridding reconstruction with a minimal oversampling ratio,” *IEEE Trans. Med. Imaging*, vol. 24, no. 6, pp. 799–808, Jun. 2005.

[17] D. Parker, G. Rotival, A. Laine, and Q. R. Razlighi, “RETROSPECTIVE DETECTION OF INTERLEAVED SLICE ACQUISITION PARAMETERS FROM FMRI DATA,” *ISBI*, 2014.

[18] B. B. Biswal *et al.*, “Toward discovery science of human brain function.,” *Proc. Natl. Acad. Sci. U. S. A.*, vol. 107, no. 10, pp. 4734–9, Mar. 2010.

[19] J. D. Power, K. A. Barnes, A. Z. Snyder, B. L. Schlaggar, and S. E. Petersen, “Spurious but systematic correlations in functional connectivity MRI networks arise from subject motion,” *Neuroimage*, vol. 59, no. 3, pp. 2142–2154, Feb. 2012.

[20] J. V. Hajnal, R. Myers, A. Oatridge, J. E. Schwieso, I. R. Young, and G. M. Bydder, “Artifacts due to stimulus correlated motion in functional imaging of the brain,” *Magn. Reson. Med.*, vol. 31, no. 3, pp. 283–291, Mar. 1994.

[21] A. S. Field, Y. F. Yen, J. H. Burdette, and A. D. Elster, “False cerebral activation on BOLD functional MR images: study of low-amplitude motion weakly correlated to stimulus.,” *AJNR. Am. J. Neuroradiol.*, vol. 21, no. 8, pp. 1388–96, Sep. 2000.

[22] R. W. Cox, “AFNI: Software for Analysis and Visualization of Functional Magnetic Resonance Neuroimages,” *Comput. Biomed. Res.*, vol. 29, no. 3, pp. 162–173, Jun. 1996.

[23] J. D. Power, M. Plitt, P. Kundu, P. A. Bandettini, and A. Martin, “Temporal interpolation alters motion in fMRI scans: Magnitudes and consequences for artifact detection,” *PLoS One*, vol. 12, no. 9, p. e0182939, Sep. 2017.

[24] A. Kaushik *et al.*, “Estimation of radiation dose to patients from 18FDG whole body PET/CT investigations using dynamic PET scan protocol,” *Indian J. Med. Res.*, vol. 142, no. 6, p. 721, Dec. 2015.

[25] C. M. Collins *et al.*, “Temperature and SAR calculations for a human head within volume and surface coils at 64 and 300 MHz,” *J. Magn. Reson. Imaging*, vol. 19, no. 5, pp. 650–656, May 2004.

[26] J. T. Vaughan *et al.*, “7T vs. 4T: RF power, homogeneity, and signal-to-noise comparison in head images,” *Magn. Reson. Med.*, vol. 46, no. 1, pp. 24–30, Jul. 2001.

[27] FDA, “MRI (Magnetic Resonance Imaging) - Benefits and Risks,” 2017.

[28] O. Carmichael *et al.*, “The role of fMRI in drug development,” *Drug Discov. Today*, vol. 23, no. 2, pp. 333–348, Feb. 2018.

[29] N. Jaworska, X.-R. Yang, V. Knott, and G. MacQueen, “A review of fMRI studies during visual emotive processing in major depressive disorder,” *World J. Biol. Psychiatry*, vol. 16, no. 7, pp. 448–471, Oct. 2015.

[30] H. Macpherson, M. Formica, E. Harris, and R. M. Daly, “Brain functional alterations in Type 2 Diabetes – A systematic review of fMRI studies,” *Front. Neuroendocrinol.*, vol. 47, pp. 34–46, Oct. 2017.

[31] H. Khazaie *et al.*, “Functional reorganization in obstructive sleep apnoea and insomnia: A systematic review of the resting-state fMRI,” *Neurosci. Biobehav. Rev.*, vol. 77, pp. 219–231, Jun. 2017.

[32] D. P. Terry, D. Sabatinelli, A. N. Puente, N. A. Lazar, and L. S. Miller, “A Meta-Analysis of fMRI

Activation Differences during Episodic Memory in Alzheimer's Disease and Mild Cognitive Impairment," *J. Neuroimaging*, vol. 25, no. 6, pp. 849–860, Nov. 2015.

[33] H.-J. Li, X.-H. Hou, H.-H. Liu, C.-L. Yue, Y. He, and X.-N. Zuo, "Toward systems neuroscience in mild cognitive impairment and Alzheimer's disease: A meta-analysis of 75 fMRI studies," *Hum. Brain Mapp.*, vol. 36, no. 3, pp. 1217–1232, Mar. 2015.

[34] J. V. Hull, L. B. Dokovna, Z. J. Jacokes, C. M. Torgerson, A. Irimia, and J. D. Van Horn, "Resting-State Functional Connectivity in Autism Spectrum Disorders: A Review," *Front. Psychiatry*, vol. 7, p. 205, Jan. 2017.

[35] M. Tahmasian *et al.*, "A systematic review on the applications of resting-state fMRI in Parkinson's disease: Does dopamine replacement therapy play a role?," *Cortex*, vol. 73, pp. 80–105, Dec. 2015.

[36] D. C. Van Essen, S. M. Smith, D. M. Barch, T. E. J. Behrens, E. Yacoub, and K. Ugurbil, "The WU-Minn Human Connectome Project: An overview," *Neuroimage*, vol. 80, pp. 62–79, 2013.

[37] P. M. Matthews and A. Hampshire, "Clinical Concepts Emerging from fMRI Functional Connectomics," *Neuron*, vol. 91, no. 3, pp. 511–528, Aug. 2016.

[38] R. M. Birn *et al.*, "The effect of scan length on the reliability of resting-state fMRI connectivity estimates," *Neuroimage*, vol. 83, pp. 550–558, Dec. 2013.

[39] R. Sladky, K. J. Friston, J. Tröstl, R. Cunnington, E. Moser, and C. Windischberger, "Slice-timing effects and their correction in functional MRI," *Neuroimage*, vol. 58, no. 2, pp. 588–594, Sep. 2011.

[40] R. Henson, C. Buechel, O. Josephs, and K. Friston, "The slice-timing problem in event-related fMRI," *Neuroimage*, 1999.

[41] K. Vogt, J. Ibinson, R. Small, and P. Schmalbrock, "Slice-timing correction affects functional MRI noise, model fit, activation maps, and physiologic noise correction," in *Proceedings 17th Scientific Meeting, International Society for Magnetic Resonance in Medicine*, 2009, vol. Honolulu, p. 3679.

[42] K. J. Friston, A. P. Holmes, K. J. Worsley, J.-P. Poline, C. D. Frith, and R. S. J. Frackowiak, "Statistical parametric maps in functional imaging: A general linear approach," *Hum. Brain Mapp.*, vol. 2, no. 4, pp. 189–210, Jan. 1994.

[43] M. Jenkinson, C. F. Beckmann, T. E. J. Behrens, M. W. Woolrich, and S. M. Smith, "FSL," *Neuroimage*, vol. 62, no. 2, pp. 782–790, Aug. 2012.

[44] B. Fischl *et al.*, "Whole Brain Segmentation: Automated Labeling of Neuroanatomical Structures in the Human Brain," *Neuron*, vol. 33, no. 3, pp. 341–355, Jan. 2002.

[45] B. Fischl *et al.*, "Sequence-independent segmentation of magnetic resonance images," *Neuroimage*, vol. 23, Supple, pp. S69–S84, 2004.

[46] D. N. Greve and B. Fischl, "Accurate and robust brain image alignment using boundary-based registration," *Neuroimage*, vol. 48, no. 1, pp. 63–72, Oct. 2009.

[47] M. Jenkinson, P. Bannister, M. Brady, and S. Smith, "Improved Optimization for the Robust and Accurate Linear Registration and Motion Correction of Brain Images," *Neuroimage*, vol. 17, no. 2, pp. 825–841, Oct. 2002.

[48] K. J. Friston *et al.*, "Analysis of fMRI time-series revisited.," *NeuroImage*, vol. 2, no. 1. pp. 45–53, Mar-1995.

[49] B. Kim, J. L. Boes, P. H. Bland, T. L. Chenevert, and C. R. Meyer, “Motion correction in fMRI via registration of individual slices into an anatomical volume,” *Magn. Reson. Med.*, vol. 41, no. 5, pp. 964–972, 1999.

[50] C. F. Beckmann, M. Jenkinson, and S. M. Smith, “General multilevel linear modeling for group analysis in FMRI,” *Neuroimage*, vol. 20, no. 2, pp. 1052–1063, Oct. 2003.

[51] M. W. Woolrich, T. E. J. Behrens, C. F. Beckmann, M. Jenkinson, and S. M. Smith, “Multilevel linear modelling for FMRI group analysis using Bayesian inference,” *Neuroimage*, vol. 21, no. 4, pp. 1732–1747, Apr. 2004.

[52] R. A. Poldrack, J. A. Mumford, and T. E. Nichols, *Handbook of functional MRI data analysis*. Cambridge University Press, 2011.

[53] V. Calhoun, X. Golay, and G. Pearlson, “Improved fMRI slice timing correction: interpolation errors and wrap around effects,” *Proceedings, ISMRM, 9th Annu. Meet. Denver*, p. 810, 2000.

[54] N. White *et al.*, “PROMO: Real-time prospective motion correction in MRI using image-based tracking,” *Magn. Reson. Med.*, vol. 63, no. 1, pp. 91–105, Jan. 2010.

[55] M. Zaitsev, J. Maclaren, and M. Herbst, “Motion artifacts in MRI: A complex problem with many partial solutions,” *J. Magn. Reson. Imaging*, vol. 42, no. 4, pp. 887–901, Oct. 2015.

[56] R. Bhagalia and B. Kim, “Spin saturation artifact correction using slice-to-volume registration motion estimates for fMRI time series,” *Med. Phys.*, vol. 35, no. 2, pp. 424–434, Jan. 2008.

[57] W. Chunli, D. Zhibing, Y. Kun, and W. Yun, “An improved algorithm of translational motion artifact correction for MRI,” in *The 27th Chinese Control and Decision Conference (2015 CCDC)*, 2015, pp. 4054–4057.

[58] B. Zahneisen, B. Keating, A. Singh, M. Herbst, and T. Ernst, “Reverse retrospective motion correction,” *Magn. Reson. Med.*, vol. 75, no. 6, pp. 2341–2349, Jun. 2016.

[59] T. Johnstone *et al.*, “Motion correction and the use of motion covariates in multiple-subject fMRI analysis,” *Hum. Brain Mapp.*, vol. 27, no. 10, pp. 779–788, Oct. 2006.

[60] M. Hedley, H. Yan, and D. Rosenfeld, “Motion artifact correction in MRI using generalized projections,” *IEEE Trans. Med. Imaging*, vol. 10, no. 1, pp. 40–46, Mar. 1991.

[61] T. R. Oakes *et al.*, “Comparison of fMRI motion correction software tools,” *Neuroimage*, vol. 28, no. 3, pp. 529–543, Nov. 2005.

[62] R. Birn, “An Improved Model of Motion-Related Signal Changes in fMRI,” *Neuroimage*, pp. 3–7, 2016.

[63] J. D. Power, A. Mitra, T. O. Laumann, A. Z. Snyder, B. L. Schlaggar, and S. E. Petersen, “Methods to detect, characterize, and remove motion artifact in resting state fMRI,” *Neuroimage*, vol. 84, pp. 320–341, Jan. 2014.

[64] K. J. Friston, S. Williams, R. Howard, R. S. J. Frackowiak, and R. Turner, “Movement-Related effects in fMRI time-series,” *Magn. Reson. Med.*, vol. 35, no. 3, pp. 346–355, Mar. 1996.

[65] P. R. Bannister, J. Michael Brady, and M. Jenkinson, “Integrating temporal information with a non-rigid method of motion correction for functional magnetic resonance images,” *Image Vis. Comput.*, vol. 25, no. 3, pp. 311–320, Mar. 2007.

[66] H. J. Jo *et al.*, “Effective Preprocessing Procedures Virtually Eliminate Distance-Dependent Motion Artifacts in Resting State FMRI.,” *J. Appl. Math.*, vol. 2013, May 2013.

[67] H. J. Jo, Z. S. Saad, W. K. Simmons, L. A. Milbury, and R. W. Cox, “Mapping sources of correlation in resting state FMRI, with artifact detection and removal,” *Neuroimage*, vol. 52, no. 2, pp. 571–582, Aug. 2010.

[68] L. Griffanti *et al.*, “ICA-based artefact removal and accelerated fMRI acquisition for improved resting state network imaging,” *Neuroimage*, vol. 95, pp. 232–247, Jul. 2014.

[69] P. Kundu, M. D. Santin, P. A. Bandettini, E. T. Bullmore, and A. Petiet, “Differentiating BOLD and non-BOLD signals in fMRI time series from anesthetized rats using multi-echo EPI at 11.7T,” *Neuroimage*, vol. 102, pp. 861–874, Nov. 2014.

[70] P. Kundu, S. J. Inati, J. W. Evans, W.-M. Luh, and P. A. Bandettini, “Differentiating BOLD and non-BOLD signals in fMRI time series using multi-echo EPI,” *Neuroimage*, vol. 60, no. 3, pp. 1759–1770, Apr. 2012.

[71] J. D. Power, B. M. Silver, M. R. Silverman, E. L. Ajodan, D. J. Bos, and R. M. Jones, “Customized head molds reduce motion during resting state fMRI scans,” *Neuroimage*, vol. 189, pp. 141–149, Apr. 2019.

[72] S. E. Yancey *et al.*, “Spin-history artifact during functional MRI: Potential for adaptive correction,” *Med. Phys.*, vol. 38, no. 8, pp. 4634–4646, Jul. 2011.

[73] J. Schulz *et al.*, “Prospective slice-by-slice motion correction reduces false positive activations in fMRI with task-correlated motion,” *Neuroimage*, vol. 84, pp. 124–132, Jan. 2014.

[74] N. Todd, O. Josephs, M. F. Callaghan, A. Lutti, and N. Weiskopf, “Prospective motion correction of 3D echo-planar imaging data for functional MRI using optical tracking,” *Neuroimage*, vol. 113, pp. 1–12, Jun. 2015.

[75] R. Frost *et al.*, “Markerless high-frequency prospective motion correction for neuroanatomical MRI,” *Magn. Reson. Med.*, vol. 82, no. 1, pp. 126–144, Jul. 2019.

[76] O. Speck, J. Hennig, and M. Zaitsev, “Prospective Real-Time Slice-by-Slice Motion Correction for fMRI in Freely Moving Subjects,” *Magn. Reson. Mater. Physics, Biol. Med.*, vol. 19, no. 2, pp. 55–61, May 2006.

[77] S. Thesen, O. Heid, E. Mueller, and L. R. Schad, “Prospective acquisition correction for head motion with image-based tracking for real-time fMRI,” *Magn. Reson. Med.*, vol. 44, no. 3, pp. 457–465, Sep. 2000.

[78] M. D. Tisdall, A. T. Hess, M. Reuter, E. M. Meintjes, B. Fischl, and A. J. W. van der Kouwe, “Volumetric navigators for prospective motion correction and selective reacquisition in neuroanatomical MRI,” *Magn. Reson. Med.*, vol. 68, no. 2, pp. 389–399, Aug. 2012.

[79] J. Maclaren, M. Aksoy, M. B. Ooi, B. Zahneisen, and R. Bammer, “Prospective motion correction using coil-mounted cameras: Cross-calibration considerations,” *Magn. Reson. Med.*, vol. 79, no. 4, pp. 1911–1921, Apr. 2018.

[80] M. Zaitsev, B. Akin, P. LeVan, and B. R. Knowles, “Prospective motion correction in functional MRI,” *Neuroimage*, vol. 154, pp. 33–42, Jul. 2017.

[81] M. Zaitsev, C. Dold, J. Hennig, and O. Speck, “Prospective Real-Time Slice-by-Slice 3D Motion

Correction for EPI Using an External Optical Motion Tracking System," *Proc. Int. Soc. Magn. Reson. Med.*, p. 517, 2004.

[82] I. Drobnjak, D. Gavaghan, E. Süli, J. Pitt-Francis, and M. Jenkinson, "Development of a functional magnetic resonance imaging simulator for modeling realistic rigid-body motion artifacts," *Magn. Reson. Med.*, vol. 56, no. 2, pp. 364–380, Aug. 2006.

[83] I. Drobnjak, G. S. Pell, and M. Jenkinson, "Simulating the effects of time-varying magnetic fields with a realistic simulated scanner," *Magn. Reson. Imaging*, vol. 28, no. 7, pp. 1014–1021, Sep. 2010.

[84] C. Triantafyllou *et al.*, "Comparison of physiological noise at 1.5 T, 3 T and 7 T and optimization of fMRI acquisition parameters," *Neuroimage*, vol. 26, no. 1, pp. 243–250, May 2005.

[85] P. Dragicevic, "Fair Statistical Communication in HCI," Springer, Cham, 2016, pp. 291–330.

[86] L. Friedman, G. H. Glover, D. Krenz, and V. Magnotta, "Reducing inter-scanner variability of activation in a multicenter fMRI study: Role of smoothness equalization," *Neuroimage*, vol. 32, no. 4, pp. 1656–1668, Oct. 2006.

[87] E. C. Caparelli and D. Tomasi, "K-space spatial low-pass filters can increase signal loss artifacts in Echo-Planar Imaging.," *Biomed. Signal Process. Control*, vol. 3, no. 1, pp. 107–114, Jan. 2008.

[88] M. J. Lowe and J. A. Sorenson, "Spatially filtering functional magnetic resonance imaging data," *Magn. Reson. Med.*, vol. 37, no. 5, pp. 723–729, May 1997.

[89] Q. R. Razlighi, J. Steffener, C. Habeck, A. Laine, and Y. Stern, "Resting state inter and intra hemispheric human brain functional connectivity," in *2013 35th Annual International Conference of the IEEE Engineering in Medicine and Biology Society (EMBC)*, 2013, pp. 6522–6525.

[90] C. E. Davey, D. B. Grayden, G. F. Egan, and L. A. Johnston, "Filtering induces correlation in fMRI resting state data," *Neuroimage*, vol. 64, pp. 728–740, Jan. 2013.

[91] C. Dold, M. Zaitsev, O. Speck, E. A. Firle, J. Hennig, and G. Sakas, "Updating of MRI Gradients Using a Infrared Tracking System to Compensate Motion Artifacts."

[92] E. B. Beall and M. J. Lowe, "SimPACE: Generating simulated motion corrupted BOLD data with synthetic-navigated acquisition for the development and evaluation of SLOMOCO: A new, highly effective slicewise motion correction," *Neuroimage*, vol. 101, pp. 21–34, Nov. 2014.

[93] S. J. Clare, "Functional magnetic resonance imaging : methods and applications," University of Nottingham, 1997.

[94] C. Figley, "Improved Methods for Motion-Compensating and Event-Related Spinal Functional Magnetic Resonance Imaging (fMRI)," 2019.

[95] R. Gebker, J. Schwitter, E. Fleck, and E. Nagel, "How We Perform Myocardial Perfusion With Cardiovascular Magnetic Resonance," *J. Cardiovasc. Magn. Reson.*, vol. 9, no. 3, pp. 539–547, May 2007.

Publications & Related Work

First Author:

[1] L. Pauling and C. D. Coryell, “The Magnetic Properties and Structure of Hemoglobin, Oxyhemoglobin and Carbonmonoxyhemoglobin.,” *Proc. Natl. Acad. Sci. U. S. A.*, vol. 22, no. 4, pp. 210–6, Apr. 1936.

[2] S. Ogawa, T. M. Lee, A. S. Nayak, and P. Glynn, “Oxygenation-sensitive contrast in magnetic resonance image of rodent brain at high magnetic fields.,” *Magn. Reson. Med.*, vol. 14, no. 1, pp. 68–78, Apr. 1990.

[3] S. A. Huettel, A. W. Song, G. McCarthy, and others, *Functional magnetic resonance imaging*, vol. 1. Sinauer Associates Sunderland, MA, 2004.

[4] R. Valabrègue, A. Aubert, J. Burger, J. Bittoun, and R. Costalat, “Relation between Cerebral Blood Flow and Metabolism Explained by a Model of Oxygen Exchange,” *J. Cereb. Blood Flow Metab.*, vol. 23, no. 5, pp. 536–545, May 2003.

[5] P. G. Haydon and G. Carmignoto, “Astrocyte Control of Synaptic Transmission and Neurovascular Coupling,” *Physiol. Rev.*, vol. 86, no. 3, pp. 1009–1031, Jul. 2006.

[6] R. B. Buxton and L. R. Frank, “A Model for the Coupling between Cerebral Blood Flow and Oxygen Metabolism during Neural Stimulation,” *J. Cereb. Blood Flow Metab.*, vol. 17, no. 1, pp. 64–72, Jan. 1997.

[7] D. Attwell and C. Iadecola, “The neural basis of functional brain imaging signals,” *Trends Neurosci.*, vol. 25, no. 12, pp. 621–625, Dec. 2002.

[8] G. Wu, F. Luo, Z. Li, X. Zhao, and S.-J. Li, “Transient relationships among BOLD, CBV, and CBF changes in rat brain as detected by functional MRI,” *Magn. Reson. Med.*, vol. 48, no. 6, pp. 987–993, Dec. 2002.

[9] T. Kato, A. Kamei, S. Takashima, and T. Ozaki, “Human Visual Cortical Function during Photic Stimulation Monitoring by Means of near-Infrared Spectroscopy,” *J. Cereb. Blood Flow Metab.*, vol. 13, no. 3, pp. 516–520, May 1993.

[10] P. T. Fox, M. E. Raichle, M. A. Mintun, and C. Dence, “Nonoxidative glucose consumption during focal physiologic neural activity,” *Science (80-.).*, vol. 241, no. 4864, pp. 462–464, 1988.

[11] N. K. Logothetis, “What we can do and what we cannot do with fMRI,” *Nature*, vol. 453, no. 7197, pp. 869–878, Jun. 2008.

[12] A. Ekstrom, “How and when the fMRI BOLD signal relates to underlying neural activity: The danger in dissociation,” *Brain Res. Rev.*, vol. 62, no. 2, pp. 233–244, Mar. 2010.

[13] M. T. Lippert, T. Steudel, F. Ohl, N. K. Logothetis, and C. Kayser, “Coupling of neural activity and fMRI-BOLD in the motion area MT,” *Magn. Reson. Imaging*, vol. 28, no. 8, pp. 1087–1094, Oct. 2010.

[14] A. C. Silva, E. L. Barbier, I. J. Lowe, and A. P. Koretsky, “Radial Echo-Planar Imaging,” *J. Magn. Reson.*, vol. 135, no. 1, pp. 242–247, Nov. 1998.

[15] J. I. Jackson, C. H. Meyer, D. G. Nishimura, and A. Macovski, “Selection of a convolution function for Fourier inversion using gridding (computerised tomography application),” *IEEE Trans. Med. Imaging*, vol. 10, no. 3, pp. 473–478, 1991.

[16] P. J. Beatty, D. G. Nishimura, and J. M. Pauly, “Rapid gridding reconstruction with a minimal oversampling ratio,” *IEEE Trans. Med. Imaging*, vol. 24, no. 6, pp. 799–808, Jun. 2005.

[17] D. Parker, G. Rotival, A. Laine, and Q. R. Razlighi, “RETROSPECTIVE DETECTION OF INTERLEAVED SLICE ACQUISITION PARAMETERS FROM FMRI DATA,” *ISBI*, 2014.

[18] B. B. Biswal *et al.*, “Toward discovery science of human brain function.,” *Proc. Natl. Acad. Sci. U. S. A.*, vol. 107, no. 10, pp. 4734–9, Mar. 2010.

[19] J. D. Power, K. A. Barnes, A. Z. Snyder, B. L. Schlaggar, and S. E. Petersen, “Spurious but systematic correlations in functional connectivity MRI networks arise from subject motion,” *Neuroimage*, vol. 59, no. 3, pp. 2142–2154, Feb. 2012.

[20] J. V. Hajnal, R. Myers, A. Oatridge, J. E. Schwieso, I. R. Young, and G. M. Bydder, “Artifacts due to stimulus correlated motion in functional imaging of the brain,” *Magn. Reson. Med.*, vol. 31, no. 3, pp. 283–291, Mar. 1994.

[21] A. S. Field, Y. F. Yen, J. H. Burdette, and A. D. Elster, “False cerebral activation on BOLD functional MR images: study of low-amplitude motion weakly correlated to stimulus.,” *AJNR. Am. J. Neuroradiol.*, vol. 21, no. 8, pp. 1388–96, Sep. 2000.

[22] R. W. Cox, “AFNI: Software for Analysis and Visualization of Functional Magnetic Resonance Neuroimages,” *Comput. Biomed. Res.*, vol. 29, no. 3, pp. 162–173, Jun. 1996.

[23] J. D. Power, M. Plitt, P. Kundu, P. A. Bandettini, and A. Martin, “Temporal interpolation alters motion in fMRI scans: Magnitudes and consequences for artifact detection,” *PLoS One*, vol. 12, no. 9, p. e0182939, Sep. 2017.

[24] A. Kaushik *et al.*, “Estimation of radiation dose to patients from 18FDG whole body PET/CT investigations using dynamic PET scan protocol,” *Indian J. Med. Res.*, vol. 142, no. 6, p. 721, Dec. 2015.

[25] C. M. Collins *et al.*, “Temperature and SAR calculations for a human head within volume and surface coils at 64 and 300 MHz,” *J. Magn. Reson. Imaging*, vol. 19, no. 5, pp. 650–656, May 2004.

[26] J. T. Vaughan *et al.*, “7T vs. 4T: RF power, homogeneity, and signal-to-noise comparison in head images,” *Magn. Reson. Med.*, vol. 46, no. 1, pp. 24–30, Jul. 2001.

[27] FDA, “MRI (Magnetic Resonance Imaging) - Benefits and Risks,” 2017.

[28] O. Carmichael *et al.*, “The role of fMRI in drug development,” *Drug Discov. Today*, vol. 23, no. 2, pp. 333–348, Feb. 2018.

[29] N. Jaworska, X.-R. Yang, V. Knott, and G. MacQueen, “A review of fMRI studies during visual emotive processing in major depressive disorder,” *World J. Biol. Psychiatry*, vol. 16, no. 7, pp. 448–471, Oct. 2015.

[30] H. Macpherson, M. Formica, E. Harris, and R. M. Daly, “Brain functional alterations in Type 2 Diabetes – A systematic review of fMRI studies,” *Front. Neuroendocrinol.*, vol. 47, pp. 34–46, Oct. 2017.

[31] H. Khazaie *et al.*, “Functional reorganization in obstructive sleep apnoea and insomnia: A systematic review of the resting-state fMRI,” *Neurosci. Biobehav. Rev.*, vol. 77, pp. 219–231, Jun. 2017.

[32] D. P. Terry, D. Sabatinelli, A. N. Puente, N. A. Lazar, and L. S. Miller, “A Meta-Analysis of fMRI Activation Differences during Episodic Memory in Alzheimer’s Disease and Mild Cognitive Impairment,” *J. Neuroimaging*, vol. 25, no. 6, pp. 849–860, Nov. 2015.

[33] H.-J. Li, X.-H. Hou, H.-H. Liu, C.-L. Yue, Y. He, and X.-N. Zuo, “Toward systems neuroscience in mild cognitive impairment and Alzheimer’s disease: A meta-analysis of 75 fMRI studies,” *Hum. Brain Mapp.*, vol. 36, no. 3, pp. 1217–1232, Mar. 2015.

[34] J. V. Hull, L. B. Dokovna, Z. J. Jacokes, C. M. Torgerson, A. Irimia, and J. D. Van Horn, “Resting-State Functional Connectivity in Autism Spectrum Disorders: A Review,” *Front. Psychiatry*, vol. 7, p.

205, Jan. 2017.

[35] M. Tahmasian *et al.*, “A systematic review on the applications of resting-state fMRI in Parkinson’s disease: Does dopamine replacement therapy play a role?,” *Cortex*, vol. 73, pp. 80–105, Dec. 2015.

[36] D. C. Van Essen, S. M. Smith, D. M. Barch, T. E. J. Behrens, E. Yacoub, and K. Ugurbil, “The WU-Minn Human Connectome Project: An overview,” *Neuroimage*, vol. 80, pp. 62–79, 2013.

[37] P. M. Matthews and A. Hampshire, “Clinical Concepts Emerging from fMRI Functional Connectomics,” *Neuron*, vol. 91, no. 3, pp. 511–528, Aug. 2016.

[38] R. M. Birn *et al.*, “The effect of scan length on the reliability of resting-state fMRI connectivity estimates,” *Neuroimage*, vol. 83, pp. 550–558, Dec. 2013.

[39] R. Sladky, K. J. Friston, J. Tröstl, R. Cunnington, E. Moser, and C. Windischberger, “Slice-timing effects and their correction in functional MRI,” *Neuroimage*, vol. 58, no. 2, pp. 588–594, Sep. 2011.

[40] R. Henson, C. Buechel, O. Josephs, and K. Friston, “The slice-timing problem in event-related fMRI,” *Neuroimage*, 1999.

[41] K. Vogt, J. Ibinson, R. Small, and P. Schmalbrock, “Slice-timing correction affects functional MRI noise, model fit, activation maps, and physiologic noise correction,” in *Proceedings 17th Scientific Meeting, International Society for Magnetic Resonance in Medicine*, 2009, vol. Honolulu, p. 3679.

[42] K. J. Friston, A. P. Holmes, K. J. Worsley, J.-P. Poline, C. D. Frith, and R. S. J. Frackowiak, “Statistical parametric maps in functional imaging: A general linear approach,” *Hum. Brain Mapp.*, vol. 2, no. 4, pp. 189–210, Jan. 1994.

[43] M. Jenkinson, C. F. Beckmann, T. E. J. Behrens, M. W. Woolrich, and S. M. Smith, “FSL,” *Neuroimage*, vol. 62, no. 2, pp. 782–790, Aug. 2012.

[44] B. Fischl *et al.*, “Whole Brain Segmentation: Automated Labeling of Neuroanatomical Structures in the Human Brain,” *Neuron*, vol. 33, no. 3, pp. 341–355, Jan. 2002.

[45] B. Fischl *et al.*, “Sequence-independent segmentation of magnetic resonance images,” *Neuroimage*, vol. 23, Supple, pp. S69–S84, 2004.

[46] D. N. Greve and B. Fischl, “Accurate and robust brain image alignment using boundary-based registration,” *Neuroimage*, vol. 48, no. 1, pp. 63–72, Oct. 2009.

[47] M. Jenkinson, P. Bannister, M. Brady, and S. Smith, “Improved Optimization for the Robust and Accurate Linear Registration and Motion Correction of Brain Images,” *Neuroimage*, vol. 17, no. 2, pp. 825–841, Oct. 2002.

[48] K. J. Friston *et al.*, “Analysis of fMRI time-series revisited.,” *NeuroImage*, vol. 2, no. 1. pp. 45–53, Mar-1995.

[49] B. Kim, J. L. Boes, P. H. Bland, T. L. Chenevert, and C. R. Meyer, “Motion correction in fMRI via registration of individual slices into an anatomical volume,” *Magn. Reson. Med.*, vol. 41, no. 5, pp. 964–972, 1999.

[50] C. F. Beckmann, M. Jenkinson, and S. M. Smith, “General multilevel linear modeling for group analysis in FMRI,” *Neuroimage*, vol. 20, no. 2, pp. 1052–1063, Oct. 2003.

[51] M. W. Woolrich, T. E. J. Behrens, C. F. Beckmann, M. Jenkinson, and S. M. Smith, “Multilevel linear modelling for FMRI group analysis using Bayesian inference,” *Neuroimage*, vol. 21, no. 4, pp. 1732–1747, Apr. 2004.

[52] R. A. Poldrack, J. A. Mumford, and T. E. Nichols, *Handbook of functional MRI data analysis*. Cambridge University Press, 2011.

[53] V. Calhoun, X. Golay, and G. Pearlson, “Improved fMRI slice timing correction: interpolation errors

and wrap around effects," *Proceedings, ISMRM, 9th Annu. Meet. Denver*, p. 810, 2000.

[54] N. White *et al.*, "PROMO: Real-time prospective motion correction in MRI using image-based tracking," *Magn. Reson. Med.*, vol. 63, no. 1, pp. 91–105, Jan. 2010.

[55] M. Zaitsev, J. Maclaren, and M. Herbst, "Motion artifacts in MRI: A complex problem with many partial solutions," *J. Magn. Reson. Imaging*, vol. 42, no. 4, pp. 887–901, Oct. 2015.

[56] R. Bhagalia and B. Kim, "Spin saturation artifact correction using slice-to-volume registration motion estimates for fMRI time series," *Med. Phys.*, vol. 35, no. 2, pp. 424–434, Jan. 2008.

[57] W. Chunli, D. Zhibing, Y. Kun, and W. Yun, "An improved algorithm of translational motion artifact correction for MRI," in *The 27th Chinese Control and Decision Conference (2015 CCDC)*, 2015, pp. 4054–4057.

[58] B. Zahneisen, B. Keating, A. Singh, M. Herbst, and T. Ernst, "Reverse retrospective motion correction," *Magn. Reson. Med.*, vol. 75, no. 6, pp. 2341–2349, Jun. 2016.

[59] T. Johnstone *et al.*, "Motion correction and the use of motion covariates in multiple-subject fMRI analysis," *Hum. Brain Mapp.*, vol. 27, no. 10, pp. 779–788, Oct. 2006.

[60] M. Hedley, H. Yan, and D. Rosenfeld, "Motion artifact correction in MRI using generalized projections," *IEEE Trans. Med. Imaging*, vol. 10, no. 1, pp. 40–46, Mar. 1991.

[61] T. R. Oakes *et al.*, "Comparison of fMRI motion correction software tools," *Neuroimage*, vol. 28, no. 3, pp. 529–543, Nov. 2005.

[62] R. Birn, "An Improved Model of Motion-Related Signal Changes in fMRI," *Neuroimage*, pp. 3–7, 2016.

[63] J. D. Power, A. Mitra, T. O. Laumann, A. Z. Snyder, B. L. Schlaggar, and S. E. Petersen, "Methods to detect, characterize, and remove motion artifact in resting state fMRI," *Neuroimage*, vol. 84, pp. 320–341, Jan. 2014.

[64] K. J. Friston, S. Williams, R. Howard, R. S. J. Frackowiak, and R. Turner, "Movement-Related effects in fMRI time-series," *Magn. Reson. Med.*, vol. 35, no. 3, pp. 346–355, Mar. 1996.

[65] P. R. Bannister, J. Michael Brady, and M. Jenkinson, "Integrating temporal information with a non-rigid method of motion correction for functional magnetic resonance images," *Image Vis. Comput.*, vol. 25, no. 3, pp. 311–320, Mar. 2007.

[66] H. J. Jo *et al.*, "Effective Preprocessing Procedures Virtually Eliminate Distance-Dependent Motion Artifacts in Resting State FMRI.," *J. Appl. Math.*, vol. 2013, May 2013.

[67] H. J. Jo, Z. S. Saad, W. K. Simmons, L. A. Milbury, and R. W. Cox, "Mapping sources of correlation in resting state FMRI, with artifact detection and removal," *Neuroimage*, vol. 52, no. 2, pp. 571–582, Aug. 2010.

[68] L. Griffanti *et al.*, "ICA-based artefact removal and accelerated fMRI acquisition for improved resting state network imaging," *Neuroimage*, vol. 95, pp. 232–247, Jul. 2014.

[69] P. Kundu, M. D. Santin, P. A. Bandettini, E. T. Bullmore, and A. Petiet, "Differentiating BOLD and non-BOLD signals in fMRI time series from anesthetized rats using multi-echo EPI at 11.7T," *Neuroimage*, vol. 102, pp. 861–874, Nov. 2014.

[70] P. Kundu, S. J. Inati, J. W. Evans, W.-M. Luh, and P. A. Bandettini, "Differentiating BOLD and non-BOLD signals in fMRI time series using multi-echo EPI," *Neuroimage*, vol. 60, no. 3, pp. 1759–1770, Apr. 2012.

[71] J. D. Power, B. M. Silver, M. R. Silverman, E. L. Ajodan, D. J. Bos, and R. M. Jones, "Customized head molds reduce motion during resting state fMRI scans," *Neuroimage*, vol. 189, pp. 141–149,

Apr. 2019.

[72] S. E. Yancey *et al.*, “Spin-history artifact during functional MRI: Potential for adaptive correction,” *Med. Phys.*, vol. 38, no. 8, pp. 4634–4646, Jul. 2011.

[73] J. Schulz *et al.*, “Prospective slice-by-slice motion correction reduces false positive activations in fMRI with task-correlated motion,” *Neuroimage*, vol. 84, pp. 124–132, Jan. 2014.

[74] N. Todd, O. Josephs, M. F. Callaghan, A. Lutti, and N. Weiskopf, “Prospective motion correction of 3D echo-planar imaging data for functional MRI using optical tracking,” *Neuroimage*, vol. 113, pp. 1–12, Jun. 2015.

[75] R. Frost *et al.*, “Markerless high-frequency prospective motion correction for neuroanatomical MRI,” *Magn. Reson. Med.*, vol. 82, no. 1, pp. 126–144, Jul. 2019.

[76] O. Speck, J. Hennig, and M. Zaitsev, “Prospective Real-Time Slice-by-Slice Motion Correction for fMRI in Freely Moving Subjects,” *Magn. Reson. Mater. Physics, Biol. Med.*, vol. 19, no. 2, pp. 55–61, May 2006.

[77] S. Thesen, O. Heid, E. Mueller, and L. R. Schad, “Prospective acquisition correction for head motion with image-based tracking for real-time fMRI,” *Magn. Reson. Med.*, vol. 44, no. 3, pp. 457–465, Sep. 2000.

[78] M. D. Tisdall, A. T. Hess, M. Reuter, E. M. Meintjes, B. Fischl, and A. J. W. van der Kouwe, “Volumetric navigators for prospective motion correction and selective reacquisition in neuroanatomical MRI,” *Magn. Reson. Med.*, vol. 68, no. 2, pp. 389–399, Aug. 2012.

[79] J. Maclaren, M. Aksoy, M. B. Ooi, B. Zahneisen, and R. Bammer, “Prospective motion correction using coil-mounted cameras: Cross-calibration considerations,” *Magn. Reson. Med.*, vol. 79, no. 4, pp. 1911–1921, Apr. 2018.

[80] M. Zaitsev, B. Akin, P. LeVan, and B. R. Knowles, “Prospective motion correction in functional MRI,” *Neuroimage*, vol. 154, pp. 33–42, Jul. 2017.

[81] M. Zaitsev, C. Dold, J. Hennig, and O. Speck, “Prospective Real-Time Slice-by-Slice 3D Motion Correction for EPI Using an External Optical Motion Tracking System,” *Proc. Int. Soc. Magn. Reson. Med.*, p. 517, 2004.

[82] I. Drobnjak, D. Gavaghan, E. Süli, J. Pitt-Francis, and M. Jenkinson, “Development of a functional magnetic resonance imaging simulator for modeling realistic rigid-body motion artifacts,” *Magn. Reson. Med.*, vol. 56, no. 2, pp. 364–380, Aug. 2006.

[83] I. Drobnjak, G. S. Pell, and M. Jenkinson, “Simulating the effects of time-varying magnetic fields with a realistic simulated scanner,” *Magn. Reson. Imaging*, vol. 28, no. 7, pp. 1014–1021, Sep. 2010.

[84] C. Triantafyllou *et al.*, “Comparison of physiological noise at 1.5 T, 3 T and 7 T and optimization of fMRI acquisition parameters,” *Neuroimage*, vol. 26, no. 1, pp. 243–250, May 2005.

[85] P. Dragicevic, “Fair Statistical Communication in HCI,” Springer, Cham, 2016, pp. 291–330.

[86] L. Friedman, G. H. Glover, D. Krenz, and V. Magnotta, “Reducing inter-scanner variability of activation in a multicenter fMRI study: Role of smoothness equalization,” *Neuroimage*, vol. 32, no. 4, pp. 1656–1668, Oct. 2006.

[87] E. C. Caparelli and D. Tomasi, “K-space spatial low-pass filters can increase signal loss artifacts in Echo-Planar Imaging.,” *Biomed. Signal Process. Control*, vol. 3, no. 1, pp. 107–114, Jan. 2008.

[88] M. J. Lowe and J. A. Sorenson, “Spatially filtering functional magnetic resonance imaging data,” *Magn. Reson. Med.*, vol. 37, no. 5, pp. 723–729, May 1997.

[89] Q. R. Razlighi, J. Steffener, C. Habeck, A. Laine, and Y. Stern, “Resting state inter and intra

hemispheric human brain functional connectivity," in *2013 35th Annual International Conference of the IEEE Engineering in Medicine and Biology Society (EMBC)*, 2013, pp. 6522–6525.

[90] C. E. Davey, D. B. Grayden, G. F. Egan, and L. A. Johnston, "Filtering induces correlation in fMRI resting state data," *Neuroimage*, vol. 64, pp. 728–740, Jan. 2013.

[91] C. Dold, M. Zaitsev, O. Speck, E. A. Firle, J. Hennig, and G. Sakas, "Updating of MRI Gradients Using a Infrared Tracking System to Compensate Motion Artifacts."

[92] E. B. Beall and M. J. Lowe, "SimPACE: Generating simulated motion corrupted BOLD data with synthetic-navigated acquisition for the development and evaluation of SLOMOCO: A new, highly effective slicewise motion correction," *Neuroimage*, vol. 101, pp. 21–34, Nov. 2014.

[93] S. J. Clare, "Functional magnetic resonance imaging : methods and applications," University of Nottingham, 1997.

[94] C. Figley, "Improved Methods for Motion-Compensating and Event-Related Spinal Functional Magnetic Resonance Imaging (fMRI)," 2019.

[95] R. Gebker, J. Schwitter, E. Fleck, and E. Nagel, "How We Perform Myocardial Perfusion With Cardiovascular Magnetic Resonance," *J. Cardiovasc. Magn. Reson.*, vol. 9, no. 3, pp. 539–547, May 2007.

Appendix A: Proof of Commutative Property for Mean and Autocorrelation Operation

The fundamental principles can be explained in a 2D case, which can be applied to an arbitrary number of dimensions without loss of generality.

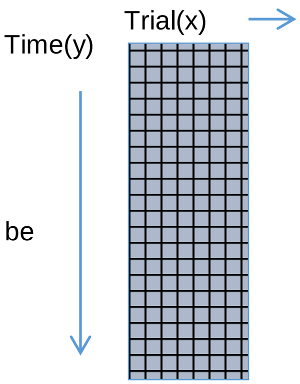

A.1. Definitions

- s[x,y] is a 2D array with NxM elements. In this analysis, an average will be taken over trials (x axis, columns).
- F{ } is a discrete Fourier transform operation

2D DFT pair:

The 2D DFT is defined as follows:

$$S[k,l] = F\{s[x,y]\} = \sum_{y=0}^{M-1}\sum_{x=0}^{N-1} s[x,y]\left(e^{-i2\pi kx/N}\, e^{-i2\pi ly/M}\right) \tag{0.1}$$

Where S[k,l] is the DFT of s[x,y]. In this proof, capital letters indicate the Fourier transform of a function, and lowercase letters indicate the time (or space) domain of a function. The inverse DFT is defined as:

$$s[x,y] = F^{-1}\{S[k,l]\} = \frac{1}{NM}\sum_{l=0}^{M-1}\sum_{k=0}^{N-1} S[k,l]\left(e^{i2\pi kx/N} e^{i2\pi ly/M}\right) \tag{0.2}$$

Autocorrelation:

$c_{xx}[x,y]$ is the correlation (non-normalized) of any function x with itself. The autocorrelation is defined in terms of its well-known Fourier transform relationship, where the Fourier transform of the autocorrelation of a function *s* is equal to the Fourier transform of the function *s*, squared. Thus, the autocorrelation can be found with the following equation:

$$c_{ss} = F^{-1}\{F\{s[x,y]\}^2\} \tag{0.3}$$

From (1), we can substitute $S[k,l] = F\{s[x,y]\}$:

$$c_{ss} = F^{-1}\{S[k,l]^2\} \tag{0.4}$$

Taking the Fourier transform of both sides gives us:

$$F\{c_{ss}[x,y]\} = C_{ss}[k,l] = S[k,l]^2 \tag{0.5}$$

Average:

We denote the average of a function with a ^ symbol, and a subscript denoting the axis along which the average was taken. For example, $\hat{s}_x[y]$ is the average of the signal s along the x axis. And is defined as:

$$\hat{s}_x[y] = Mean(s[x,y],x) = \frac{1}{N}\sum_{x=0}^{N} s[x,y] \tag{0.6}$$

Projection:

The projection of a 2D signal is defined as the summation of the signal along a given axis. The projection of the signal *s* along the *x* axis is denoted as $p_{sx}[y]$, and is defined as

$$p_{sx}[y] = \sum_{x=0}^{N} s[x,y] = N\hat{s}_x[y] \tag{0.7}$$

And in the frequency domain:

$$F\{p_{sx}[y]\} = F\{N\hat{s}_x[y]\} \tag{0.8}$$

$$P_{sx}[l] = N\hat{S}_x[l] \tag{0.9}$$

A.2. Proof

<u>Question</u>:

Is the average of an autocorrelation equivalent to the autocorrelation of an average, along a given axis of a 2D signal?

$$c_{\hat{s}_x\hat{s}_x}[y] = \hat{c}_{ssx}[\mathrm{y}] \qquad (\ 0.10\ )$$

Proof:

First, the Fourier pairs are derived for the mean of a signal along a given axis. If the Fourier transform of $s(x,y)$ is $S[k,l]$, what is the fourier transform of $\hat{s}_x(y)$? According to the projection-slice theorem, the Fourier transform of a signals projection along a given axis is equal to a slice of the original fourier transform that intersects the origin and is parallel to the projection. For a projection along a primary axis, this means that the Fourier transform of the projection is equivalent to the center line of the Fourier transform along the remaining axis. In other words, the projection along the x axis of a 2D function has the 1D Fourier transform:

$$F\{p_{sx}[y]\} = S[k/2, l] \qquad (\ 0.11\ )$$

Using equation (0.9), we can rewrite equation (0.11) as:

$$S[k/2, l] = N\hat{S}_x[l] \qquad (\ 0.12\ )$$

This allows the Fourier Transform of the mean to be described in terms of the original signal:

$$\hat{S}_x[l] = \frac{1}{N} S\left[\frac{k}{2}, l\right] \qquad (\ 0.13\ )$$

The next step is to examine the autocorrelation of the x-averaged function and define it as $c_{\hat{s}_x\hat{s}_x}[y]$. First, the Fourier transform pair for $c_{\hat{s}_x\hat{s}_x}(y)$ will be derived using equations (0.3), (0.4), and (0.5):

$$c_{\hat{s}_x\hat{s}_x}[y] = F^{-1}\{F\{\hat{s}_x[y]\}^2\} = F^{-1}\{\hat{S}_x[l]^2\} \qquad (\ 0.14\ )$$

$$C_{\hat{s}_x\hat{s}_x}[l] = \hat{S}_x[l]^2 \qquad (\ 0.15\ )$$

Equation (0.13) can be used to put $\hat{S}_x$ in terms of the original signal's Fourier transform, S

$$C_{\hat{s}_x\hat{s}_x}[l] = \frac{1}{N^2} S\left[\frac{k}{2}, l\right]^2 \qquad (\ 0.16\ )$$

(0.16) is the definition of the autocorrelation of a signal averaged along the x axis, in terms of the original signal's Fourier transform.

The next step is to examine the autocorrelation of the original signal, s. This is denoted as $c_{ss}[x, y]$, and defined by equations (0.3) and:

$$c_{ss}[x, y] = F^{-1}\{F\{s[x, y]\}^2\} \qquad (\ 0.17\ )$$

$$C_{ss}[k, l] = S[k, l]^2 \qquad (\ 0.18\ )$$

Using the same properties of the projection theorem from equations (0.11), (0.12), (0.13), the average of the autocorrelation function along the x axis can be defined as:

$$\hat{c}_{ssx}[y] = \frac{1}{N} p_{c_{ss}x}[y] \qquad (\ 0.19\ )$$

$$\hat{C}_{ssx}[l] = \frac{1}{N} C_{ss}\left[\frac{k}{2}, l\right] \text{ (20)} \qquad (\ 0.20\ )$$

Substituting equation (0.18) into equation (0.20) defines the average of the autocorrelation in terms of the original signal's Fourier transform:

$$\hat{C}_{ssx}[l] = \frac{1}{N} S\left[\frac{k}{2}, l\right]^2 \qquad (\ 0.21\ )$$

By multiplying equation (0.21) by 1/N, it is equivalent to equation (0.16), which is the autocorrelation of the averaged function:

$$\frac{1}{N}\hat{C}_{ssx}[l] = C_{\hat{s}_x\hat{s}_x}[l] \qquad (\ 0.22\ )$$

Thus, the autocorrelation of the average is equivalent to the average of the autocorrelation, scaled by a factor of 1/N

Appendix B: Derivation of the Signal Equation & the Effect of Motion

A.3. Derivation of the fMRI Signal Equation Without Motion:

The Bloch equation states that transverse magnetization at a 3D spatial coordinate $\boldsymbol{r}$ at time t (relative to the last RF pulse at t_0) is equal to the magnitude of the transverse magnetization at the time of the RF pulse ($|M_{xy}(\boldsymbol{r}, t_0)|$), multiplied with a phase component described by its rotation $e^{i\omega(\boldsymbol{r},t)}$, and it's T_2^* decay described by $e^{-(t-t_0)/T_2^*(\boldsymbol{r},t)}$, where ω is the Larmor frequency of the protons at point $\boldsymbol{r}$, and $T_2^*(\boldsymbol{r}, t)$ is the rate of decay of the transverse magnetization, which varies spatially over $\boldsymbol{r}$ as well as temporally, which is the basis of the BOLD signal. The full equation is described in equation (0.1):

$$M_{xy}(\boldsymbol{r}, t) = e^{-(t-t_0)/T_2^*(\boldsymbol{r},t)} \left| M_{xy}(\boldsymbol{r}, t_0) \right| e^{i\omega(\boldsymbol{r},t)} \tag{0.1}$$

The signal acquired by the receive coils in an fMRI scanner is equal to the sum of all transverse components from all the protons in the excited slice. In other words, we take an integral of this equation over all points in $\boldsymbol{r}$ for excited tissues. We can simplify this equation if the readout time is small compared to the T_2^* decay by omitting the first exponential. Additionally, once the objects flip angle reaches steady-state, M_{xy} at time t_0 is assumed to be constant for each location $\boldsymbol{r}$, with spatial variation as a function of proton density, ρ. With these adjustments, equation (0.1) can be approximated to create a signal equation:

$$s(t) = \int_r \rho(\boldsymbol{r}) \boldsymbol{e}^{\boldsymbol{i}\varphi(\boldsymbol{r},t)} \, d\boldsymbol{r} \tag{0.2}$$

Where φ is the accumulated phase, which is derived from the function describing the frequency at which the protons spin in the scanner, $\omega(\boldsymbol{r}, t)$:

$$\omega(\boldsymbol{r}, t) = \omega_0 + \omega_G(\boldsymbol{r}, t) \tag{0.3}$$

Where ω_0 is the frequency due to the static magnetic field, B0, and $\omega_G(\boldsymbol{r}, t)$ is the frequency offset due to any spatial gradients applied in the scanner. The magnitude of this gradient-induced phase offset varies depending on the position $\boldsymbol{r}$ in the scanner. This is the fundamental principle behind frequency encoding, which allows for image reconstruction in EPI pulse sequences. In a typical scanner, this phase is demodulated, essentially removing the phase component belonging to ω_0, leaving only the ω_G component. The actual amount of frequency offset depends on the gradient strength, the location of the object, and the gyromagnetic ratio, shown in equation (0.4):

$$\omega_G(\boldsymbol{r},t) = -\gamma \boldsymbol{G}(t) \cdot \boldsymbol{r} \qquad (0.4)$$

Where the negative sign accounts for the “Counter clockwise positive” rotation convention. A typical EPI pulse sequence takes about 60ms to acquire a single 2D slice of k-space. During this time, the frequency offset accumulates, referred to as “accumulated phase”, which is calculated as the integral of the frequency offset over the readout time:

$$\varphi(\boldsymbol{r},t) = \int_0^t \omega_G(\boldsymbol{r},t)\, dt = -\int_{\boldsymbol{0}}^{\boldsymbol{t}} \gamma \boldsymbol{G}(t) \cdot \boldsymbol{r} dt = -\gamma \int_{\boldsymbol{0}}^{\boldsymbol{t}} \boldsymbol{G}(t) dt \cdot \boldsymbol{r} \qquad (0.5)$$

The factors γ and ***r*** do not change with time, and so they can be placed outside the integral. This leads to the classical description of “k-space”, where the signal at time t is being recorded from location ***k*** in k-space:

$$\boldsymbol{k}(t) = \gamma \int_{\boldsymbol{0}}^{\boldsymbol{t}} \boldsymbol{G}(t) \qquad (0.6)$$

Substituting equations (0.6) and (0.5) into (0.2), we obtain:

$$s(t) = \int_r \rho(\boldsymbol{r}) \boldsymbol{e}^{-i\boldsymbol{k}(\boldsymbol{t})\cdot \boldsymbol{r}}\, d\boldsymbol{r} \qquad (0.7)$$

which has the form of a Fourier transform.

A.4. Derivation of the fMRI Singal Equation With Motion:

This equation is where we begin our analysis of motion in fMRI. We can now consider two coordinate systems: The object, $\boldsymbol{r_{ob}}$, and the scanner, $\boldsymbol{r_{sc}}$. Without motion, these coordinate systems are static, and we simply set them equal to each other, where $\boldsymbol{r} = \boldsymbol{r_{ob}} = \boldsymbol{r_{sc}}$. However, this no longer holds true if the object moves. When motion is present, we must describe the object's location relative to its initial position, specifically at the time of excitation from the most recent RF pulse. If the object is initially aligned with the scanner's coordinate system, $\boldsymbol{r_{sc}}$, and moves in a way described by a rotation matrix R and a translation vector $\boldsymbol{T}$, we can describe a point in the object's coordinate in terms of the scanner's coordinates:

$$\boldsymbol{r_{sc}} = R(t)\boldsymbol{r_{ob}} + \boldsymbol{T}(t) \tag{0.8}$$

And it follows that we can describe a point in the scanner in terms of the object's coordinates:

$$R^{-1}(t)\boldsymbol{r_{sc}} - R^{-1}(t)\boldsymbol{T}(t) = \boldsymbol{r_{ob}} \tag{0.9}$$

To model the motion as a stationary object with an inverse rotation of the scanner, we must reevaluate equations (0.4), (0.5), and (0.6) to account for this rotation, as the spatial coordinate $\boldsymbol{r}$ is now changing with time, and cannot be removed from the integral in (0.5):

$$\omega_G(\boldsymbol{r_{sc}}, t) = -\gamma\boldsymbol{G}(t) \cdot \boldsymbol{r_{sc}} = -\gamma\boldsymbol{G}(t) \cdot (R(t)\boldsymbol{r_{ob}} + \boldsymbol{T}(t)) \tag{0.10}$$

$$\varphi(\boldsymbol{r_{ob}}, t) = \int_0^t \omega_G(\boldsymbol{r_{ob}}, t)\, dt = -\gamma \int_{\boldsymbol{0}}^{\boldsymbol{t}} \boldsymbol{G}(t) \cdot (R(t)\boldsymbol{r_{ob}} + \boldsymbol{T}(t))dt \tag{0.11}$$

We now distribute the dot product with $\boldsymbol{G}$ and evaluate each component separately:

$$\varphi(\boldsymbol{r_{ob}}, t) = -\gamma \int_{\boldsymbol{0}}^{\boldsymbol{t}} \boldsymbol{G}(t) \cdot R(t)\boldsymbol{r_{ob}}dt - \gamma \int_{\boldsymbol{0}}^{\boldsymbol{t}} \boldsymbol{G}(t) \cdot \boldsymbol{T}(t)dt \tag{0.12}$$

The first term deals with rotation and has the actual object's coordinates in the integral term. We can use the properties of a dot product to simplify this notation. The geometric definition of a dot product of two vectors in space is:

$$\boldsymbol{a} \cdot \boldsymbol{b} = \|\boldsymbol{a}\|\|\boldsymbol{b}\|\cos(\theta) \tag{0.13}$$

Where $\|\boldsymbol{a}\|$ is the magnitude of the vector, and theta is the angle between **a** and **b**. In our example, $\boldsymbol{r_{ob}}$ is rotated by the rotation matrix R. Because a rotation will not change the magnitude of a vector, the first two components of equation (0.13) remain unchanged. The angle between the vectors, however, will change depending on the rotation matrix. A rotation matrix R rotating vector ***b*** by α degrees away from vector ***a*** changes equation (0.13) to:

$$\boldsymbol{a} \cdot R\boldsymbol{b} = \|\boldsymbol{a}\|\|\boldsymbol{b}\|\cos(\theta + \alpha) \qquad (0.14)$$

Likewise, rotating vector ***a*** by α degrees away from vector ***b*** also increases the angle between the two vectors by α, and the result is the same as equation (0.14). Note, that rotating vector ***a*** away from vector b is the inverse (opposite) rotation applied to rotate vector ***b*** away from vector ***a***. For rotation matrices, a rotation in the opposite direction is equivalent to the inverse of the original matrix. In other words:

$$R(-\theta) = R^{-1}(\theta) \qquad (0.15)$$

From equation (0.14), this means:

$$\boldsymbol{a} \cdot R\boldsymbol{b} = R^{-1}\boldsymbol{a} \cdot \boldsymbol{b} \qquad (0.16)$$

Using this property in equation (0.12), we can move the rotation to the gradient vector $\boldsymbol{G}$, and once again remove the $\boldsymbol{r_{ob}}$ vector from the integral:

$$\varphi(\boldsymbol{r_{ob}}, t) = -\gamma \int_{\boldsymbol{0}}^{\boldsymbol{t}} R^{-1}(t)\boldsymbol{G}(t)dt \cdot \boldsymbol{r_{ob}} - \gamma \int_{\boldsymbol{0}}^{\boldsymbol{t}} \boldsymbol{G}(t) \cdot \boldsymbol{T}(t)dt \qquad (0.17)$$

We can now modify our K-space formula and update our signal equation:

$$\boldsymbol{k_R}(t) = \gamma \int_{\boldsymbol{0}}^{\boldsymbol{t}} R^{-1}(t)\boldsymbol{G}(t)dt \qquad (0.18)$$

$$
\begin{aligned}
s(t) &= \int_{r_{ob}} \rho(\boldsymbol{r_{ob}}) \boldsymbol{e}^{-i(\boldsymbol{k_R}(t)\cdot\boldsymbol{r_{ob}} - \gamma \int_{\boldsymbol{0}}^{\boldsymbol{t}} \boldsymbol{G}(t)\cdot\boldsymbol{T}(t)dt)}\, d\boldsymbol{r_{ob}} \\
&= \left(\boldsymbol{e}^{i\gamma \int_{\boldsymbol{0}}^{\boldsymbol{t}} \boldsymbol{G}(t)\cdot\boldsymbol{T}(t)dt}\right). \int_{r_{ob}} \rho(\boldsymbol{r_{ob}}) \boldsymbol{e}^{-i\boldsymbol{k_R}(\boldsymbol{t})\cdot\boldsymbol{r_{ob}}}\, d\boldsymbol{r_{ob}}
\end{aligned}
\qquad (0.19)
$$